

Myeloid progenitor dysregulation fuels immunosuppressive macrophages in tumours

<https://doi.org/10.1038/s41586-025-09493-y>

Received: 17 June 2024

Accepted: 5 August 2025

Published online: 10 September 2025

 Check for updates

Samarth Hegde^{1,2}, Bruno Giotti^{1,3,13}, Brian Y. Soong^{1,2,13}, Laszlo Halasz^{1,2}, Jessica Le Berichel^{1,2}, Maximilian M. Schaefer^{1,2}, Benoit Kloeckner⁴, Raphaël Mattiuz^{1,2}, Matthew D. Park^{1,2}, Assaf Magen¹, Adam Marks^{1,2,3,5}, Meriem Belabed^{1,2}, Pauline Hamon^{1,2}, Theodore Chin^{1,2}, Leanna Troncoso^{1,2}, Juliana J. Lee⁶, Kaili Fan⁷, Dughan Ahimovic^{8,9}, Michael J. Bale^{8,9}, Kai Nie^{1,2,10}, Grace Chung^{1,2,10}, Darwin D'souza^{1,2,10}, Krista Angeliadis^{1,2,10}, Seunghee Kim-Schulze^{1,2,10}, Raja M. Flores^{5,11,12}, Andrew J. Kaufman^{5,11,12}, Florent Ginhoux⁴, Jason D. Buenrostro⁷, Steven Z. Josefowicz^{8,9}, Alexander M. Tsankov^{1,3,5}, Thomas U. Marron^{1,2,3,5,11,12}, Sai Ma^{3,5}, Brian D. Brown^{1,2,3,5} & Miriam Merad^{1,2,5,10}✉

Monocyte-derived macrophages (mo-macs) often drive immunosuppression in the tumour microenvironment (TME)¹ and tumour-enhanced myelopoiesis in the bone marrow fuels these populations². Here we performed paired transcriptome and chromatin accessibility analysis over the continuum of myeloid progenitors, circulating monocytes and tumour-infiltrating mo-macs in mice and in patients with lung cancer to identify myeloid progenitor programs that fuel pro-tumorigenic mo-macs. We show that lung tumours prime accessibility for *Nfe2l2* (NRF2) in bone marrow myeloid progenitors as a cytoprotective response to oxidative stress, enhancing myelopoiesis while dampening interferon response and promoting immunosuppression. NRF2 activity is amplified during monocyte differentiation into mo-macs in the TME to regulate stress and drive immunosuppressive phenotype. NRF2 genetic deletion and pharmacological inhibition significantly reduced the survival and immunosuppression of mo-macs in the TME, restoring natural killer and T cell anti-tumour immunity and enhancing checkpoint blockade efficacy. Our findings identify a targetable epigenetic node of myeloid progenitor dysregulation that sustains immunoregulatory mo-macs in the lung TME and highlight the potential of early interventions to reprogram macrophage fate for improved immunotherapy outcomes.

A main focus in cancer immunotherapy has been reprogramming monocyte-derived macrophages (mo-macs) in the microenvironment of solid tumours to reverse immunosuppression and unleash T cell and/or natural killer cell responses³. Although this TME-centric approach has considerable merit, it fails to tackle the ‘wellspring’ of bone marrow (BM) myeloid progenitors seeding monocytes and mo-macs in the TME through tumour-driven myelopoiesis^{2,4}. Tumour-induced myelopoiesis has been observed across several cancers^{5–8}, but molecular mechanisms remain elusive. As our view of systemic tumour–host crosstalk expands, it becomes important to understand whether tumoural cues alter the molecular state of myeloid progenitors in BM, priming genes that ultimately affect anti-tumour responses. Understanding the mechanics of mo-mac replenishment and plasticity of mo-mac development during cancer inflammation is key to breaking the vicious cycle of tumour myelopoiesis, and developing more efficacious myeloid-targeting therapies.

Here we sought to identify epigenetic changes that prime myeloid progenitors in lung tumour-bearing hosts, probe their contribution towards pro-tumorigenic mo-macs in the TME, and harness this knowledge to redirect TME mo-mac fate towards an anti-tumour phenotype.

NSCLC influences chromatin state of BM progenitors

To characterize the impact of lung adenocarcinoma growth on myelopoiesis, we profiled progenitors and myeloid lineages in BM of naïve and *Kras*^{LSL-G12D/+}; *Trp53*^{fl/fl} (KP) tumour-bearing mice modelling non-small-cell lung cancer (NSCLC), at early (day 7), middle (day 15) and advanced (day 21) time points. We observed a marked increase in long-term haematopoietic stem cells (LT-HSC), multipotent common myeloid progenitors (CMP), granulocytic–monocytic progenitors (GMP) and committed monocyte progenitor (cMoP) by

¹Marc and Jennifer Lipschultz Precision Immunology Institute, Icahn School of Medicine at Mount Sinai, New York, NY, USA. ²Department of Immunology and Immunotherapy, Icahn School of Medicine at Mount Sinai, New York, NY, USA. ³Department of Genetics and Genomic Sciences, Icahn School of Medicine at Mount Sinai, New York, NY, USA. ⁴Institut Gustave Roussy, INSERM U1015, Villejuif, France. ⁵The Tisch Cancer Institute, Icahn School of Medicine at Mount Sinai, New York, NY, USA. ⁶Department of Immunology, Harvard Medical School, Boston, MA, USA. ⁷Department of Stem Cell and Regenerative Biology, Harvard Medical School, Boston, MA, USA. ⁸Immunology and Microbial Pathogenesis Program, Weill Cornell Graduate School of Medical Sciences, New York, NY, USA. ⁹Laboratory of Epigenetics and Immunity, Department of Pathology and Laboratory Medicine, Weill Cornell Medicine, New York, NY, USA. ¹⁰The Human Immune Monitoring Center, Icahn School of Medicine at Mount Sinai, New York, NY, USA. ¹¹Division of Hematology/Oncology, Icahn School of Medicine at Mount Sinai, New York, NY, USA. ¹²Center for Thoracic Oncology, Icahn School of Medicine at Mount Sinai, New York, NY, USA. ¹³These authors contributed equally: Bruno Giotti, Brian Y. Soong. ✉e-mail: miriam.merad@mssm.edu

Article

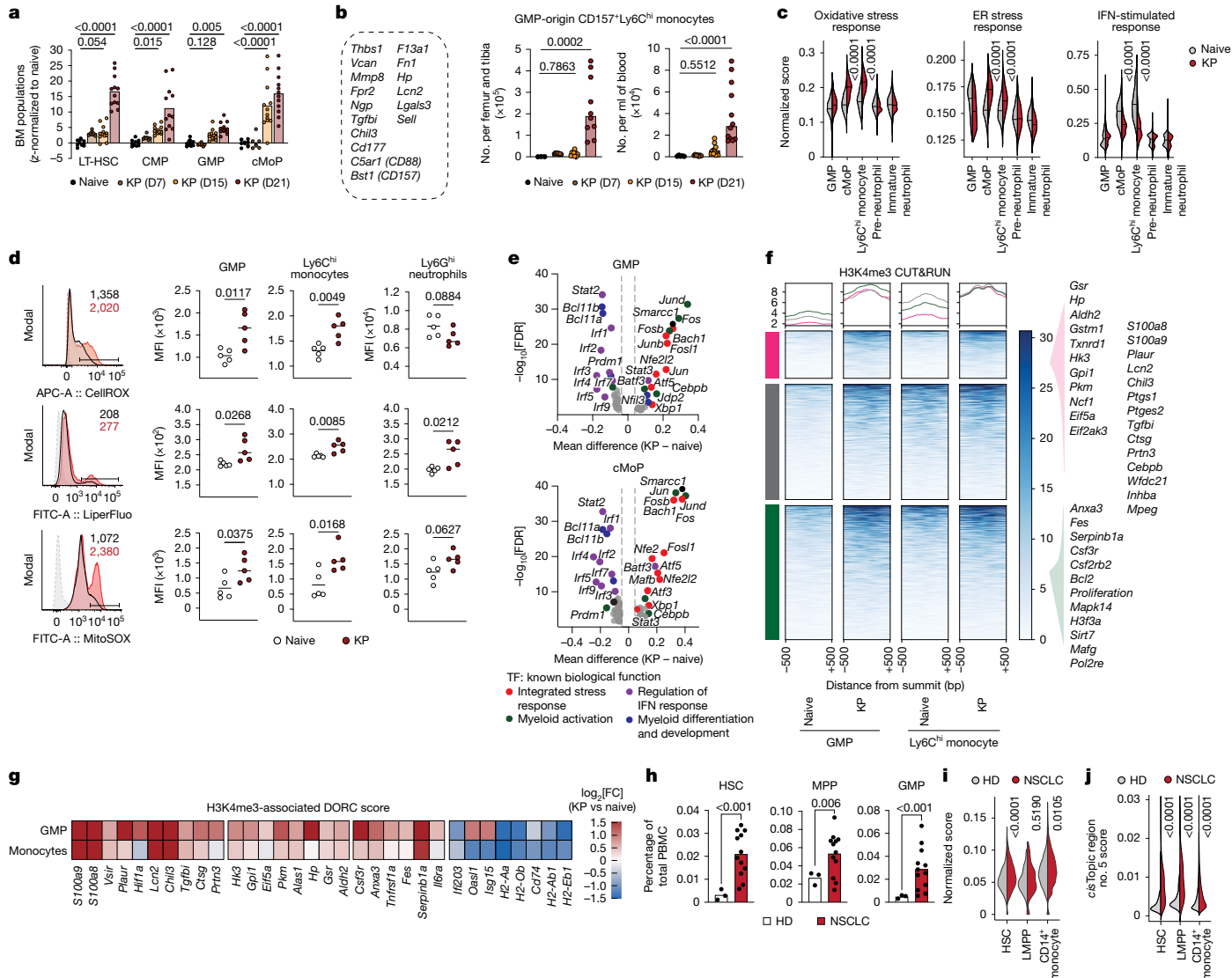


Fig. 1 | Lung cancer influences chromatin state of BM myeloid progenitors.

a, Relative abundance of LT-HSC, CMP, GMP and cMoP in BM of KP tumour-bearing mice at different time points, normalized to tumour-naive mice. Individual data points with bar denoting mean (left to right, $n = 10, 7, 12, 12$) from two experiments. **b**, Gene markers characterizing CD157⁺Ly6C^{hi} GMP-origin monocytes, with abundance in BM and blood of KP tumour-bearing mice at different time points. Individual data points with bar denoting mean (left to right, $n = 3, 7, 12, 12$) from two experiments. **c**, Normalized UCell-computed scores for oxidative stress response, endoplasmic reticulum (ER) stress response, and type I or III IFN-stimulated gene signature in BM cells of naive and KP tumour-bearing mice ($n = 3$ each). **d**, Representative histograms and quantification of CellROX, LiperFluo, MitoSOX median fluorescence intensity (MFI) in BM GMPs, Ly6C^{hi} monocytes and Ly6C^{hi} neutrophils from naive and KP tumour-bearing mice ($n = 5$ each). Individual data points with bar denoting mean, representative of two experiments. Grey dotted line, fluorescence-minus-one control; black line, naive; red line, KP. **e**, TF motifs differentially enriched in KP tumour-associated BM GMPs (top) and BM cMoPs (bottom) compared with

naive mice; ranked by false discovery rate (FDR). Dot colour indicates known biological pathways. Dashed lines indicate mean difference cut-off for visualization of most-deviated factors. **f,g**, H3K4me3 CUT&RUN signal clustering (**f**) and relative DORC scores for exemplar genes (**g**) in KP tumour-associated GMP and monocytes relative to naive. Units in **f** are normalized counts per million. **h**, Frequency of HSC, multipotent progenitors (MPP) and GMP in blood of patients with NSCLC ($n = 12$) and healthy donors (HD, $n = 3$). Pooled from three experiments. **i**, Normalized UCell-computed scores for oxidative stress response signature in indicated cells from patients with NSCLC ($n = 3$) and HD ($n = 2$). **j**, Normalized scores for cisTopic region 5 in HSC, lymphoid-myeloid primed multipotent progenitors (LMP) and monocytes from blood of patients with NSCLC ($n = 3$) compared with HD ($n = 2$). Per-cell distribution, pooled per group (**c,i,j**). Statistics computed by two-way analysis of variance (ANOVA) with Fisher's LSD test (**a**), one-way ANOVA with Dunnett's multiple comparison (**b**), unpaired two-tailed Student's t-test (**d,h**) or hypergeometric test with multiple correction (**c,i,j**). **D**, day; **FC**, fold change.

flow cytometry in BM of advanced KP tumour-bearing mice (Fig. 1a) alongside an increase in more mature myeloid populations (Extended Data Figs. 1a and 2a). BM progenitors from late-stage tumour-bearing mice formed markedly more granulocytic-monocytic colonies than erythroid colonies and proliferated more than their tumour-naive counterparts (Extended Data Fig. 1b,c). In addition, we observed an increased mobilization of Ly6C^{hi} monocytes and Ly6C^{hi} neutrophils in circulation tracking with tumour burden (Extended Data Figs. 1d

and 2b). We also observed an expansion of GMP-derived CD157⁺Ly6C^{hi} neutrophil-like monocytes in the BM and peripheral blood of late-stage tumour-bearing mice (Fig. 1b), previously described to expand in emergency conditions and engender oxidative burst-associated degranulation gene programs^{9,10}. We observed a similar expansion of GMPs, cMoPs and CD157⁺Ly6C^{hi} monocytes in the *Kras*^{LSL-G12D/+;Trp53fl/fl genetically engineered mouse model (GEMM) (Extended Data Fig. 1e) and ruled out any contribution of bone metastases (Extended Data Fig. 2c).}

Given that such myeloid expansion is driven by malignancy, we probed how molecular programs are transcriptionally and epigenetically rewired in myeloid progenitors in response to peripheral tumour cues. Experimentally, we used single-cell RNA sequencing (scRNA-seq) to interrogate myeloid progenitor lineages broadly sorted from the BM of age-matched naive and advanced tumour-bearing mice (Extended Data Fig. 2d). We identified distinct granulocytic (granulocytic progenitor, pre-neutrophil, immature neutrophil) and monocytic (cMoP, Ly6C^{hi} monocyte, Ly6C^{low} monocyte) lineages (Extended Data Fig. 1f and Supplementary Table 2). We focused on monocytic lineage progenitors (GMP and cMoP) because they are the main source of suppressive mo-macs in tumours¹¹. Differentially upregulated genes in tumour-educated GMPs and cMoPs were associated with biological processes such as ‘response to reactive oxygen species (ROS)’, ‘hypoxia response’, ‘regulation of apoptosis’ and ‘metabolic regulation of superoxide generation’, which was supported in other datasets of tumour-driven myelopoiesis^{12,13} (Extended Data Fig. 1g,h). Tumour-associated BM myeloid progenitors and Ly6C^{hi} monocytes also had higher gene signature scores for oxidative stress response and ER stress response (Fig. 1c and Supplementary Table 1) while exhibiting increased cellular ROS burden, lipid peroxidation and mitochondrial oxidative stress as measured by flow cytometry (Fig. 1d).

Using scRNA-seq profiles of myeloid cells with paired small-cell ATAC sequencing (scATAC-seq) data, we then correlated gene programs in each myeloid cell state to chromatin accessibility (Extended Data Fig. 1i) and focused on transcription factors (TF) driving downstream gene programs. Lineage-determining TF motifs enriched in GMP marker regions included GATA2, TAL1 and LY1 (ref. 14), whereas cMoPs and monocyte marker regions were enriched in IRF4 and SPIB¹⁵ (Extended Data Fig. 1j). We then sought to identify TF motifs enriched in differentially accessible regions of tumour-associated cell states. In line with our transcriptional results, tumour-associated GMPs and cMoPs had increased motif accessibility for oxidative stress-responsive TFs such as NFE2L2, BACH1, FOSL2, ATF4, ATF5, NFIL3, STAT3 and XBP1 (ref. 16), AP-1 factors such as JUND, JUN and FOS, and granulocytic fate regulators CEBPB and CEBPA¹⁷ (Fig. 1e), when compared with naive counterparts. These observations were further supported by our analysis of histone CUT&RUN data showing H3K4me3 signal (enriched proximal to promoter regions) was gained in tumour-associated myeloid progenitors in genomic regions associated with oxidative stress handling, detoxification, chromatin remodelling and proliferation (Fig. 1f and Extended Data Fig. 1k). Enhancer-associated H3K4me1 and H3K27ac signal augmented in tumour-associated GMPs was associated with pathways involved in cellular detoxification, immunoregulation and anti-apoptotic or pro-survival pathways (Extended Data Fig. 1l). Domains of regulatory chromatin (DORC) scores calculated on H3K4me3 signal–gene association highlighted genes involved in inflammation regulation (for example, *S100a8*, *S100a9*, *Hif1a*, *Chil3*, *Lcn2* and *Prtn3*), metabolic adaptation under oxidative stress (for example, *Hk3*, *Eif5a*, *Pkm*, *Gpi1*, *Gsr* and *Aldh2*) and mitogen-induced survival (for example, *Anxa3*, *Tnfrsf1a* and *Serpinb1a*) activated in KP-experienced GMPs (Fig. 1g and Methods). On the other hand, we observed a reduction of type I or III interferon (IFN)-stimulated gene expression in tumour-associated BM myeloid progenitors, supporting a damped inflammatory state^{18,19} distal to the TME (Fig. 1c). The reduced chromatin accessibility for several IFN pathway TFs including IRF3, IRF7, IRF5 and STAT2 (Fig. 1e), lower H3K4me3-associated DORC scores at IFN-stimulated gene (ISG) loci such as *Ifi203*, *Oasl1* and *Isg15* (Fig. 1g) and lower H3K4me1-associated and H3K27ac-associated DORC scores complemented by higher H3K27me3 repressive histone mark at gene loci such as *Ifitm3*, *Ms4a4c*, *Mx1* and *Gbp4* in tumoural BM myeloid progenitors (Extended Data Fig. 1m) further supported our transcriptomic findings of IFN hyporesponsiveness. These results collectively suggested that tumour-associated myelopoiesis drives priming of pathways in BM GMPs involved in the ROS stress response²⁰,

mitochondria–ER metabolic adaptations²¹ and IFN hypo-responsiveness to limit exhaustion²². We identified certain binding motifs for TFs such as *Nfe2l2* to be enriched in promoter-proximal activating histone marks of tumoural myeloid progenitors, unlike TFs such as *Gata2*, *Mesp1*, *Glis2* and *Tcf3* that are enriched at more distal H3K4me1 and H3K27ac enhancer-associated signal (Extended Data Fig. 1n).

Subsequently, we quantified mobilized progenitor populations in the blood of patients with early-stage NSCLC and found that HSCs, multipotent progenitors (MPPs) and GMPs were elevated in peripheral blood from patients with early-stage NSCLC when compared with healthy donors (Fig. 1h and Extended Data Fig. 2e). We next conducted a 10x Multiome (RNA + ATAC) assay on peripheral blood mononuclear cells (PBMCs) from patients with NSCLC, to interrogate molecular changes. Mirroring our findings in mice, CD14⁺ monocytes from peripheral blood of patients with early NSCLC had increased oxidative stress response signature scores (Fig. 1i and Extended Data Fig. 1o) and accessible chromatin topics enriched in these patients were associated with ‘MAPK signalling activation’, ‘metabolic processes’, ‘response to ROS’ and ‘response to oxidative stress’ (Fig. 1j and Extended Data Fig. 1p). In support, genes differentially expressed in monocytes from patients with NSCLC were downstream of TF regulators such as NFE2L2, STAT3, PPARG and MYC (Extended Data Fig. 1q). Thus, cancer-associated inflammation provokes demand-adapted mobilization of myeloid-biased progenitors associated with oxidative stress-responsive epigenomic remodelling.

Tumour-induced myelopoiesis fuels TME mo-macs

To measure whether imprinting of stress-responsive programs in BM myeloid progenitors upon sensing systemic tumour cues influence mo-mac states in the TME, we adoptively transferred GMPs from either tumour-bearing mice or naive mice into a tumour-bearing congenic host (Extended Data Fig. 2f). We found mo-macs derived from tumour-primed GMPs to be more immunoregulatory in the TME, characterized by increased differentiation into GPNMB⁺CD9⁺TREM2^{hi} mo-macs²³ expressing higher PD-L1, increased ARG1⁺ mo-macs²⁴ and decreased frequency of CD86⁺MHCII⁺ immunostimulatory mo-macs (Fig. 2a and Extended Data Fig. 3a–c). In addition, we differentiated BM-derived macrophage (BMDM) ex vivo in the presence of tumour conditioning (CM) either early or later during the differentiation. Early exposure to tumour inflammatory cues significantly enhanced mo-mac suppressive phenotype compared with late exposure (Extended Data Fig. 3d). Transient incubation of BM progenitors with KP CM also cues a more immunoregulatory phenotype in progeny macrophages (Extended Data Fig. 3e). These results collectively suggest that exposure of myeloid progenitors to tumour cues affected their ultimate trajectory in the TME.

Using paired scRNA-seq and scATAC-seq analysis of myeloid cells isolated from naive and tumour-bearing lungs (Extended Data Fig. 2g), we identified discrete inflammatory Ly6C^{hi} monocytes, patrolling Ly6C^{low} monocytes, resident tissue alveolar macrophages, interstitial macrophages and mo-mac subsets such as ARG1^{hi} mo-macs and TREM2^{hi} mo-macs (Extended Data Fig. 4a). Using gene–gene correlation, we identified a module of genes implicated in anti-apoptotic cytoprotection, glycolytic metabolic shift and regulation of oxidative stress that was highly enriched in tumour-infiltrating ARG1^{hi} mo-macs and TREM2^{hi} mo-macs (Extended Data Fig. 4b, Supplementary Table 2 and Methods), regulated by TFs such as STAT3, NFE2L2, HIF1A, KLF4, SPI1 and CEBPB. We captured a similar diversity of tumour-infiltrating myeloid cells in the scATAC-seq data through independent clustering of chromatin accessibility features (Extended Data Fig. 4c), which aligned with cell-type-specific enrichment of lineage-determining TF motifs (Extended Data Fig. 4d). TFs for oxidative stress response, including *Nfe2l2*, *Fosl2* and *Bach1*, were specifically enriched in tumour-dominant ARG1^{hi} and TREM2^{hi} mo-macs. Phenotypically, Ly6C^{hi} monocytes infiltrating KP tumours exhibited a higher oxidative stress burden (Extended

Article

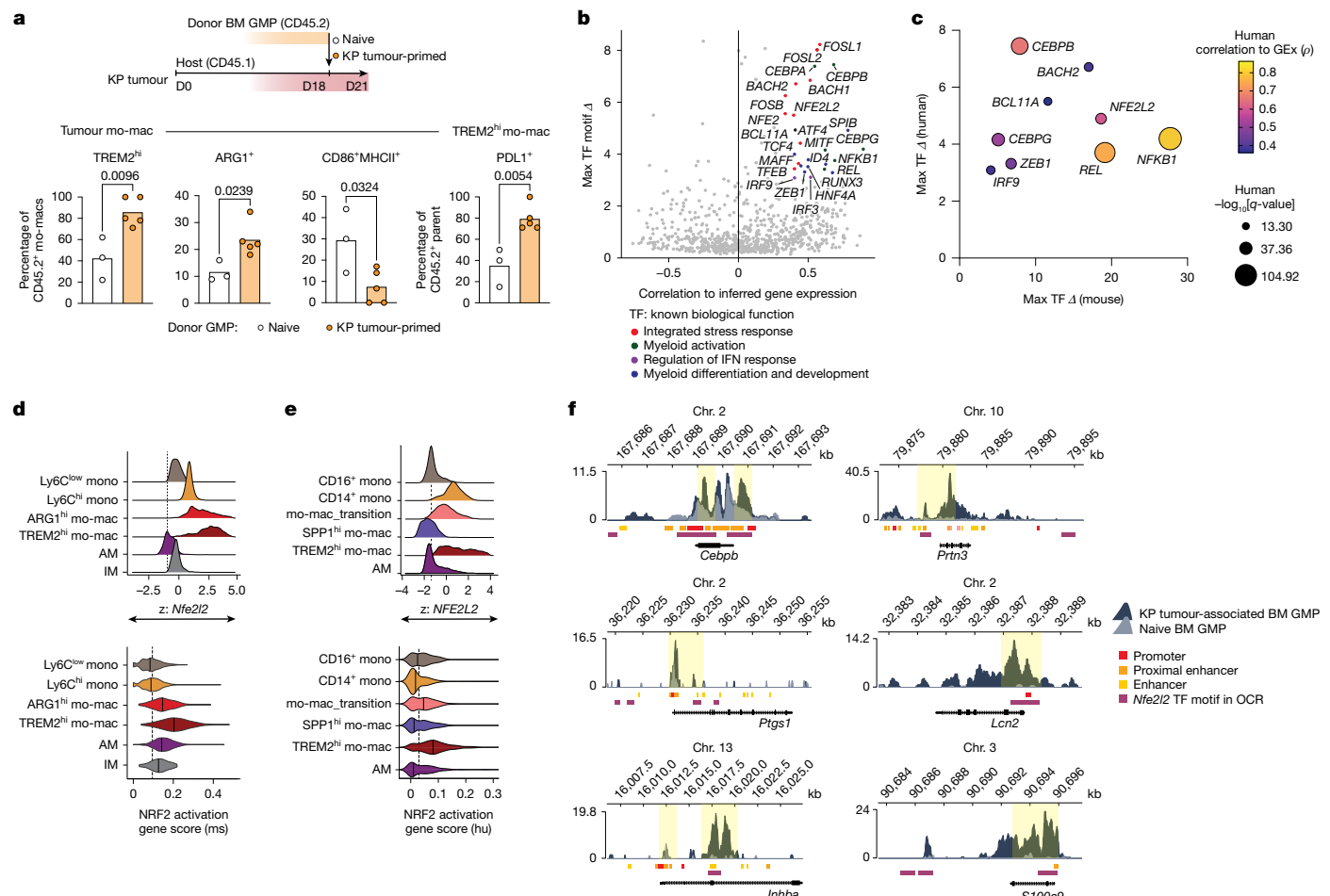


Fig. 2 | Tumour-induced myelopoiesis fuels mo-macs in TME with sustained cytoprotective stress response. **a**, In vivo tracing of naive ($n = 3$) and KP tumour-primed ($n = 5$) BM GMPs sorted at day 17 and transferred to KP tumour-bearing CD45.1 hosts, with frequency of donor-derived CD45.2⁺TREM2^{hi}, ARG1⁺ and CD86⁺MHCII⁺ mo-macs, and frequency of donor-derived CD45.2⁺TREM2^{hi} mo-macs expressing PD-L1 four days post transfer. Individual data points are shown with a bar denoting the mean, representative of two independent experiments. **b**, Candidate TF regulators in tissue-infiltrating monocyte and mo-macs of patients with NSCLC, prioritized by maximum TF motif deviation (Δ) across clusters. **c**, Top-quartile TF regulators conserved in both mouse and

human analysis, ranked by correlation to human TF gene expression (GEx).

d,e, ChromVAR motif deviation for *Nfe2l2* and UCell-computed score for NRF2 downstream gene program activation in mouse tumour-infiltrating myeloid cell clusters ($n = 4$ pooled) (**d**) and human NSCLC-infiltrating myeloid cell clusters ($n = 14$ pooled) (**e**). **f**, Browser plots at indicated gene loci for H3K4me3 CUT&RUN signal in KP tumour-associated and naive GMPs. Highlighted regions indicate differential signal near known *cis*-regulatory elements and open chromatin regions (OCRs) containing *Nfe2l2* motif. Statistics computed by unpaired two-tailed Student's *t*-test (**a**). AM, alveolar macrophage; chr., chromosome; IM, interstitial macrophage; ms, mouse; hu, human.

Data Fig. 3f) and intratumoural TREM2^{hi} mo-macs had relatively higher amounts of cytosolic ROS when compared with immunostimulatory mo-macs (Extended Data Fig. 3g). In light of our findings in BM myeloid progenitors, these results suggested that oxidative stress-induced cytoprotective chromatin changes initiated in tumour-educated myeloid progenitors are maintained in tumoural mo-macs.

We simultaneously used paired single-cell chromatin accessibility and gene expression profiling to analyse tumour-infiltrating immune cells isolated from 14 human NSCLC lesions (Supplementary Table 3). On the basis of marker gene-based filtering in our 10x Multiome dataset from 5 patients, we isolated 4,177 myeloid cells and classified them according to their nuclear RNA-seq profiles and by weighted gene correlation network analysis (Extended Data Fig. 4e). Tumour-infiltrating myeloid cells included CD14⁺ monocyte clusters, a transitional mo-mac state that exhibits monocytic features and macrophage markers such as *MRC1*, *CD68* and *C1Q4*; SPP1^{hi} mo-macs²⁵ characterized by *SPP1*, *FBP1* and *IL4I1*; and TREM2^{hi} mo-macs²⁶ characterized by *GPNMB*, *CD9*, *TREM2* and *PPARG* (Extended Data Fig. 4f and modules in Supplementary Table 4). We integrated the cellular identity from Multiome samples with 24,346 scATAC-seq-captured myeloid cells from 9 patients (Extended Data

Fig. 4g). In close agreement with our mouse analyses, we observed motifs for TFs such as *NFE2L2*, *FOSL2*, *JUN* and *BACH1* to be enriched in marker peaks of tumour-infiltrating activated CD14⁺ monocytes, mo-mac_transition and TREM2^{hi} mo-macs (Extended Data Fig. 4h).

Subsequently, we prioritized TF regulators with sustained cell-type-specific activity in TME-infiltrating immunosuppressive mo-macs. Putative TF regulators in our mouse dataset included *Spi1*, *Mafb* and *Cebpb*, as well as NF- κ B or Rel family members and AP-1 family members associated with response to inflammation and growth factors²⁷ (Extended Data Fig. 4i). Strikingly, we again observed a nexus of stress-responsive TFs, principally *Nfe2l2*, *Bach1*, *Fosl2*, *Mafk* and *Mafg*. Concurrent analyses in our human NSCLC dataset of TME monocytes and mo-macs indicated very similar candidate regulators such as *NFKB1*, *REL*, *SPIB* and *CEBPB* but also oxidative stress response and integrated stress response regulators *NFE2L2*, *BACH1*, *MAFF*, *FOSL2* and *ATF4* (Fig. 2b). Downstream pathways conserved across mouse and human TME mo-macs included ‘heme signalling’, ‘cytoprotection by HMOX1’, ‘response to ER stress’ and ‘mitochondrial biogenesis’ (Extended Data Fig. 4j) and ranking on the basis of correlation to gene expression prioritized *NFKB1*, *REL*, *CEPB*, *CEBPG* and *NFE2L2* (Fig. 2c).

NRF2 signalling dampens IFN response in the TME

We were especially interested in NRF2 because of its role in driving antioxidant gene batteries, promoting resistance to lipid-associated ferroptosis and opposing NF- κ B pro-inflammatory cascades^{28,29}. NRF2 can also directly influence pro-inflammatory signals by suppressing type I IFN pathway genes and limiting inflammasome activation^{30–33}. In the lung, we observed relative TF motif deviation for NRF2 and aggregate score for NRF2 downstream gene activation to be highest in immunoregulatory ARG1^{hi} and TREM2^{hi} mo-macs that accumulate in late-stage tumours³⁴ (Fig. 2d). We did not rely on *Nfe2l2* gene expression alone, because NRF2 is regulated post-transcriptionally and post-translationally. As a proxy for activation of NRF2 programs in vivo, we assayed the amounts of nuclear NRF2 and intracellular heme oxygenase (HO-1, encoded by *Hmox1*)³⁵. TREM2^{hi} mo-macs had increased amounts of NRF2 and HO-1 compared with CD86⁺MHCII⁺ mo-macs in KP tumours (Extended Data Fig. 3h), and mo-macs in KP GEMM also had increased amounts of NRF2 (Extended Data Fig. 5a). Similarly, in human NSCLC, NRF2 TF motif deviation was highest in immunosuppressive TREM2^{hi} mo-macs and recently infiltrated monocytes (mo-mac_transition), with concomitantly high NRF2 downstream gene activation (Fig. 2e). Furthermore, we found the NRF2 activation score to be highest in tumour-associated TREM2^{hi} mo-macs across two independent scRNA-seq datasets^{36,37} (Extended Data Fig. 3i and Methods).

Given the persistent NRF2 pathway activation in TME immunosuppressive mo-macs, we next explored when NRF2 was activated during GMP differentiation to monocytes and mo-macs. We observed increased NRF2 activation and HO-1 induction in mo-macs that differentiate in vivo from adoptively transferred tumour-experienced BM GMPs, and myeloid progenitors exposed to early transient tumour conditioning (Extended Data Fig. 3j,k). GMPs isolated from KP tumour-bearing mice had increased H3K4me3 promoter-proximal signal at known NRF2 oxidative stress response genes such as *Gclm*, *Alas1*, *Gsr*, *Prtn3* and *Txnd1* (Extended Data Fig. 3l), but also key immunosuppressive gene loci such as *Cebpb*, *Ptgs1* (ref. 38), *Inhba*³⁹, *Lcn2* (ref. 40) and *S100a8* (ref. 41) (Fig. 2f), suggesting imprinting of immunoregulatory programs early in differentiation. Crucially, although we observed tumour-educated BM GMPs and monocytes had increased NRF2 motif accessibility compared with their tumour-free counterparts, this was not matched by activation of downstream gene programs (Extended Data Fig. 5b). Given the downregulation of the IFN-stimulated response in tumour-experienced BM myeloid cells, we next tested the temporal relationship of IFN responsiveness with NRF2 activation. For this, we implanted lung tumours in *Mx1*^{GFP} IFN-sensitive response element reporter mice⁴². Here tumour-associated monocytes across tissue compartments and tumoural mo-macs had consistently lower GFP expression than their naive counterparts, indicating lower IFN responsiveness (Extended Data Fig. 5c). Strikingly, there was a stepwise increase in *Mx1*^{GFP} as monocytes infiltrated the tumour, followed by waning in TME mo-macs concomitant with NRF2 activation (Extended Data Fig. 5c,d). Several ISGs and antigen-presentation-associated gene loci are potentially regulated by NRF2 and partner TFs at distal enhancer loci, as evident from reduced H3K27ac CUT&RUN marks in KP-experienced GMPs at loci such as *Mx1*, *Ifitm1*, *Slamf7* and *H2-Ab1* (Extended Data Fig. 5e). These results collectively suggested that exposure of BM myeloid progenitors to tumour cues primes NRF2 response loci and certain immunosuppressive gene loci, which promotes a more immunoregulatory fate for mo-macs in the TME with a dampened type I or III IFN response.

Tumour cues activate NRF2 in BM progenitors

Taking a candidate approach to identify cues that activate NRF2, we found protein factors to be the dominant trigger in tumour CM (Extended Data Fig. 6a,b). Specifically, factors such as granulocyte-macrophage

colony-stimulating factor (GM-CSF), granulocyte colony-stimulating factor (G-CSF) and interleukin 6 were enriched in BM sera, blood sera and tumour CM (Extended Data Fig. 6d–f). GM-CSF and interleukin 6 mimicked the impact of tumour CM on myelopoiesis, resulting in NRF2 activation, increased HO-1 expression and increased proliferation (Extended Data Fig. 6g,h). The myelopoietic effects of KP CM were ameliorated by incubating progenitors with anti-GM-CSF and anti-interleukin 6 neutralizing antibodies, associated with a reduction in oxidative stress burden (Extended Data Fig. 6i,j). Although there was a reduction in myeloid expansion and HO-1 expression upon incubating progenitors with KP CM in the presence of ML385—an inhibitor of *Nfe2l2* DNA binding and transcriptional activity⁴³ (Extended Data Fig. 6k)—there was an increase in oxidative burden (Extended Data Fig. 6l) suggestive of stress response uncoupling. We found that stress-responsive p38 MAPK signalling was induced in KP CM-experienced progenitors (Extended Data Fig. 6m) but was not affected by ML385 (Extended Data Fig. 6n); this suggested NRF2 pathway activation to be downstream of stress-responsive signal transduction from mitogenic cues such as GM-CSF and interleukin 6. Incubating progenitors with GM-CSF and interleukin 6 in the presence of p38 MAPK inhibitor ameliorated myelopoietic expansion as well as HO-1 expression in conjunction with reducing cellular ROS burden (Extended Data Fig. 6o,p). Although we do not exclude other signals in the TME such as heme⁴⁴, our results indicate that NRF2 activation in BM due to tumour mitogen-induced oxidative stress enables progenitors to continue expanding to meet inflammatory demand (Extended Data Fig. 6q).

NRF2 regulates mo-mac function in the TME

Having established the role of NRF2 in BM myeloid expansion, we interrogated the functional consequence of NRF2 in tumour-associated myeloid cell survival and immunosuppression. Exposing BMDMs to tumour CM during the last 24 h of culture (to mimic polarization in the TME) resulted in immunosuppressive gene activation, cytoprotection and IFN response suppression (Extended Data Fig. 7a). When we cultured BMDMs from NRF2 constitutive knockout mice (*Nfe2l2*^{TKO}) or wild-type counterparts in the presence of KP CM, we found that tumour-conditioned *Nfe2l2*^{TKO} BMDMs had lower relative activation of *Arg1*, *Retnla* and *Chil3*, while concomitantly expressing higher amounts of the ISGs *Mx1* and *Nos2* (Fig. 3a). Adding ML385 at day 6 resulted in a similar phenotype (Extended Data Fig. 7b). Remarkably, tumour-educated *Nfe2l2*^{TKO} BMDMs exhibited increased ROS burden, lipid peroxidation and mitochondrial stress, and increased sensitivity to cell death (Extended Data Fig. 7c,d). This susceptibility for cell death under redox crisis was specific to tumour condition, because *Nfe2l2*^{TKO} BMDMs did not exhibit increased cell death at steady state (Extended Data Fig. 7e). Viable tumour-educated *Nfe2l2*^{TKO} BMDMs had reduced expression of HO-1, ARG1 and PD-L1 with increased expression of MHCII, CD86 and CD40 (Fig. 3b), indicating a phenotypic shift towards immunogenicity and antigen presentation.

Next, we generated conditional knockout mice, wherein NRF2 is floxed by Cre recombinase under the *Ms4a3* promoter (*Nfe2l2*^{ΔMs4a3}) restricted to GMPs⁴⁵, resulting in decreased NRF2 activity. Myelopoiesis, differentiation and monocyte function in these mice were unaltered at the steady state (Extended Data Fig. 7f–i). We adoptively transferred GMPs from CD45.2 *Nfe2l2*^{ΔMs4a3} or *Nfe2l2*^{f/f} control BM into congenic CD45.1 hosts bearing KP tumours, and found that GMPs from *Nfe2l2*^{ΔMs4a3} mice differentiated into more immunostimulatory CD86⁺MHCII⁺ mo-macs and strikingly fewer TREM2^{hi} mo-macs in the lung TME, with the TREM2^{hi} mo-macs having decreased PD-L1 (Fig. 3c). GMPs derived from KP-experienced mice treated with quassinoid NRF2 inhibitor Brusatol⁴⁶, when similarly transferred into congenic tumour-bearing mice, differentiated into more immunostimulatory mo-macs (Fig. 3d). Remarkably, GMPs from tumour-naive mice administered antioxidant N-acetyl cysteine (NAC) differentiated into mo-macs with increased

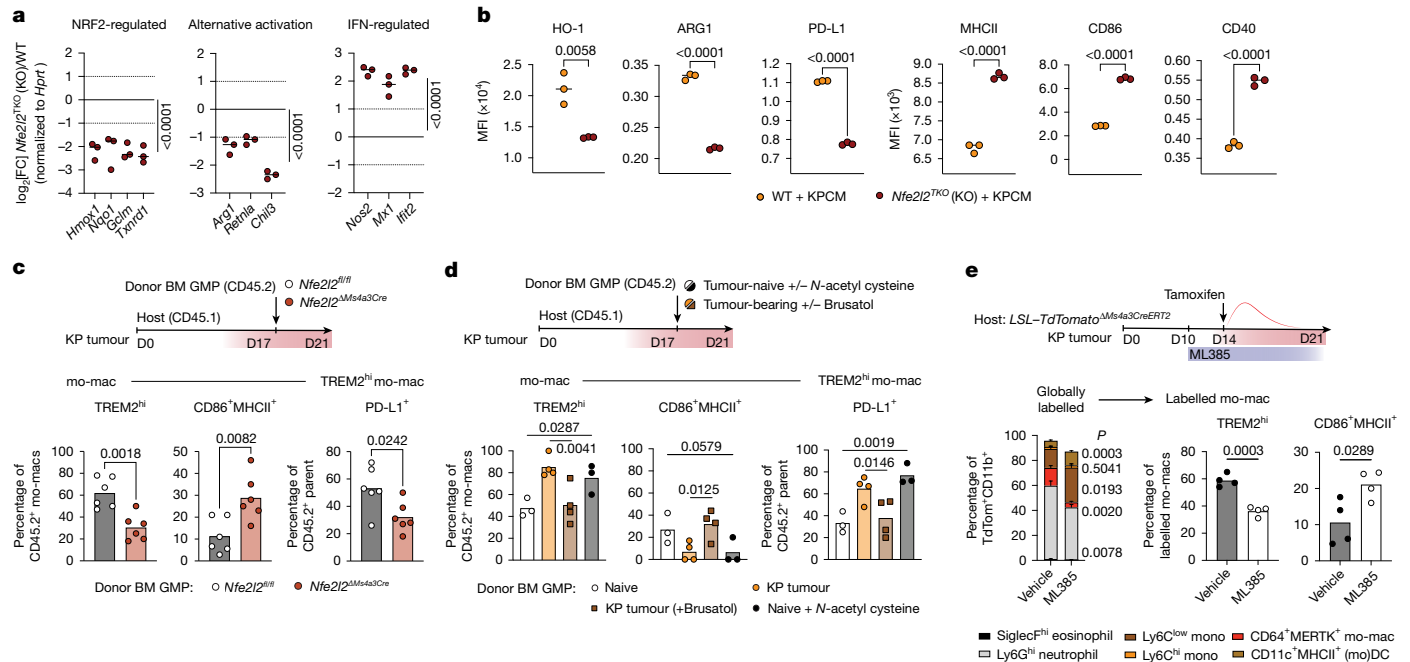


Fig. 3 | NRF2 signalling is a regulator of mo-mac persistence and immunosuppressive function in the lung TME. **a**, Gene expression in KPCM-exposed *Nfe2l2*^{TKO} (KO) BMDMs as measured by reverse transcription quantitative polymerase chain reaction (RT-qPCR). Relative values depicted as fold change compared with NRF2-proficient wild-type BMDMs, after normalization to *Hprt* expression. *n* = 3 replicates, representative of two independent experiments. **b**, MFI of HO-1, ARG1, PD-L1 and MHCII, CD86, CD40 in KPCM-exposed *Nfe2l2*^{TKO} (KO, *n* = 3), or control (WT, *n* = 3) BMDMs. Representative of two independent experiments. **c**, In vivo tracing of BM GMPs transferred from *Nfe2l2*^{ΔMs4a3} mice (*n* = 6) or *Nfe2l2*^{fl/fl} control littermates (*n* = 6) into KP tumour-bearing congenic CD45.1 hosts, with frequency of donor-derived TREM2^{hi} mo-macs, CD86⁺MHCII⁺ mo-macs and frequency of donor-derived TREM2^{hi} mo-macs expressing PD-L1 4 days post transfer. Representative of two independent experiments. **d**, In vivo tracing of indicated GMPs from

Brusatol-treated tumour-bearing mice or N-acetyl cysteine-treated tumour-naive mice transferred into KP tumour-bearing CD45.1 hosts, with frequency of donor-derived TREM2^{hi} mo-macs, CD86⁺MHCII⁺ mo-macs and frequency of donor-derived TREM2^{hi} mo-macs expressing PD-L1 4 days post transfer (left to right, *n* = 3, 4, 4, 3). Representative of two independent experiments. **e**, In vivo tracing of myeloid cells in KP tumour-bearing *LSL-TdTomato*^{ΔMs4a3CreERT2} mice administered ML385 (*n* = 4) or vehicle (*n* = 4) starting on day 10 and tamoxifen-pulse labelled at day 14, with quantification of labelled TdTomato⁺CD11b⁺ myeloid cells (left), and frequency of TREM2^{hi} and CD86⁺MHCII⁺ phenotype in labelled CD64⁺MERTK⁺ mo-macs (right) at day 21. Error bars in stacked bar plot indicate mean values ± s.e.m. Representative experiment. Statistics computed by two-way ANOVA with Fisher's LSD test (**a,d**) and unpaired two-tailed Student's *t*-test (**b,c,e**). +/-, with or without; DC, dendritic cell; mono, monocyte; TdTom, TdTomato.

immunosuppressive phenotype (Fig. 3d and Extended Data Fig. 7j). Thus, manipulating ROS burden and NRF2 activation in BM GMPs influenced subsequent mo-mac phenotype in the TME.

NRF2 enhances immunoregulatory myelopoiesis

Considering that peripheral tumours can promote NRF2 priming in BM myeloid progenitors, we interrogated how loss of NRF2 signalling functionally affects myelopoiesis. To do so, we first administered NRF2 inhibitor ML385 in KP tumour-bearing *LSL-TdTomato*^{ΔMs4a3CreERT2} reporter mice and pulsed with one dose of tamoxifen to trace the fate of recently emigrated GMP-derived cells in the TME. NRF2 inhibition resulted in a reduction of TdTomato-labelled intratumoural mo-macs and neutrophils 8 days post-tamoxifen, with a significant reduction in the frequency of TREM2^{hi} mo-macs (Fig. 3e). Consequently, we implanted KP tumours orthotopically in *Nfe2l2*^{ΔMs4a3} and *Nfe2l2*^{fl/fl} mice. *Nfe2l2*^{ΔMs4a3} mice had a significant reduction in KP burden and greater overall survival (Fig. 4a and Extended Data Fig. 8a). Similar results were obtained in the LLC1 lung cancer model and the B16-F10 model of melanoma lung metastases (Extended Data Fig. 8b). We also generated transgenic mice, wherein the Kelch-like ECH-associated protein 1 (KEAP1) locus was floxed under Ms4a3Cre (*Keap1*^{ΔMs4a3}) resulting in GMP-restricted loss of KEAP1, a component of the Cullin 3-based E3 ubiquitin ligase complex controlling the stability of NRF2, leading to sustained NRF2 activity and an increase in NRF2 downstream programs. KP tumours were significantly larger in *Keap1*^{ΔMs4a3} mice when compared with

littermates (Extended Data Fig. 8c). We next assessed myelopoiesis in *Nfe2l2*^{ΔMs4a3} mice. Although NRF2 deletion did not affect steady-state myelopoiesis (Extended Data Fig. 7f,g), tumour-bearing *Nfe2l2*^{ΔMs4a3} mice had significant contraction of BM CMP, GMP and cMoP numbers (Fig. 4b). Reduced NRF2 in tumoural mo-macs of *Nfe2l2*^{ΔMs4a3} mice was associated with a reduction in the number of PD-L1-expressing TREM2^{hi} mo-macs in the TME and a compensatory increase in CD86⁺MHCII⁺ immunogenic mo-macs (Fig. 4c,d). Notably, TREM2^{hi} mo-macs in the TME of *Nfe2l2*^{ΔMs4a3} mice were more susceptible to cell death (Extended Data Fig. 8d), providing rationale for the phenotypic shift in the TME. The mo-mac distribution in *Keap1*^{ΔMs4a3} mice was tumour-promoting, with more abundant TREM2^{hi} mo-macs in the TME expressing PD-L1 (Extended Data Fig. 8e).

To measure the cell-intrinsic effect of NRF2 activation on myelopoiesis independent of tumour burden differences, we created mixed-BM chimeras with 1:1 reconstitution of CD45.2 *Nfe2l2*^{ΔMs4a3} and CD45.1 *Nfe2l2*^{WT} mice (Extended Data Fig. 8f). We observed decreased expansion of *Nfe2l2*^{ΔMs4a3} donor-derived GMPs in BM and lower mobilization of *Nfe2l2*^{ΔMs4a3} CD157⁺Ly6C^{hi} monocytes in peripheral blood (Extended Data Fig. 8g). Consequently in the lung, TREM2^{hi} mo-macs of *Nfe2l2*^{ΔMs4a3} origin were also relatively less abundant, whereas CD86⁺MHCII⁺ mo-macs were increased (Extended Data Fig. 8h). Integrated scRNA-seq and scATAC-seq on the myeloid progenitor lineages in tumour-bearing *Nfe2l2*^{ΔMs4a3} mice and control counterparts (Extended Data Fig. 8i) showed the most differentially expressed genes (DEGs) and differentially accessible regions (DARs) to be in GMPs and

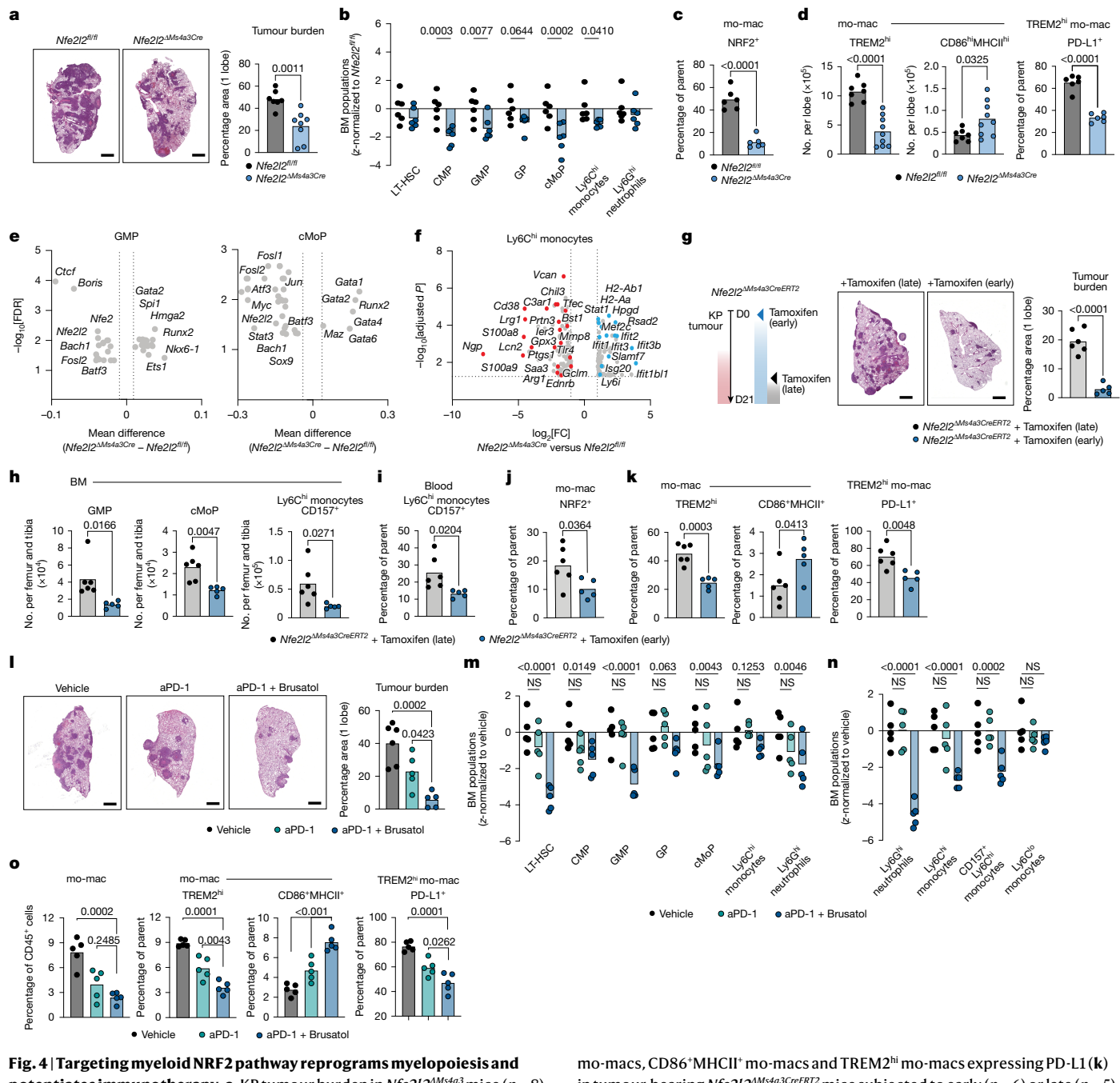


Fig. 4 | Targeting myeloid NRF2 pathway reprograms myelopoiesis and potentiates immunotherapy. **a**, KP tumour burden in *Nfe2l2*^{ΔMs4a3} mice ($n = 8$) or *Nfe2l2*^{fl/fl} littermates ($n = 7$). **b**, Relative abundance of LT-HSC, myeloid progenitors and mature populations in BM of tumour-bearing *Nfe2l2*^{ΔMs4a3} mice ($n = 6$), normalized to *Nfe2l2*^{fl/fl} littermates ($n = 6$). **c**, Nuclear NRF2 in tumour-infiltrating mo-macs of *Nfe2l2*^{ΔMs4a3} ($n = 6$) or *Nfe2l2*^{fl/fl} mice ($n = 6$). **d**, Number of tumour-infiltrating TREM2^{hi} mo-macs, CD86⁺MHCII⁺ mo-macs in *Nfe2l2*^{ΔMs4a3} ($n = 9$) or *Nfe2l2*^{fl/fl} mice ($n = 7$), and TREM2^{hi} mo-macs expressing PD-L1 in *Nfe2l2*^{ΔMs4a3} ($n = 6$) or *Nfe2l2*^{fl/fl} mice ($n = 6$). **e**, TF motifs differentially enriched in KP tumour-bearing *Nfe2l2*^{ΔMs4a3} GMP (left) and cMoP (right) compared with *Nfe2l2*^{fl/fl}. Dashed lines indicate mean difference cut-off for visualization of most-deviated factors. **f**, DEGs in tumour-infiltrating Ly6C^{hi} monocytes of *Nfe2l2*^{ΔMs4a3} mice compared with *Nfe2l2*^{fl/fl}. **g**, Tumour burden after early ($n = 6$) or late ($n = 5$) deletion of NRF2 in *Nfe2l2*^{ΔMs4a3CreERT2} mice. **h–k**, Number of GMP, cMoP and CD157⁺Ly6C^{hi} monocytes in BM (**h**), frequency of CD157⁺Ly6C^{hi} monocytes in blood (**i**), nuclear NRF2 in mo-macs (**j**) and number of TREM2^{hi}

mo-macs, CD86⁺MHCII⁺ mo-macs and TREM2^{hi} mo-macs expressing PD-L1 (**k**) in tumour-bearing *Nfe2l2*^{ΔMs4a3CreERT2} mice subjected to early ($n = 6$) or late ($n = 5$) deletion of *Nfe2l2*. **l**, Tumour burden at day 21 in mice treated with Brusatol (NRF2 inhibitor) and anti-PD-1 (aPD-1) ($n = 5$), anti-PD-1 alone ($n = 5$) or vehicle ($n = 6$) since day 10 post implantation. **m,n**, Relative abundance of LT-HSC, myeloid progenitors and myeloid populations in BM of KP tumour-bearing mice treated as indicated (**m**) and myeloid populations in blood of KP tumour-bearing mice treated as indicated (**n**), normalized to vehicle ($n = 5$ each). **o**, Frequency of intratumoral mo-macs, relative frequency of TREM2^{hi} mo-macs, CD86⁺MHCII⁺ mo-macs and TREM2^{hi} mo-macs expressing PD-L1 in lungs of KP tumour-bearing mice treated as indicated ($n = 5$ each). Individual data points with bar denoting mean, representative of two independent experiments (**a,d,g–l,o**) or one experiment (**b,c,m,n**). Statistics computed by unpaired two-tailed Student's *t*-test (**a,c,d,g–k**), two-way ANOVA with Fisher's LSD test (**b,m,n**), one-way ANOVA with Dunnett's multiple comparison (**l,o**). Scale bar, 2 mm (**a,g,l**).

monocytic lineages (Extended Data Fig. 8j–l). The GMP, cMoP and mature monocyte clusters in BM of *Nfe2l2*^{ΔMs4a3} mice had reduced TF motif accessibility for *Nfe2l2* and *Bach1*, *Stat3*, *Myc*, *Myb*, *Fosl2* and *Atf3*

that drive important facets of myeloid differentiation, proliferation and survival^{47–49} (Fig. 4e and Extended Data Fig. 8m). Type I or III IFN response regulators such as *Irf3*, *Irf5* and *Irf9* were enriched in DARs of

Article

Nfe2l2^{ΔMs4a3} mature Ly6C^{hi} monocytes, matched by reduced accessibility for *Hnf1a*, *Etv3* and *Etv6* (ref. 50) (Extended Data Fig. 8m). Downstream of BM progenitors, molecular programs in lung-infiltrating myeloid cells were significantly altered in *Nfe2l2^{ΔMs4a3}* mice (Extended Data Fig. 8n,o). NRF2 activation scores were decreased in Ly6C^{hi} monocytes from *Nfe2l2^{ΔMs4a3}* mice, with a concomitant upshift in IFN-responsive gene scores (Extended Data Fig. 8p). Specifically, there was relative enrichment of ISGs (*Stat1*, *Rasd2*, *Ifit2*, *Isg20*, *Ifit3b*) and antigen presentation genes (*H2-Ab1*, *H2-Aa*, *Mef2c*) in *Nfe2l2^{ΔMs4a3}* TME-infiltrating monocytes and mo-macs, with a decrease in sensing pathways (*Ier3*, *Tlr4*, *Cd38* and *C3ar1*), immunoregulatory genes (*Chil3*, *Vcan*, *S100a8*, *Ngp*, *Lcn2*, *Arg1*, *Ptg51* and *Prtn3*) and NRF2-associated cytoprotective genes (*Gpx3*, *Gclm*, *Tfec* and *Ednrb*) (Fig. 4f and Extended Data Fig. 8q).

To disentangle how NRF2 affects local reprogramming in the TME from how it influences replenishment through myelopoiesis, we leveraged the tamoxifen-inducible strategy to generate *Nfe2l2^{ΔMs4a3CreERT2}* mice and conditionally ablate NRF2 signalling in myeloid precursors before or after tumour exposure. Tamoxifen administration from the time of KP tumour implantation (early) in *Nfe2l2^{ΔMs4a3CreERT2}* mice resulted in a greater reduction in tumour when compared with tamoxifen administration at later stages of progression (Fig. 4g). Early attenuation of NRF2 signalling in *Nfe2l2^{ΔMs4a3CreERT2}* mice was associated with a decrease in BM GMPs, cMoPs and CD157⁺Ly6C^{hi} monocytes (Fig. 4h), reduced mobilization of CD157⁺Ly6C^{hi} monocytes (Fig. 4i), but insignificant changes to neutrophil mobilization and tumoural infiltration (Extended Data Fig. 9a,b). Early attenuation of NRF2 signalling, as evidenced by reduced nuclear NRF2 in TME mo-macs, was associated with accumulation of more immunostimulatory mo-macs (Fig. 4j,k). Reduced myeloid NRF2 signalling was associated with significant infiltration of tumoricidal IFNγ⁺ natural killer cells into lung tumours (Extended Data Fig. 9c–e). Effector CD8⁺ T cells were also more abundant in the tumours of *Nfe2l2^{ΔMs4a3}* mice (Extended Data Fig. 9f,g). Depletion of monocytes and mo-macs in KP tumour-bearing NRF2-proficient mice resulted in a clear reduction in tumour burden, signifying the importance of mo-macs in KP progression, but such treatment in *Nfe2l2^{ΔMs4a3}* mice saw no additive impact, suggesting NRF2 activation in mo-macs is crucial to orchestrating immunosuppression (Extended Data Fig. 9h). Furthermore, depletion of natural killer cells in tumour-bearing *Nfe2l2^{ΔMs4a3}* mice resulted in greater tumour burden, highlighting the mode of immunoregulation in this model to be predominantly by means of natural killer cell exclusion and suppression³⁴ (Extended Data Fig. 9i).

Targeting myeloid NRF2 potentiates immunotherapy

Given the impact of NRF2 activation on mo-macs curtailing anti-tumour natural killer cell and T cell surveillance, we interrogated whether myeloid NRF2 influences immunotherapy response. In three independent scRNA-seq datasets of immunotherapy or chemotherapy response comparing baseline with post-therapy tissue, tumour-infiltrating mo-macs enriched in non-responders (Extended Data Fig. 10a–c and Methods), as well as circulating CD14⁺ monocytes in non-responders with stable disease (Extended Data Fig. 10d) had DEGs regulated by TFs such as *PPARG*, *TP63*, *SMAD4* and *NFE2L2*. Spurred on by our observations, we tested whether pharmacological inhibition of NRF2 can enhance response to checkpoint blockade. We administered NRF2 inhibitor Brusatol with or without anti-PD-1 therapy starting at day 9 post-KP tumour implant. Combination treatment significantly reduced tumour burden (Fig. 4l), affected myelopoiesis as evidenced by the reduction of CMPs, GMPs and cMoPs (Fig. 4m), and reduced mobilization of CD157⁺Ly6C^{hi} monocytes (Fig. 4n). These systemic changes were associated with a decrease in the abundance of mo-macs, specific decrease in PD-L1⁺TREM2^{hi} mo-macs and concomitant increase in CD86⁺MHCII⁺ mo-macs (Fig. 4o). Combination of Brusatol and anti-PD-1 prolonged survival outcomes beyond benefit derived from anti-PD-1 monotherapy (Extended Data Fig. 10e). A similar dosing

regimen using ML385 in conjunction with anti-PD-1 had similarly improved outcomes (Extended Data Fig. 10f). We found the efficacy of combination therapy relied on targeting of myeloid NRF2, because administration of Brusatol and anti-PD-1 in *Nfe2l2^{ΔMs4a3Cre}* mice had no additive impact on anti-tumour immunity (Extended Data Fig. 10g). Anti-tumour immunity was associated with a substantial influx of natural killer cells with increased expression of CD69 and tumoricidal IFNγ (Extended Data Fig. 10h), alongside effector CD8⁺ T cells lacking exhaustion marks, and producing IFNγ and tumour necrosis factor (Extended Data Fig. 10i).

Discussion

We demonstrate that peripheral tumour cues induce maladaptive myelopoiesis, in part, by altering the oxidative stress response in BM progenitors through NRF2 priming. These findings are indicative of hormetic oxidative stress during steady-state haematopoiesis becoming dysfunctional during chronic inflammation and malignancy⁵¹. We further find NRF2-driven programs to be progressively activated in tumour-infiltrating mo-macs, promoting pro-survival, detoxification and immunosuppressive machinery. Our work aligns with evidence of neutrophil reprogramming in the TME^{52–54}, and posits a shared oxidative stress-mediated cytoprotective mechanism across myeloid cells engendering immunosuppression. Our data extend this model, demonstrating that maladaptation of NRF2 signalling is initiated early in tumour-educated BM myeloid progenitors as a ‘first hit’ and reinforced along the mo-mac lineage in the TME. These findings also imply the establishment of epigenetic memory in HSCs and myeloid progenitors⁵⁵ wrought by tumour inflammation.

Our data highlight the potential of targeting oxidative stress regulators such as NRF2 in influencing monocyte fate and restoring mo-mac immunogenicity. Targeting NRF2 signalling in myeloid progenitors and TME myeloid cells can have the added benefit of exploiting NRF2-KEAP1 vulnerability in many cancers⁵⁶. Therapeutics exploiting modalities such as TF-targeted molecular glue degraders and PROTACs⁵⁷ could provide specific and durable rewiring of monocytic differentiation in the TME. NRF2 is part of a constellation of stress response regulators governing metabolism and proteostasis^{58–60}; future studies will help decipher how these factors interplay with NRF2 in priming cytoprotective and immunoregulatory gene loci in myeloid progenitors to orchestrate TME mo-mac fate.

Online content

Any methods, additional references, Nature Portfolio reporting summaries, source data, extended data, supplementary information, acknowledgements, peer review information; details of author contributions and competing interests; and statements of data and code availability are available at <https://doi.org/10.1038/s41586-025-09493-y>.

1. DeNardo, D. G. & Ruffell, B. Macrophages as regulators of tumour immunity and immunotherapy. *Nat. Rev. Immunol.* **19**, 369–382 (2019).
2. Swann, J. W., Olson, O. C. & Passegae, E. Made to order: emergency myelopoiesis and demand-adapted innate immune cell production. *Nat. Rev. Immunol.* **24**, 596–613 (2024).
3. Goswami, S., Anandhan, S., Raychaudhuri, D. & Sharma, P. Myeloid cell-targeted therapies for solid tumours. *Nat. Rev. Immunol.* **23**, 106–120 (2023).
4. Sica, A., Guarneri, V. & Gennari, A. Myelopoiesis, metabolism and therapy: a crucial crossroads in cancer progression. *Cell Stress* **3**, 284–294 (2019).
5. Giles, A. J. et al. Activation of hematopoietic stem/progenitor cells promotes immunosuppression within the pre-metastatic niche. *Cancer Res.* **76**, 1335–1347 (2016).
6. Casbon, A. J. et al. Invasive breast cancer reprograms early myeloid differentiation in the bone marrow to generate immunosuppressive neutrophils. *Proc. Natl. Acad. Sci. USA* **112**, E566–E575 (2015).
7. Wu, W. C. et al. Circulating hematopoietic stem and progenitor cells are myeloid-biased in cancer patients. *Proc. Natl. Acad. Sci. USA* **111**, 4221–4226 (2014).
8. Porembka, M. R. et al. Pancreatic adenocarcinoma induces bone marrow mobilization of myeloid-derived suppressor cells which promote primary tumor growth. *Cancer Immunol. Immunother.* **61**, 1373–1385 (2012).
9. Trzebanski, S. et al. Classical monocyte ontogeny dictates their functions and fates as tissue macrophages. *Immunity* **57**, 1225–1243 (2024).

10. Ikeda, N. et al. The early neutrophil-committed progenitors aberrantly differentiate into immunoregulatory monocytes during emergency myelopoiesis. *Cell Rep.* **42**, 112165 (2023).
11. LaMarche, N. M. et al. An IL-4 signalling axis in bone marrow drives pro-tumorigenic myelopoiesis. *Nature* **625**, 166–174 (2024).
12. Hao, X. et al. Osteoprogenitor–GMP crosstalk underpins solid tumor-induced systemic immunosuppression and persists after tumor removal. *Cell Stem Cell* **30**, 648–664 (2023).
13. Gerber-Ferder, Y. et al. Breast cancer remotely imposes a myeloid bias on haematopoietic stem cells by reprogramming the bone marrow niche. *Nat. Cell Biol.* **25**, 1736–1745 (2023).
14. Dey, S., Curtis, D. J., Jane, S. M. & Brandt, S. J. The TAL1/SCL transcription factor regulates cell cycle progression and proliferation in differentiating murine bone marrow monocyte precursors. *Mol. Cell. Biol.* **30**, 2181–2192 (2010).
15. Pham, T. H. et al. Dynamic epigenetic enhancer signatures reveal key transcription factors associated with monocytic differentiation states. *Blood* **119**, e161–e171 (2012).
16. Mandala, J. K. & Rodriguez, P. C. Tumor-related stress regulates functional plasticity of MDSCs. *Cell Immunol.* **363**, 104312 (2021).
17. Paul, F. et al. Transcriptional heterogeneity and lineage commitment in myeloid progenitors. *Cell* **163**, 1663–1677 (2015).
18. Kwart, D. et al. Cancer-cell-derived type I interferons instruct tumor monocyte polarization. *Cell Rep.* **41**, 111769 (2022).
19. Alicea-Torres, K. et al. Immune suppressive activity of myeloid-derived suppressor cells in cancer requires inactivation of the type I interferon pathway. *Nat. Commun.* **12**, 1717 (2021).
20. Kwak, H. J. et al. Myeloid cell-derived reactive oxygen species externally regulate the proliferation of myeloid progenitors in emergency granulopoiesis. *Immunity* **42**, 159–171 (2015).
21. Pizzato, H. A. et al. Mitochondrial pyruvate metabolism and glutaminolysis toggle steady-state and emergency myelopoiesis. *J. Exp. Med.* **220**, e20221373 (2023).
22. Pietras, E. M. et al. Re-entry into quiescence protects hematopoietic stem cells from the killing effect of chronic exposure to type I interferons. *J. Exp. Med.* **211**, 245–262 (2014).
23. Molgora, M. et al. TREM2 modulation remodels the tumor myeloid landscape enhancing anti-PD-1 immunotherapy. *Cell* **182**, 886–900 (2020).
24. Katzenellenbogen, Y. et al. Coupled scRNA-seq and intracellular protein activity reveal an immunosuppressive role of TREM2 in cancer. *Cell* **182**, 872–885 (2020).
25. Matusiak, M. et al. Spatially segregated macrophage populations predict distinct outcomes in colon cancer. *Cancer Discov.* **14**, 1418–1439 (2024).
26. Mulder, K. et al. Cross-tissue single-cell landscape of human monocytes and macrophages in health and disease. *Immunity* **54**, 1883–1900 (2021).
27. McGinnis, C. S. et al. The temporal progression of lung immune remodeling during breast cancer metastasis. *Cancer Cell* **42**, 1018–1031 (2024).
28. Beury, D. W. et al. Myeloid-derived suppressor cell survival and function are regulated by the transcription factor Nrf2. *J. Immunol.* **196**, 3470–3478 (2016).
29. Namgaladze, D., Fuhrmann, D. C. & Brune, B. Interplay of Nrf2 and BACH1 in inducing ferroportin expression and enhancing resistance of human macrophages towards ferroptosis. *Cell Death Discov.* **8**, 327 (2022).
30. Kobayashi, E. H. et al. Nrf2 suppresses macrophage inflammatory response by blocking proinflammatory cytokine transcription. *Nat. Commun.* **7**, 11624 (2016).
31. Ryan, D. G. et al. Nrf2 activation reprograms macrophage intermediary metabolism and suppresses the type I interferon response. *iScience* **25**, 103827 (2022).
32. Olagnier, D. et al. Nrf2 negatively regulates STING indicating a link between antiviral sensing and metabolic reprogramming. *Nat. Commun.* **9**, 3506 (2018).
33. Ting, K. K. Y. et al. Oxidized low-density lipoprotein accumulation suppresses glycolysis and attenuates the macrophage inflammatory response by diverting transcription from the HIF-1alpha to the Nrf2 pathway. *J. Immunol.* **211**, 1561–1577 (2023).
34. Park, M. D. et al. TREM2 macrophages drive NK cell paucity and dysfunction in lung cancer. *Nat. Immunol.* **24**, 792–801 (2023).
35. Alaluf, E. et al. Heme oxygenase-1 orchestrates the immunosuppressive program of tumor-associated macrophages. *JCI Insight* **5**, e133929 (2020).
36. Leader, A. M. et al. Single-cell analysis of human non-small cell lung cancer lesions refines tumor classification and patient stratification. *Cancer Cell* **39**, 1594–1609 (2021).
37. Hu, J. et al. Tumor microenvironment remodeling after neoadjuvant immunotherapy in non-small cell lung cancer revealed by single-cell RNA sequencing. *Genome Med.* **15**, 14 (2023).
38. Zelenay, S. et al. Cyclooxygenase-dependent tumor growth through evasion of immunity. *Cell* **162**, 1257–1270 (2015).
39. Taniguchi, S. et al. In vivo induction of activin A-producing alveolar macrophages supports the progression of lung cell carcinoma. *Nat. Commun.* **14**, 143 (2023).
40. Gomez-Chou, S. B. et al. Lipocalin-2 promotes pancreatic ductal adenocarcinoma by regulating inflammation in the tumor microenvironment. *Cancer Res.* **77**, 2647–2660 (2017).
41. Li, Z. et al. Proinflammatory S100A8 induces PD-L1 expression in macrophages, mediating tumor immune escape. *J. Immunol.* **204**, 2589–2599 (2020).
42. Uccellini, M. B. & Garcia-Sastre, A. ISRE-reporter mouse reveals high basal and induced type I IFN responses in inflammatory monocytes. *Cell Rep.* **25**, 2784–2796 (2018).
43. Singh, A. et al. Small molecule inhibitor of NRF2 selectively intervenes therapeutic resistance in KEAP1-deficient NSCLC tumors. *ACS Chem. Biol.* **11**, 3214–3225 (2016).
44. Schaer, D. J. et al. Hemorrhage-activated NRF2 in tumor-associated macrophages drives cancer growth, invasion, and immunotherapy resistance. *J. Clin. Invest.* **134**, e174528 (2023).
45. Liu, Z. et al. Fate mapping via Ms4a3-expression history traces monocyte-derived cells. *Cell* **178**, 1509–1525 (2019).
46. Ren, D. et al. Brusatol enhances the efficacy of chemotherapy by inhibiting the Nrf2-mediated defense mechanism. *Proc. Natl Acad. Sci. USA* **108**, 1433–1438 (2011).
47. Perrone, M. et al. ATF3 reprograms the bone marrow niche in response to early breast cancer transformation. *Cancer Res.* **83**, 117–129 (2023).
48. Zhang, M. et al. Selective activation of STAT3 and STAT5 dictates the fate of myeloid progenitor cells. *Cell Death Discov.* **9**, 274 (2023).
49. Laurenti, E. et al. Hematopoietic stem cell function and survival depend on c-Myc and N-Myc activity. *Cell Stem Cell* **3**, 611–624 (2008).
50. Villar, J. et al. ETV3 and ETV6 enable monocyte differentiation into dendritic cells by repressing macrophage fate commitment. *Nat. Immunol.* **24**, 84–95 (2023).
51. Ratajczak, M. Z. & Kucia, M. Hematopoiesis and innate immunity: an inseparable couple for good and bad times, bound together by an hornetic relationship. *Leukemia* **36**, 23–32 (2022).
52. Ng, M. S. F. et al. Deterministic reprogramming of neutrophils within tumors. *Science* **383**, eadf6493 (2024).
53. Zhao, Y. et al. Neutrophils resist ferroptosis and promote breast cancer metastasis through aconitate decarboxylase 1. *Cell Metab.* **35**, 1688–1703 (2023).
54. Garner, H. et al. Understanding and reversing mammary tumor-driven reprogramming of myelopoiesis to reduce metastatic spread. *Cancer Cell* **43**, 1279–1295 (2025).
55. Damani, A. W. et al. Microbial cancer immunotherapy reprograms hematopoiesis to enhance myeloid-driven anti-tumor immunity. *Cancer Cell* <https://doi.org/10.1016/j.ccr.2025.05.002> (2025).
56. Singh, A. et al. Nrf2 activation promotes aggressive lung cancer and associates with poor clinical outcomes. *Clin. Cancer Res.* **27**, 877–888 (2021).
57. Chirnomas, D., Hornberger, K. R. & Crews, C. M. Protein degraders enter the clinic—a new approach to cancer therapy. *Nat. Rev. Clin. Oncol.* **20**, 265–278 (2023).
58. Mohamed, E. et al. The unfolded protein response mediator PERK governs myeloid cell-driven immunosuppression in tumors through inhibition of STING signaling. *Immunity* **52**, 668–682 (2020).
59. Raines, L. N. et al. PERK is a critical metabolic hub for immunosuppressive function in macrophages. *Nat. Immunol.* **23**, 431–445 (2022).
60. Kress, J. K. C. et al. The integrated stress response effector ATF4 is an obligatory metabolic activator of Nrf2. *Cell Rep.* **42**, 112724 (2023).

Publisher's note Springer Nature remains neutral with regard to jurisdictional claims in published maps and institutional affiliations.

Springer Nature or its licensor (e.g. a society or other partner) holds exclusive rights to this article under a publishing agreement with the author(s) or other rightsholder(s); author self-archiving of the accepted manuscript version of this article is solely governed by the terms of such publishing agreement and applicable law.

© The Author(s), under exclusive licence to Springer Nature Limited 2025

Article

Methods

Mice

C57BL/6 mice were obtained from Charles River Laboratories or Jackson Laboratory. CD45.1 congenic C57BL/6 mice were obtained from Jackson Laboratory (C57BL/6J-Ptprc^{em6Lutzy}/J RRID:IMSR_JAX:033076). *Ms4a3*^{Cre} mice were purchased from Jackson Laboratory (C57BL/6J-Ms4a3^{em2(Cre)Fgnx}/J RRID:IMSR_JAX:036382) and *Ms4a3*^{CreERT2} mice were received from F. Ginhoux⁴⁵. *Nfe2l2*^{f/f} floxed mice were purchased from Jackson Laboratory (C57BL/6-Nfe2l2^{tm1.1Sred}/SbsJ RRID:IMSR_JAX:025433). NRF2 constitutive knockout (*Nfe2l2*^{TKO}) mice were purchased from Jackson Laboratory (B6.129×1-Nfe2l2^{tm1Ywk}/J RRID:IMSR_JAX:017009). Keap1^{f/f} floxed mice were purchased from Jackson Laboratory (B6(Cg)-Keap1tm1.1Sbis/J RRID:IMSR_JAX:037075). *Mxi1*^{GFP} mice were received from A. Garcia-Sastre (Mount Sinai), and subsequently purchased from Jackson Laboratory (B6.Cg-Mxi1^{tm1.1Agsga}/J RRID:IMSR_JAX:033219). *Kras*^{LSL-G12D/+}; *Trp53*^{f/f} mice used for autochthonous model of NSCLC (GEMM) were purchased from Jackson Laboratory (B6.129-Kras^{tm4Tyj} Trp53^{tm1Bnn}/J RRID:IMSR_JAX:032435). Focal tumour were induced by means of intratracheal inhalation of $2.5 \times 10 \times 10^8$ pfu adenoviral vector with Surfactant Protein C promoter driving Cre recombinase (Ad5mSPC-Cre, courtesy of A. Berns) at 12 weeks of age. KP tumour implantations and associated experiments were conducted in mice between 10 and 14 weeks of age. Both male and female mice were used, and we observed no significant differences between sexes in any experiment. Where applicable, littermate controls were used to minimize variation between mouse strains. Mice were housed in individually ventilated cages at the Mount Sinai specific-pathogen-free facilities, provided food and water ad libitum, with conditions maintained at 21–23 °C, 39%–50% humidity and a 12:12 h dark–light cycle. All experiments were approved by, and in compliance with the Institutional Animal Care and Use Committee of the Icahn School of Medicine at Mount Sinai.

Human participants

Informed consent was obtained using the Universal Consent for Mount Sinai Biorepository (Human Subjects Electronic Research Applications 20-01197), in accordance with the protocol reviewed and approved by the Institutional Review Board (IRB) at the Icahn School of Medicine at Mount Sinai. Participants provided written consent to analysis of their blood and resected tissue. Samples of tumour and non-involved lung were then obtained from surgical specimens of participants undergoing resection at the Mount Sinai Hospital in collaboration with the Thoracic Surgery Department, the Mount Sinai Biorepository and Department of Pathology. Analysis of the tumour and non-involved lung samples was performed under IRB Human Subjects Electronic Research Applications 10-00472A, in accordance with the protocol reviewed and approved by the IRB at Icahn School of Medicine at Mount Sinai.

Murine tumour models

Unlabelled or GFP-transduced *Kras*^{LSL-G12D/+}; *Trp53*^{f/f} (KP) and non-fluorescent *Kras*^{LSL-G12D/+}; *Trp53*^{f/f}; *Rosa26*^{A3Bi}; *Rag1*^{-/-} (KPAR) cells derived from previously reported and validated mouse models of NSCLC^{61,62} were used for tumour implantation models. KP lines were maintained at 37 °C in RPMI supplemented with 10% v/v fetal bovine serum (FBS) and 1% v/v penicillin–streptomycin (Pen–Strep). KPAR lines were maintained at 37 °C in DMEM supplemented with 10% FBS and 1% Pen–Strep. LLC1 carcinoma cells were a gift from L. Ferrari de Andrade at Mount Sinai, originally purchased from ATCC (CRL-1642). B16-F10 melanoma cells were purchased from ATCC (CRL-6475). These non-KP cells were maintained at 37 °C in DMEM with 10% FBS and 1% Pen–Strep. Cells were injected in vivo when in log-phase of growth and within three or four passages of thawing. Depending on the experiment, 500,000 KP cells, 150,000 KPAR cells, 500,000 B16-F10 or 500,000 LLC1 cells were injected intravenously through the tail vein. For survival studies,

mice were killed when they exhibited more than 20% body weight loss or moribund status (laboured breathing, hunched posture, cachexia) according to predetermined humane end points. For profiling studies, mice were killed at the time points described in text. All experiments were approved and in compliance with the Institutional Animal Care and Use Committee of the Icahn School of Medicine at Mount Sinai.

Mixed-BM chimera

Lethally irradiated (2 × 6.5 Gy) 10–14-week-old CD45.1 mice were reconstituted with a 1:1 ratio of *Nfe2l2*^{WT} CD45.1 and *Nfe2l2*^{ΔMs4a3} CD45.2 BM cells ($5 \times 10 \times 10^6$ cells each) retro-orbitally. Mice were kept on sulfa-methoxazole–trimethoprim for 3 weeks. Mice were implanted with KP tumours 8–10 weeks after reconstitution, and chimerism was assessed 7 days before tumour implant (baseline), as well as 21 days post-implant (terminal).

In vivo treatments

To deplete natural killer cells specifically in vivo, tumour-bearing mice were administered 200 µg of anti-NK1.1-depleting antibody (Bio X Cell Clone PK136, catalogue no. BE0036) or 200 µg of immunoglobulin G2a (IgG2a) isotype (Bio X Cell, catalogue no. BE0085) at the indicated time point and continued every other day. For depletion of monocytic-macrophages in vivo, tumour-bearing mice were administered 400 µg of anti-CSF1R-depleting antibody (Bio X Cell Clone AFS98, catalogue no. BE0213) or 400 µg of IgG2a isotype (Bio X Cell, catalogue no. BE0089) at the indicated time point and continued every other day. To assess pharmacological inhibition of the NRF2 pathway in vivo, tumour-bearing mice were given Brusatol (MedChemExpress, catalogue no. HY-19543) orally, dissolved in 5% dimethylsulfoxide and 95% corn oil. In some experiments, tumour-bearing mice were administered ML385 (MedChemExpress, catalogue no. HY-100523) orally, dissolved at a concentration of 8 mg ml⁻¹ in 50% polyethylene glycol 30 + 50% saline. Mice were administered 100 µg of anti-PD-1 neutralizing antibody (Bio X Cell Clone RMP1-14, catalogue no. BE0146) or 100 µg of IgG2a isotype (Bio X Cell, catalogue no. BE0089) intravenously with 50 µg of Brusatol or 800 µg of ML385 every other day starting at day 10 after tumour implantation. Where indicated, mice were administered 500 mg kg⁻¹ NAC (Sigma-Aldrich, catalogue no. A9165) daily intraperitoneally in saline.

Tamoxifen-based in vivo pulse-chase and gene inactivation. KP tumours were implanted in tamoxifen-inducible reporter mice, and 2.5 mg of tamoxifen (Sigma-Aldrich, catalogue no. T5648) dissolved in corn oil was administered intraperitoneally on the indicated time points, or continually every day for NRF2 inactivation studies. Cre-activation was verified using TdTomato expression in circulating monocytes of *Nfe2l2*^{ΔMs4a3CreERT2} mice, as well as using flow cytometry for HO-1.

Mouse tissue processing

Mice were killed by CO₂ inhalation and death was confirmed by cervical dislocation. Mice were subjected to transcardiac perfusion with cold phosphate-buffered saline (PBS) and relevant tissue was extracted for downstream studies. Mouse lung lobes were digested on a shaker in RPMI media containing 10% FBS, collagenase IV (Sigma, catalogue no. C5138) and DNase I (Sigma, catalogue no. DN25) for 30 min at 37 °C before being triturated through an 18 G needle and filtered through a 70 µm mesh. Samples were subjected to RBC Lysis Buffer (BioLegend) for 2 min at room temperature and quenched with ice-cold fluorescence-activated cell sorting (FACS) buffer (PBS supplemented with 1% bovine serum albumin and 2 mM EDTA) before downstream processes. BM was flushed with cold FACS buffer using a 27 G needle from both long bones (femur and tibia) and filtered through a 70 µm mesh. Samples were subjected to RBC Lysis Buffer (BioLegend) for 2 min at room temperature and quenched with ice-cold FACS buffer before downstream processes. For assays such as low-input RNA and ATAC-seq,

marrow cells were enriched for Kit⁺ progenitors using the Mojosort Mouse Lin-neg enrichment kit (BioLegend, catalogue no. 480004). Blood was collected by cardiac puncture in EDTA-coated tubes and red blood cells (RBCs) were lysed in two successive cycles of 5 min each, at room temperature in RBC Lysis Buffer (BioLegend). Samples were quenched with FACS buffer and kept cold for downstream processes. Where relevant, serum was collected by coagulating blood in normal microcentrifuge tubes for 30 min at room temperature before centrifugation at 5,000g for 15 min at room temperature. Serum aliquots were made and stored at -80°C until experiment.

Histology

Tumour-bearing lungs were analysed at the indicated time points as follows: the left lung lobe was fixed in 4% paraformaldehyde at 4 °C, embedded in paraffin, and examined as 5-μm cross-sections. Following haematoxylin and eosin staining, lung tissue sections were scanned on slides at ×20 magnification using a Leica Aperio AT2 digital scanner and quantified by manual annotation of blinded slides using the Panoramic viewer and QuPath software v.0.4 (ref. 63).

Ex vivo culture models

BMDMs were generated ex vivo using established protocols³⁴. Briefly, BM was flushed using cold sterile PBS in sterile conditions (under laminar flow) and RBC-lysed for 1 min at room temperature. Cells were plated in DMEM containing 10% v/v FBS and 10 ng ml⁻¹ recombinant macrophage-colony stimulating factor (M-CSF; Peprotech, catalogue no. 315-02). Cells were plated at a concentration of ~150,000 cells per cm² on non-treated Petri plates. At day 2, media was replenished 1:1 with fresh media containing 10 ng ml⁻¹ M-CSF. At day 4, media was replaced with fresh media containing 10 ng ml⁻¹ M-CSF. At day 6, cells were gently replated onto test plates using ice-cold PBS containing 5 mM EDTA. KP CM was added at 1:1 ratio with existing media at the indicated time point. On the basis of the experimental time point, at day 7 or 8, BMDMs (verified 90%–95% of culture condition based on F4/80 and CD11b expression) were gently lifted off plates using ice-cold PBS containing 10 mM EDTA and subjected to downstream processes (flow cytometry, sequencing). KP CM was obtained from sub-confluent tumour cells grown in DMEM containing 10% v/v FBS, spun down at 10,000g to remove cellular debris and frozen in aliquots at -20 °C until use. Size-fractionation of CM was conducted using Amicon Ultra-15 centrifugal filter (Millipore) with a 3-kDa molecular weight cut-off. Protein-enriched supernatant and deproteinated flowthrough were resuspended to the same volume using base media and then frozen in aliquots at -20 °C until used. For experiments involving inhibitors of specific pathways, day 7 BMDMs were exposed to 10 μM ML385 (MedChemExpress, catalogue no. HY-100523) or 25 μM OB24 (MedChemExpress, catalogue no. HY-118487) at the indicated concentration and incubated for 18–24 h before wash off.

Short-term culture system

Mouse HSCs and progenitors were enriched from total BM using the EasySep CD117 positive selection kit (StemCell) according to manufacturer's instructions and plated at a concentration of ~100,000 cells per cm² on non-treated Petri plates in DMEM containing 10% FBS and 10 ng ml⁻¹ recombinant M-CSF (Peprotech). Cytokines (GM-CSF (Peprotech, catalogue no. 315-03), interleukin 6 (Peprotech, catalogue no. AF-216-16), G-CSF (Peprotech, catalogue no. AF-250-05), interleukin 3 (Peprotech, catalogue no. 213-13), stem cell factor (SCF) (Peprotech, catalogue no. 250-03) and Fms-like tyrosine kinase 3 ligand (Peprotech, catalogue no. 250-31L)), or neutralizing antibodies (anti-GM-CSF (Bio X Cell clone MP1-22E9) and anti-interleukin 6 (Bio X Cell clone MP5-20F3)), were added to media with or without 1:1 KP CM at the initial time point in the indicated concentrations. Where applicable, SB203580 (MedChemExpress, catalogue no. HY-10256) or ML385 was also added to media at indicated concentrations.

Methylcellulose and liquid culture assays

Total haematopoietic cells were extracted from the indicated mouse BM by flushing one femur with PBS, RBC-lysed and cells resuspended to a concentration of 300,000 cells per ml in IMDM (Cytivia) containing 1% Pen-Strep and 2% FBS. A volume of 0.4 ml of the resultant cells was added to pre-aliquoted 4 ml MethoCult tubes (StemCell, catalogue no. M3434 containing recombinant mouse SCF, recombinant mouse interleukin 3, recombinant mouse interleukin 6, recombinant human erythropoietin, recombinant human insulin and transferrin). The mixture was vortexed and dispensed onto 35-mm culture dishes in triplicate following the manufacturer's instructions. The dishes were incubated in a humidified incubator at 37 °C, 5% CO₂. Colonies were counted manually on day 8 on a gridded scoring dish and averaged across four independent plates. Liquid cultures from indicated mouse BM were generated as follows: 500 myeloid progenitors were sorted in triplicate into a 96-well non-tissue-culture-coated plate (Greiner) containing 150 μl of IMDM media with 5% FBS, 1% Pen-Strep, 50 μM β-mercaptoethanol + cytokines (25 ng ml⁻¹ each of recombinant mouse SCF, interleukin 11, Fms-like tyrosine kinase 3 ligand and recombinant human TPO, and 10 ng ml⁻¹ each of interleukin 3, GM-CSF and recombinant human erythropoietin). Fresh media (160 μl) was replenished every 2 days, and cells were counted using a Countess on days 4, 6 and 8 post sort.

Tissue processing (human)

Human NSCLC lung tissues were rinsed in cold PBS, minced and incubated on a shaker for 35 min at 37 °C in RPMI media containing collagenase IV at 0.25 mg ml⁻¹, Collagenase D at 200 U ml⁻¹ and DNase I at 0.1 mg ml⁻¹ (Sigma). Cell suspensions were then quenched in ice-cold FACS buffer, triturated through a 18 G needle and filtered through a 70 μm mesh before RBC lysis for 2 min at room temperature. Cell suspensions were enriched for CD45⁺ cells by either bead selection (bound fraction from StemCell EasySep Human CD45 Depletion Kit II) per kit instructions or FACS sorting on a BD FACSAria or Beckman CytoFlex SRT sorter before processing for scRNA-seq, scATAC-seq or Multiome.

Human NSCLC blood was processed as follows: PBMCs were isolated by Ficoll gradient and underwent RBC lysis for 5 min at room temperature. Cell suspensions were enriched for all myeloid cells or CD34⁺ myeloid cells by either bead selection (bound fraction from StemCell Technologies custom negative selection kit or CD34 positive selection II kit) or FACS sorting on a BD FACSAria or Beckman CytoFlex SRT sorter before processing for scRNA-seq, scATAC-seq or Multiome.

RT-qPCR

Messenger RNA was extracted from fresh cell pellets using TRIzol LS (Life Technologies), and retrotranscribed to complementary DNA using the RNA to cDNA EcoDry Premix Double-Primed kit (Takara). Transcripts were quantified using the AB7900-FAST-384 system (Applied Biosystems) with a two-step RT-qPCR process. Primer sequences (5' to 3') are provided in Supplementary Table 6. Housekeeping gene *Hprt* mRNA was included in each plate to provide normalization reference. Quantification of relative gene expression was calculated by the comparative Ct method ($2^{-\Delta\Delta Ct}$), relative to specified condition and normalized to values for *Hprt*.

Flow cytometry and FACS

Mouse tissue. Single-cell suspensions from mouse lung, blood and BM were resuspended at the desired cellular concentration in ice-cold FACS buffer and subjected to immunostaining in the following ways. Cells were first incubated with Fixable Blue Live/Dead Dye (Thermo Fisher Scientific) and CD16/CD32 (clone 93, BioLegend) for 15 min on ice before surface staining. Cells were stained for surface markers for 25 min on ice (antibody details are listed in Supplementary Table 5). Subsequently, cells were acquired fresh on a BD LSR Fortessa analyser.

Article

Alternatively, cells were fixed using the BD Cytofix kit (BD, catalogue no. 554655) following the manufacturer's instructions and acquired on a analyser within 3 days of fixation. For experiments assaying intracellular markers, cells were fixed using BD Cytofix/Cytoperm (BD, catalogue no. 554722) following the manufacturer's instructions and stained for intracellular antigens in Perm Buffer for 30 min at 4 °C. For phospho-flow cytometry of p38 MAPK, surface marker-stained cells were fixed at room temperature for 10 min in 4% paraformaldehyde and then further fixed in methanol at -80 °C for 1 h. Subsequently, cells were intracellularly stained in PBS containing 0.1% bovine serum albumin (BSA) and 0.5% Triton X-100 for 1 h at room temperature. For cytokine staining, cells were first stimulated in 10 µg ml⁻¹ Brefeldin A, 0.2 µg ml⁻¹ Ionomycin and 0.5 µg ml⁻¹ phorbol 12-myristate 13-acetate (Thermo Fisher Scientific) for 4 h at 37 °C before intracellular staining. For experiments assaying intranuclear transcription factors, cells were fixed and permeabilized using Ebioscience FOXP3 kit (Thermo Fisher Scientific, catalogue no. 00-5523-00) following the manufacturer's instructions and stained for intracellular antigens in Perm Buffer for 30 min at 4 °C (antibody details are listed in Supplementary Table 5). Subsequently, cells were acquired on a BD LSRFortessa analyser within 3 days of fixation. For sequencing purposes, cells were stained as above and sorted on a BD FACSAria sorter or Beckman CytoFlex SRT sorter using DAPI or 7-aminoactinomycin D to exclude dead cells. Cells were sorted into pre-chilled FBS-coated microcentrifuge tubes in 200 µl of PBS containing 0.5% BSA. To assay ROS and lipid peroxidation stress, cells were stained with CellROX (Invitrogen, catalogue no. C10444) and LiperFluo (Dojindo, catalogue no. L248) according to the manufacturer's instructions. To assess mitochondrial function and membrane polarity, cells were similarly incubated with MitoSOX (Invitrogen, catalogue no. M36006) and tetramethylrhodamine methyl ester (Invitrogen, catalogue no. T668) according to manufacturer's instructions and acquired live on BD LSR Fortessa analyser along with propidium iodide. For experiments analysing ferroptosis, cells were stained with annexin V for 15 min at room temperature in 1x binding buffer (Thermo Fisher Scientific), and fresh propidium iodide before acquisition live on the BD LSR Fortessa analyser. Representative gating strategies for broad sorting of myeloid lineage for sequencing experiments, and refined sorting for GMP transfer experiments are provided in Extended Data Fig. 2.

Human tissue. Cells were first incubated with Fixable Blue Live/Dead Dye (Thermo Fisher Scientific) and TruStain FcX (BioLegend) for 15 min on ice before surface staining. Cells were stained for surface markers for 25 min on ice (antibody details listed in Supplementary Table 5), followed by acquisition.

For sequencing studies, cells were sorted fresh on a BD FACSAria sorter or Beckman CytoFlex SRT sorter using DAPI or 7-aminoactinomycin D to exclude dead cells. Cells were sorted into pre-chilled FBS-coated microcentrifuge tubes in 200 µl of PBS containing 0.5% BSA. Representative gating strategies for sorting provided in Extended Data Fig. 2.

Cytokine array and Olink proteomics

For collecting BM sera, four long bones of each mouse were flushed with the same 200 µl of PBS-2% FBS using a 0.3 ml insulin syringe with a 28 G needle and spun at 3,000g for 5 min to remove BM cells. For collecting peripheral blood sera, collected blood from each mouse was allowed to coagulate at room temperature for 30 min, and then spun down at 3,000g for 5 min to remove cells and debris. Supernatants were further clarified by spinning down at 12,000g for 10 min, and samples were subsequently stored at -80 °C until use. BM sera samples were analysed using the semi-quantitative Proteome Profiler Mouse XL Cytokine Array (R&D Systems) and relative chemiluminescence signal was calculated at three different exposures. Subsequently, samples were assayed using the Olink Target 48 mouse cytokine panel (Olink Bioscience, Thermo Fisher Scientific), according to the manufacturer's

instructions. Real-time microfluidic quantitative PCR was performed in Biomark (Fluidigm) for the target protein quantification. Data were analysed using real-time PCR analysis software by means of the ΔΔCt method and Normalized Protein eXpression (NPX) manager. Data were normalized using internal controls in every single sample. NPX was generated on a log₂ scale proportional to the protein concentration. The protein concentration in standard concentration units (pg ml⁻¹) is obtained by fitting the NPX value to a standard curve, using four parameters in a nonlinear logistic regression model. The standard curves are defined for each biomarker. Differential protein abundance based on adjusted NPX values was calculated using package OlinkAnalyze v.4.1.2.

In vivo GMP transfer

The goal of short-term transfer experiments was to track fate of GMPs and study whether cell-intrinsic changes override microenvironmental influences upon infiltrating the TME. BM from indicated donor mice was flushed with cold FACS buffer using a 27 G needle from four long bones (femur and tibia) and filtered through a 70-µm mesh. Samples were subjected to RBC Lysis Buffer (BioLegend) for 2 min at room temperature and quenched with ice-cold FACS buffer before downstream processes. Marrow cells were enriched for Kit⁺ progenitors using the Mojosort Mouse Lin-neg enrichment kit (BioLegend, catalogue no. 480004). GMPs were sorted into pre-chilled FBS-coated microcentrifuge tubes in 200 µl of PBS containing 0.5% BSA on the Beckman CytoFlex SRT sorter. Cells were spun down and resuspended to concentration of 200,000 cells per millilitre in ice-cold PBS. Recipient CD45.1 mice received 100 µl of GMP retro-orbitally under anaesthesia at the indicated time points. Recipient mice were subsequently killed at day 21 and subjected to flow cytometric analysis.

Mouse CUT&RUN

A low cell input CUT&RUN technique was performed as follows: antibody-stained cell suspensions were lightly fixed in 200 µl of 0.1% formaldehyde (Sigma, catalogue no. 252549) at room temperature for 1 min and then quenched in 10 µl of 2.5 M glycine. Then 10,000 sorted cells in PBS were mixed with an equal volume of 2× Nuclear Extraction (NE) buffer: 40 mM HEPES, 20 mM KCl, 0.2% Triton X-100, 40% glycerol, 2 mM dithiothreitol, 1 mM Spermidine and 2× Roche Complete Protease Inhibitor (Millipore Sigma, catalogue no. 11873580001). Then 100× of KDACinhibitor cocktail (100 µM trichostatin A, 50 mM sodium butyrate and 50 mM nicotinamide in 70% dimethylsulfoxide) was added to the sorted sample for a final concentration of 1× before cryopreservation at -80 °C. CUT&RUN was performed in collaboration with EpiCypher following a modified CUT&RUN protocol. In brief, samples were thawed and diluted to 1 × 10⁵ cells ml⁻¹ in 1× NE buffer. A mixture of 10 µl of activated Concanavalin A beads, 2 µl of 1:50 SNAP-CUTANA K-MetStat Panel and 0.5 µg of primary antibody (rabbit IgG (EpiCypher catalogue no., 13-0042; lot 20335004-04), H3K4me1 (Thermo Fisher, catalogue no. 701763; lot 2135869), H3K4me3 (EpiCypher, catalogue no. 13-0041; lot 210760004-01), H3K27me3 (Thermo Fisher, catalogue no. MA5-11198; lot VL3152691) and H3K27ac (CST, catalogue no. 8173S; lot 8)) was added to 1 × 10⁴ cells per reaction and incubated overnight. Next day, beads were washed twice with 250 µl of digitonin buffer (20 mM, pH 7.5 HEPES, 150 mM NaCl, 0.5 mM Spermidine, 1× Roche Complete mini, 0.01% digitonin) before adding 5 µl of CUTANA pAG-MNase in 50 µl of digitonin buffer per reaction. Beads were washed twice and suspended in 50 µl of digitonin buffer. Then 2 mM CaCl₂ was then added to activate MNase and 33 µl of high-salt stop buffer (750 mM NaCl, 26.4 mM EDTA, 5.28 mM EGTA, 66 µg ml⁻¹ RNase A, 66 µg ml⁻¹ glycogen) was added to stop the MNase activity after 2 h incubation at 4 °C. Twenty picograms of CUTANA *Escherichia coli* spike-in DNA was added per sample, followed by a 10-min incubation at 37 °C to release the cleaved chromatin. CUT&RUN-enriched DNA was isolated by Concanavalin A beads, cleaned using Serapure beads, and libraries were prepared using a CUTANA CUT&RUN Library Prep Kit (EpiCypher,

catalogue no. 14-1001). Libraries were pooled and sequenced on an Illumina NovaSeq 6000 SP (150-cycle, paired end).

scRNA-seq assay

For each sample, a target recovery of 8,000 cells was loaded onto each lane of a 10x Chromium chip according to manufacturer's instructions. Libraries were prepared according to the manufacturer's instructions. All libraries were quantified by means of an Agilent 2100 hsDNA Bio-analyzer and KAPA library quantification kit (Roche, catalogue no. 0797014001). Libraries were sequenced at a targeted depth of 25,000 reads per cell using the NovaSeq 6000 S2 100 cycle kit (Illumina).

scATAC-seq and Multiome

For scATAC-seq preparation, cells were subjected to nuclei isolation following 10x Genomics manufacturer's protocol with minor adjustments. In case of low-input samples (with fewer than 100,000 cells), we used 0.2-ml PCR tubes and centrifuged at 4 °C using swinging rotor buckets to maximize nuclear recovery. For human NSCLC sample Multiome assays, cells were subjected to nuclei isolation following 10x Genomics manufacturer's protocol in the presence of RNase inhibitor (Sigma) and dithiothreitol (Sigma) to prevent RNA degradation. Viability of these nuclei was assessed using acridine orange–propidium iodide viability staining reagent (Nexcelom), and all samples post-nuclei isolation demonstrated viability at or below 1%. A target recovery number of 8,000 to 10,000 nuclei was loaded onto each lane of a 10x Chromium chip according to manufacturer's instructions. Barcoded DNA was extracted from the GEMs post-cleanup and amplified with 10x-specific sample indexing following the manufacturer's protocols. Libraries were quantified using TapeStation (Agilent) and were sequenced in pair-end mode using the NovaSeq 6000 S2 100 cycle kit (Illumina) targeting a depth of 25,000 reads per cell.

Mouse scRNA-seq analysis

Gene expression reads were aligned to the mm10 reference transcriptome and count matrices were generated using the default CellRanger 2.1 workflow, using 'raw' matrix output. Following alignment, barcodes matching cells that contained more than 500 unique molecular identifiers (UMIs) were extracted. From these cells, those with transcripts of more than 25% mitochondrial genes (quality control thresholds min_mc_size = 25, max_f_mit = 0.1) were filtered from downstream analyses. Matrix scaling, logarithmic normalization and batch correction by means of data alignment through canonical correlation analysis, and unsupervised clustering (resolution 0.7) using a K -nn graph partitioning approach were performed as previously described. Initial marker genes per cluster were identified using the FindMarkers function in Seurat v.4.4.0 (ref. 64) (non-parametric Wilcoxon rank sum test using presto and default parameters). Alternatively, we used the metacell package for clustering cells across the tumour, blood and BM samples separately (metacell size K = 25, outlier filter T_{lf} = 3). Subsequently clusters were annotated in a semi-supervised manner using canonical markers for lineage (for example, T cell, B cell, myeloid cell) and myeloid identity clusters were subjected to gene-module analyses as follows: cells were uniformly downsampled to 2,000 UMI to avoid counts-based bias before selecting the set of variable genes. Subsequently, the gene–gene correlation matrix was computed for each sample⁶⁵ subsetting for myeloid cells. Correlation matrices were averaged using Fisher Z-transformation. The inverse transformation resulted in the best-estimate correlation coefficients of gene–gene interactions across the dataset. Genes were clustered into modules using complete linkage hierarchical clustering over this correlation distance. Finally, myeloid clusters were annotated using lineage or function-determining gene modules. Where indicated, gene set enrichment analysis was performed (EnrichR) and redundancy-collapsed results were illustrated (REVIGO). Single-cell gene signature scoring was conducted using UCell v.2.4 (ref. 66); gene signatures are curated

from previously published studies^{9,67,68} and provided in Supplementary Table 1. Differentially expressed genes were calculated on pseudo-bulk counts data using muscat⁶⁹ (pbDD aggregateData) and defined as adjusted local $P < 0.05$ and absolute $\log_2[\text{fold change}] \geq 1$. Analyses were mostly run using mac x86 64-bit platform running R v.4.3.1 on macOS Big Sur 11.3.1 or mac x86 64-bit platform running R v.4.2.2 on Ubuntu 20.04.4 LTS.

Mouse scATAC-seq analysis

Fastq files from scATAC-seq samples were aligned to mouse genome reference mm10 using cellranger-atac v.2.0.0. Fragment files were parsed with ArchR v.1.0.2 and initial quality control was applied on the basis of sequencing depth and quality (minTSS = 8, minFrags = 5,000). Dimensionality reduction was applied on cells passing filters using standard ArchR workflow⁷⁰ (resolution 0.2, 0.4 and 0.8, varFeatures 15,000). Cells were clustered using Seurat's FindClusters function (resolution 0.8). Peaks were called using Macs2 (ref. 71) (adjusted P value < 0.05) to generate group coverages using addReproduciblePeakSet with default parameters. To select for myeloid clusters, we relied on ArchR Gene Scores or gene-activity scores (a surrogate for gene expression based on accessibility at the gene loci) of canonical markers and de novo marker discovery using getMarkerFeatures and getMarkers on the GeneScoreMatrix assay (FDR ≤ 0.01 and $\log_2[\text{fold change}] \geq 1.25$). Genomic regions were confirmed by visual inspection on Interactive Genomics Viewer (IGV). We filtered out lymphoid cell populations and CD45-negative contaminants, repeating ArchR analysis workflow on subsetted cells to increase the resolution of the monocytic and macrophage compartment (resolution 2.0). We used addGeneIntegrationMatrix with constraints to map between the paired scRNA and scATAC data. Correlation between gene scores in scATAC-seq clusters and relative gene expression in scRNA-seq clusters was used to define similarity scores and soft-label annotations to scATAC-seq clusters in a semi-supervised manner. TF deviations per cluster were inferred following ChromVAR⁷² using JAPSAR2020 motifs, CISBP and HOMER motifs. We calculated differentially accessible marker peak sets for identified monocytic–macrophage clusters and predicted which TFs mediate binding and define accessibility at these marker peaks using ArchR. Such analysis yields key lineage-determining TFs important for cell identity but can also prioritize TFs that are crucial to that cell's state and function. As part of candidate TF nomination, we computed TFs whose gene expression was positively correlated with changes in accessibility of their binding motifs (correlation greater than 0.4) and ranked by TF deviation (Δ) across clusters to nominate candidate regulators likely to be important to cellular function and identity. DARs were calculated using getMarkerFeatures on the Peak Matrix assay, with significance defined on the Wilcoxon rank sum test as adjusted local $P < 0.05$ and absolute $\log_2[\text{fold change}] \geq 0.4$. To identify differentially accessible TF motifs across conditions, we used getMarkerFeatures on the MotifMatrix assay correcting for TSS enrichment and number of fragments (FDR ≤ 0.05). Analyses were run using mac x86 64-bit platform running R v.4.3.1 on macOS Big Sur 11.3.1.

For paired analyses of RNA and ATAC features, previously processed and annotated mouse BM, blood and tumour scRNA-seq Seurat objects were normalized and scaled again using SCTtransform (glmGamPoi, vars.to.regress = "percent.mt", variable.features.n = 8,000). Mouse BM, blood and tumour scATAC-seq data were processed in parallel as follows. ATAC CellRanger fragment files were transformed into ArrowFiles with the ArchR package using the above methodology. Peaks were called using Macs2 with default parameters and addGroupCovariates, addReproduciblePeakSet and addPeakMatrix functions. Peaks co-accessibility matrix was obtained using the addCoAccessibility function. To pair each scRNA-seq cell with a scATAC-seq cell, datasets from both modalities were split by tissue before running FindTransferAnchors and TransferData using ATAC cells as the reference and RNA cells as the query. The combined Seurat object was filtered on myeloid

Article

cells (scRNA-seq metadata) and previously obtained peak matrix was also subsetted before being incorporated. TF deviations was inferred following ChromVAR using JAPSAR2020 and CISBP motifs.

Mouse CUT&RUN analysis

FASTQ data were adaptor trimmed using Trim Galore v.0.6.6 and aligned to mm10 reference genome using bowtie2 v.2.3.4.3 with parameters -X 700 -I 10. Uniquely mapped, non-duplicated reads with mapping quality more than 30 were filtered using SAMToolsview and Picard MarkDuplicates. BEDTools intersect was used to remove regions from ENCODE blacklist. Genome coverage tracks were generated using deep-tools2 with parameters bamCoverage --binSize 10 --normalizeUsing CPM --extendReads --ignoreDuplicates --smoothLength 50. Peaks were called using SEACR with parameters 'norm' and 'relaxed'. Paired binary alignment map files were generated for each sample after filtering for reads with a mapping quality score of more than 30 and a sequence length of less than 150. Bigwig files were derived from fragment files by normalizing read counts, and tracks were visualized using IGV v.2.17.4. We retrieved a list of myeloid genomic positions associated with open chromatin from the Immunological Genome Project murine ATAC-seq atlas⁷³ to prioritize active or poised states, and subsetted the regions to those retained in the published analysis. We extended the summits ± 500 base pairs to form a list of OCRs and trimmed the regions to within chromosomal boundaries using GenomicRanges v.1.52.0. These OCRs were then used to derive counts matrices, defined by the number of observed reads in each region, using chromVAR v.1.22 (ref. 72). Counts were then merged per histone mark, empty regions were filtered and GC bias was calculated per region. Using motifmatchr v.1.20.0, regions were annotated for the presence of TF motifs by referencing a custom database of mouse position frequency matrices. Subsequent chromVAR deviation z-scores indicate the bias-corrected and normalized presence of each histone modification around a particular TF motif, across all OCRs. To identify differentially variable regions with only two or three samples in each condition, we stratified data on the basis of the mean difference between two conditions, and the fraction of intrasample variance over total variance. The top genomic regions from chromVAR CUT&RUN analysis were confirmed by visual inspection on IGV and plotted using pyGenomeTracks v.3.9. To unbiasedly identify OCRs that were retained in both tumour-associated BM GMPs and Ly6C^{hi} monocytes, we applied k-means clustering to chromVAR-corrected OCR scores and used Genomic Regions Enrichment of Annotations Tool v.4.0.4 (ref. 74) (basal plus extension association rule) to annotate and summarize clusters of interest into Gene Ontology terms. To visualize the underlying distribution of histone modification signal without chromVAR correction, we used DeepTools v.3.5.5 to generate averaged profiles and heatmaps for each cluster of interest. In brief, bigwigs for each cell type and condition were averaged using bigwigAverage, browser extensible data files were outputted containing regions from each cluster, score matrices were calculated by computeMatrix and plots were generated through plotHeatmap. To orthogonally pinpoint tumour-specific changes in histone signal, scores were calculated for desired histone marks and cell types using the previously established DORC framework^{75,76}. DORC scores integrated paired bulk RNA-seq⁷⁷ and CUT&RUN signal (<https://rstats.immgen.org/cutrun/index.html>) in OCRs from sorted immune populations, identifying genomic regions which covary with gene expression.

Human public dataset scRNA-seq analysis

Raw count matrices were obtained from GEO repositories of published studies^{37,78,79}, also listed in Supplementary Table 7. After removal of doublets using the Solo method, data was processed in Scanpy⁸⁰, with genes detected in fewer than 10 cells and cells expressing fewer than 200 genes being filtered out. Further pre-processing involved filtering to remove cells where: (1) log1p_total_counts, log1p_n_genes_by_counts or the top 20 gene fraction exceeded five median absolute deviations;

and (2) mitochondrial_counts percentage surpassed three median absolute deviations or more than 20. The subsequent data was normalized, log1p-transformed and integrated using scVI⁸¹. The latent representation was used to compute the nearest neighbours distance matrix used for Leiden clustering at resolution 1. Cell types were manually annotated using established single-cell atlases. We analysed differential expression using Wilcoxon rank sum test, and corrected P values with the Benjamini–Hochberg method. Single-cell gene signature scoring was performed using sc.tl.score_genes function in Scanpy. Gene set enrichment analysis was conducted using Gseapy with the ENCODE_and_CheA_Consensus_TFs_from_ChIP-X gene set.

Human scATAC-seq and Multiome analysis

Fastq files from scATAC-seq and Multiome samples were aligned to human genome reference hg38 using cellranger-atac v.2.0.0 or cellranger-arc v.2.0.0 respectively. Fragment files were parsed with ArchR v.1.0.2 and initial quality control was applied on the basis of sequencing depth and quality, discarding cells with less than 3,000 fragments or a transcription start site enrichment score of less than 8. Dimensionality reduction and clustering was applied on cells passing filters using ArchR. To select for myeloid clusters, we relied on ArchR Gene Scores of canonical markers and de novo marker discovery using getMarkerFeatures on the GeneScoreMatrix assay. Thus, we filtered out lymphoid cell populations and CD45-negative contaminants for downstream RNA–ATAC integration. snRNA-seq from Multiome samples was analysed using Seurat v.4.4.0. Cells with fewer than 800 UMI or fewer than 400 genes detected were filtered out followed by default functions for data normalization and dimensionality reduction. To aid in the identification of macrophages cell states, we used hdWGCA v.0.2.18. This method allows for identification of gene co-expression modules after generation of metacells (groups of neighbouring cells in embedding space) to circumvent data sparsity. Metacells were generated with MetacellsByGroups function with following parameters: $k = 20$ max_shared = 15 and min_cells = 20. Gene modules were discovered using the function ConstructNetwork with the following parameters: soft-power = 3, deepSplit = 1, minModuleSize = 10, mergeCutHeight = 0.2, maxblocksize = 35,658. We also verified monocyte and macrophage assignment using orthogonal methodology of consensus non-negative matrix factorization ($k = 55$). For each cluster, we annotated using top genes ranked by spectra score in the gene expression program matrix obtained and selected the top 50 genes to generate cellular expression program signatures. In addition to soft assignments, this non-negative matrix factorization-based approach can work around the challenges of identifying and correcting batch effects emerged during data integration and requires minimal pre-processing steps. To annotate macrophage subtypes in chromatin space, we first co-embedded all scATAC samples and Multiome samples together, and removed batch effects using harmony v.0.1.1. We then annotated each cell cluster by the most abundant macrophage state in Multiome-origin cells that passed quality control and were previously annotated in snRNA-seq using marker gene expression. TF activity was calculated using ChromVAR v.1.16 implemented by ArchR by means of addMotifAnnotations, addBgdPeaks and addDeviationsMatrix functions. For visualization, ArchR built-in plotting functions and ComplexHeatmap v.2.10 were used. Subsequently, we carried out similar downstream gene activation score calculation using UCell, TF motif enrichment, TF prioritization and peak2gene linkage analyses as described above in the mouse section.

For the human haematopoietic stem and progenitor cell (HSPC)-enriched sample Multiome analysis, ATAC fragments were quality-controlled using PUMATAC v.0.0.1. Filtered cell barcodes were used to subset RNA counts data, and further processed by Scanpy v.1.9.5 (ref. 80) to retain cells with expressed genes of more than 100 and less than 4,500, mitochondrial counts percentage of less than 40, ribosomal counts percentage of less than 30 and haemoglobin counts percentage of less than 1. Scrublet and harmony embedded in Scanpy were used to

remove doublets and batch effects, respectively, with default settings. Leiden clustering was performed on harmony-corrected PCA embeddings (resolution of 2.0). Peripheral blood cell types were carefully annotated using existing single-cell PBMC and HSPC atlases. As previously, RNA gene signature scoring was calculated using UCell v.2.4. ATAC-seq data were further processed with pycisTopic v.2.0a0 (ref. 82) to export pseudobulk fragments files based on RNA cell-type annotations, call peaks (shift = 73, ext_size = 146, q_value = 0.05), generate a consensus peak set (peak_half_width = 250), run cisTopic using collapsed Gibbs sampling (n_topics = 40) and visualize topic contributions to identify topics enriched in PBMCs from patients with NSCLC. Pathway analyses was conducted on selected topics (regions) using Genomic Regions Enrichment of Annotations Tool as previously described.

Quantification and statistical analysis

No statistical methods were used a priori to determine sample size. Sample size was based on power analyses from prior studies in the laboratory and on establishing reproducibility between experiments. For flow cytometry, data were collected on FACSDiva v.8 or Beckman CytoExpert, and analysed using FlowJo v.10.9. Absolute cell numbers were calculated using initial loading volume and fluorescent beads (Accucheck Counting Beads PCB100, Molecular Probes) following the manufacturer's instructions. Where applicable, MFI measurements were compared for markers of interest. For histology, scanned haematoxylin and eosin slides were quantified by manual annotation of investigator-blinded slides using QuPath v.0.4 (ref. 63).

Statistical analyses for flow cytometry and histology were done using Prism v.10.0 (GraphPad). Statistical ranges in figures represent individual data points with bar at mean value, unless otherwise indicated in box plots or violin plots. For continuous data satisfying normality assumptions (flow cytometry, histology and sequencing), statistical significance between conditions was determined using unpaired Student's *t*-test for independent comparisons (Holm–Sidak) or one-way ANOVA for three or more independent groups, with multiple comparison correction (Dunnett's or Tukey's). Statistical significance between grouped data across three or more conditions was determined using two-way ANOVA with multiple comparison correction (Sidak's). Statistical significance for mouse survival analyses was performed using Kaplan–Meier log-rank estimate. UCell scores calculated on single-cell feature data are based on the Mann–Whitney *U* statistic and robust to dataset size and sample heterogeneity. DEG analyses in single-cell feature data were subjected to Wilcoxon rank sum test on pseudobulk values, as well as 'bimod' likelihood-ratio test optimal for single-cell feature expression⁸³ where indicated. Ontology terms in EnrichR were ranked by *P* value or odds ratio as indicated; where the enrichment *P* value was calculated using Fisher's exact test comparing the observed frequency with the frequency expected by chance in background gene list. Throughout the paper: **P* < 0.05, ***P* < 0.01, ****P* < 0.001 and 'NS' indicates not significant.

The following notable R packages were used: BiocManager v.1.30.22; biomaRt v.2.56.1; BSgenome v.1.68.0; BSgenome.Mmusculus.UCSC.mm10 sequences; BSgenome.Hsapiens.UCSC.hg38 sequences; Seurat v.4.4.0 and v.4.9.9; harmony v.0.1.1; scDissector v.1.0.0; parallel v.4.3.1; ShinyTree v.0.2.7; data.table v.1.14.8; reshape2 v.1.4.4; reticulate v.1.32.0; heatmaply v.1.3.0; pheatmap v.1.0.12; plotly v.4.10.0; ggvis v.0.4.7; ggplot2 v.3.3.5; cowplot v.1.1.1; patchwork v.1.1.3; dplyr v.1.3.1; tidyr v.1.3.0; tidyverse v.2.0.0; plyranges v.1.20.0; Matrix v.0.9.8; serialization v.1.3.5; ArchR v.1.0.2; chromVAR v.1.22.1; Signac v.1.11.9; complexHeatmap v.2.16.0; hdWGCNA v.0.2.18; edgeR v.3.42.4; limma v.3.56.2; presto v.1.0.0; EnhancedVolcano v.1.18.0; GenomeInfoDb v.1.36.1; GenomicRanges v.1.52.0; motifmatchr v.1.20.0; deepTools v.3.5.5; MAST v.1.6; Nebulosa v.1.10.0; RColorBrewer v.1.1; scCustomize v.1.1.3; sceasy v.0.0.7; scTools v.1.0; SeuratDisk v.0.0.0.9; SeuratWrappers v.0.3.19; SignatUR v.0.1.1; SingleCellExperiment v.1.22.0; TFBSTools v.1.38.0; UCell v.2.4.0; muscat v.1.20.0; OlinkAnalyze v.4.1.2.

Reporting summary

Further information on research design is available in the Nature Portfolio Reporting Summary linked to this article.

Data availability

Accession numbers for re-analysed published datasets are listed in Supplementary Table 7. Processed matrix files and metadata for the mouse tissue scRNA-seq and scATAC-seq generated in this study are made publicly available on GEO (GSE270148). Processed matrix files and metadata for human tissue scATAC-seq and 10x Multiome data generated in this study are also made publicly available at the time of publication on GEO (GSE270148). Source data are provided with this paper.

Code availability

Notable software package versions are listed in the Methods and in Supplementary Table 7. No new pipelines were used in the study beyond those described in the relevant Methods sections. Exemplar data objects and code for notable analyses in this study are provided at github.com/Merad-Lab/Hegde_Myelopoiesis_Epigenetics. Any additional information required to interpret data reported in this paper is available from the corresponding author upon request.

61. Boumelha, J. et al. An immunogenic model of KRAS-mutant lung cancer enables evaluation of targeted therapy and immunotherapy combinations. *Cancer Res.* **82**, 3435–3448 (2022).
62. Jackson, E. L. et al. The differential effects of mutant p53 alleles on advanced murine lung cancer. *Cancer Res.* **65**, 10280–10288 (2005).
63. Bankhead, P. et al. QuPath: open source software for digital pathology image analysis. *Sci. Rep.* **7**, 16878 (2017).
64. Hao, Y. et al. Integrated analysis of multimodal single-cell data. *Cell* **184**, 3573–3587 (2021).
65. Martin, J. C. et al. Single-cell analysis of Crohn's disease lesions identifies a pathogenic cellular module associated with resistance to anti-TNF therapy. *Cell* **178**, 1493–1508 (2019).
66. Andreatta, M. & Carmona, S. J. UCell: robust and scalable single-cell gene signature scoring. *Comput. Struct. Biotechnol. J.* **19**, 3796–3798 (2021).
67. Calzago, D. M. et al. The myeloid type I interferon response to myocardial infarction begins in bone marrow and is regulated by Nrf2-activated macrophages. *Sci. Immunol.* **5**, eaaz1974 (2020).
68. Agrawal, A. et al. WikiPathways 2024: next generation pathway database. *Nucleic Acids Res.* **52**, D679–D689 (2024).
69. Crowell, H. L. et al. muscat detects subpopulation-specific state transitions from multi-sample multi-condition single-cell transcriptomics data. *Nat. Commun.* **11**, 6077 (2020).
70. Granja, J. M. et al. ArchR is a scalable software package for integrative single-cell chromatin accessibility analysis. *Nat. Genet.* **53**, 403–411 (2021).
71. Zhang, Y. et al. Model-based analysis of ChIP-Seq (MACS). *Genome Biol.* **9**, R137 (2008).
72. Schep, A. N., Wu, B., Buenrostro, J. D. & Greenleaf, W. J. chromVAR: inferring transcription-factor-associated accessibility from single-cell epigenomic data. *Nat. Methods* **14**, 975–978 (2017).
73. Yoshida, H. et al. The *cis*-regulatory atlas of the mouse immune system. *Cell* **176**, 897–912 (2019).
74. McLean, C. Y. et al. GREAT improves functional interpretation of *cis*-regulatory regions. *Nat. Biotechnol.* **28**, 495–501 (2010).
75. Ma, S. et al. Chromatin potential identified by shared single-cell profiling of RNA and chromatin. *Cell* **183**, 1103–1116 (2020).
76. Kartha, V. K. et al. Functional inference of gene regulation using single-cell multi-omics. *Cell Genom.* **2**, 100166 (2022).
77. Lee, J. J. Early transcriptional effects of inflammatory cytokines reveal highly redundant cytokine networks. *J. Exp. Med.* **222**, e20241207 (2025).
78. Chen, Y. et al. Spatiotemporal single-cell analysis decodes cellular dynamics underlying different responses to immunotherapy in colorectal cancer. *Cancer Cell* **42**, 1268–1285 (2024).
79. Bassez, A. et al. A single-cell map of intratumoral changes during anti-PD1 treatment of patients with breast cancer. *Nat. Med.* **27**, 820–832 (2021).
80. Wolf, F. A., Angerer, P. & Theis, F. J. SCANPY: large-scale single-cell gene expression data analysis. *Genome Biol.* **19**, 15 (2018).
81. Gayoso, A. et al. A Python library for probabilistic analysis of single-cell omics data. *Nat. Biotechnol.* **40**, 163–166 (2022).
82. Bravo Gonzalez-Blas, C. et al. SCENIC+: single-cell multiomic inference of enhancers and gene regulatory networks. *Nat. Methods* **20**, 1355–1367 (2023).
83. McDavid, A. et al. Data exploration, quality control and testing in single-cell qPCR-based gene expression experiments. *Bioinformatics* **29**, 461–467 (2013).

Article

Acknowledgements M.M. was supported by National Institutes of Health (NIH) grants CA257195, CA254104 and CA154947. S.H. was supported by the National Cancer Institute (NCI) fellowship K00CA223043. B.Y.S. was supported by NIH Medical Scientist Training grant T32GM146636. R.M. was supported by the AACR-AstraZeneca Immuno-oncology fellowship 21-40-12-MATT. This work was supported by grant no. R24-072073 to the Immunological Genome Project (ImmGen) consortium. We thank the patients and their families for participating in the clinical study; members of the Merad laboratory and Brown laboratory at the Marc and Jennifer Lipschultz Precision Immunology Institute at Mount Sinai for insightful discussions and feedback; and E. Bernstein, D. Hasson and D. Filipescu for their technical advice and feedback. We acknowledge the Human Immune Monitoring Center, the Mount Sinai Biorepository and Pathology Core and the Mount Sinai Cytometry Core for extensive support and resources. This work was supported in part through the computational resources and staff expertise provided by the Bioinformatics for Next Generation Sequencing (BiNGS) Shared Resource Facility funded by NCI P30 Cancer Center and NIH/NIAMS P30 Skin Biology Disease Resource-based Center support grants. This work was also supported in part through the computational and data resources and staff expertise provided by Scientific Computing and Data at the Icahn School of Medicine at Mount Sinai and supported by the Clinical and Translational Science Awards (CTSA) grant UL1TR004419, and the Office of Research Infrastructure award S10OD026880 and S10OD030463. The content is solely the responsibility of the authors and does not necessarily represent the official views of the NIH.

Author contributions Conceptualization: S.H. and M.M. Methodology: S.H., B.G., S.M., J.D.B., A.M.T., B.D.B. and M.M. Acquisition and analysis of data: S.H., J.L.B., R.M., M.D.P., A. Marks, M.B., P.H., T.C., K.N., L.T., K.A. and G.C. Computational investigation of data: S.H., B.G., B.Y.S., L.H.,

M.M.S., B.K., M.D.P., A. Magen, D.D., K.F., J.J.L., D.A. and M.J.B. Writing—original draft: S.H. Writing—review and editing: S.H. and M.M. Resources: S.K.-S., R.M.F., A.J.K., F.G., J.D.B., S.Z.J., T.U.M., B.D.B. and M.M. Funding and supervision: M.M.

Competing interests M.M. serves on the scientific advisory board and holds stock from Compugen Inc., Dynavax Inc., Innate Pharma Inc., Morphic Therapeutics, Asher Bio Inc., Dren Bio Inc., Nirogy Inc., Genenta Inc., Oncoresponse, Inc. and Owkin Inc. M.M. also serves on the ad hoc scientific advisory board of DBV Technologies Inc. and Genentech Inc., and on the foundation advisory board of Breakthrough Cancer. M.M. receives funding for contracted research from Genentech, Regeneron and Boehringer Ingelheim. T.U.M. has served on advisory and/or data safety monitoring boards for Rockefeller University, Regeneron Pharmaceuticals, Abbvie, Bristol-Meyers Squibb, Boehringer Ingelheim, Atara, AstraZeneca, Genentech, Celldex, Chimeric, Glenmark, Simcere, Surface, G1 Therapeutics, NGMbio, DBV Technologies, Arcus and Astellas, and receives contracted grants from Regeneron, Bristol-Myers Squibb, Merck and Boehringer Ingelheim. The above interests are not directly relevant to this manuscript. The remaining authors declare no competing interests.

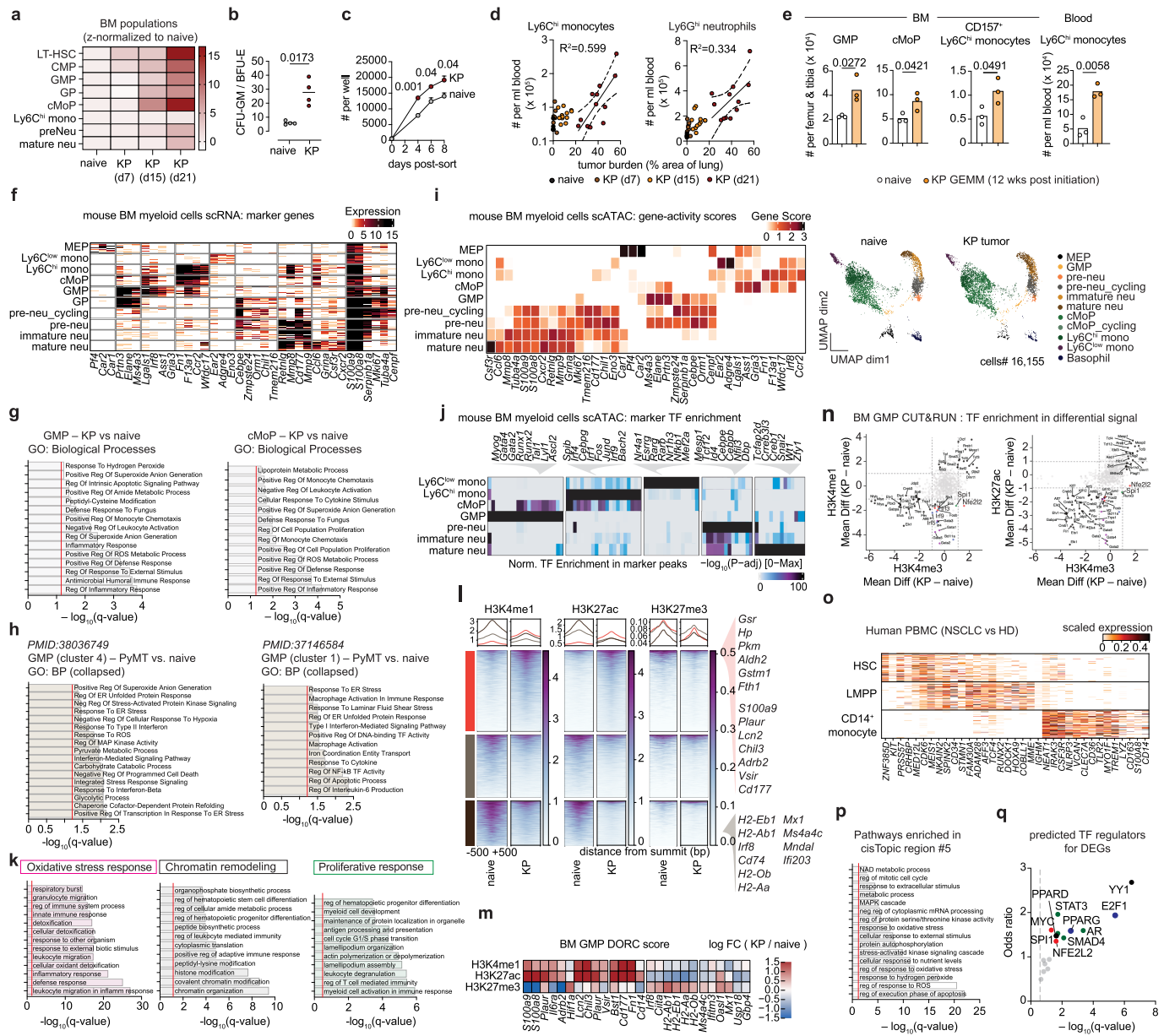
Additional information

Supplementary information The online version contains supplementary material available at <https://doi.org/10.1038/s41586-025-09493-y>.

Correspondence and requests for materials should be addressed to Miriam Merad.

Peer review information *Nature* thanks Tim Greten, Renato Ostuni and the other, anonymous, reviewer(s) for their contribution to the peer review of this work.

Reprints and permissions information is available at <http://www.nature.com/reprints>.

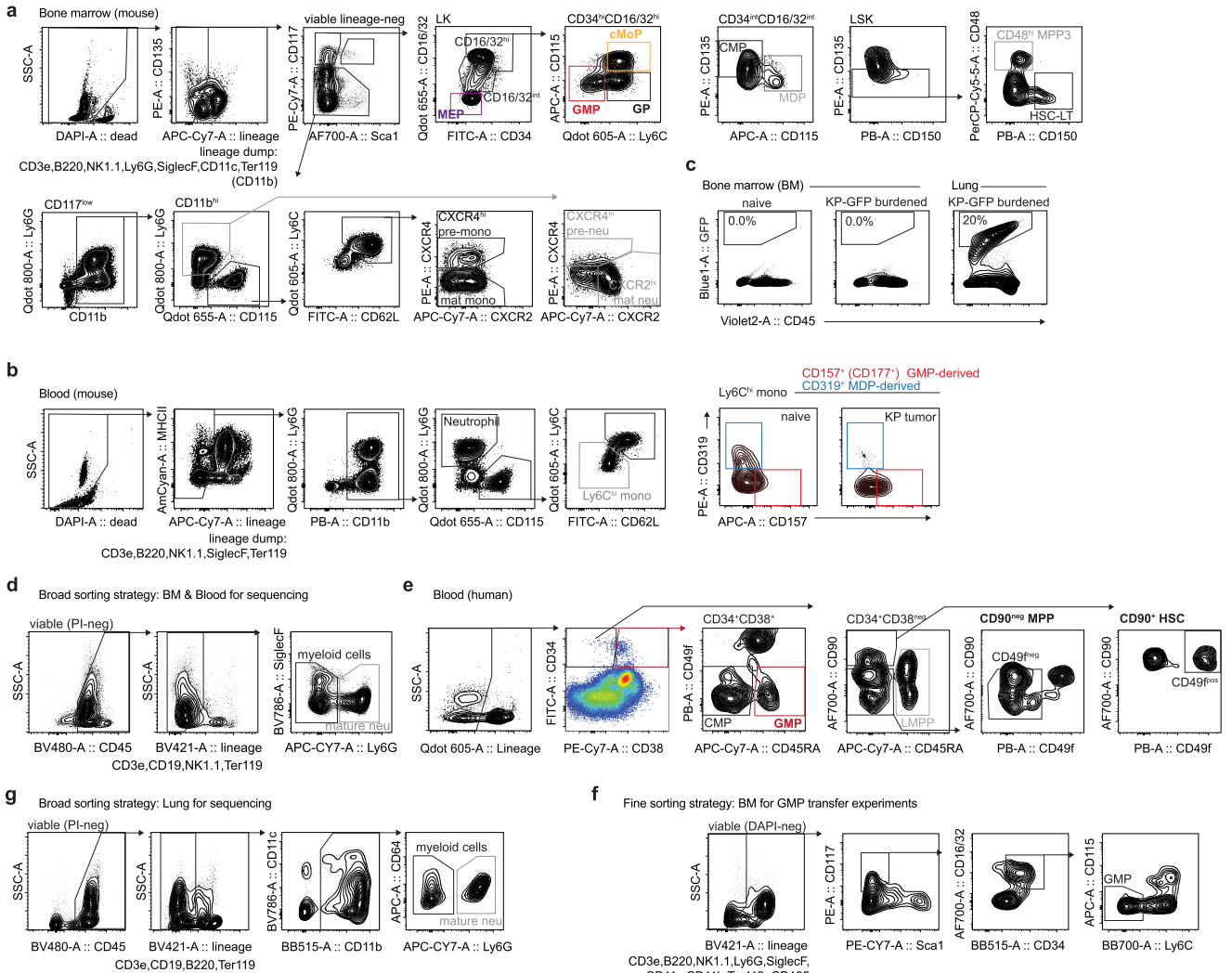


Extended Data Fig. 1 | See next page for caption.

Article

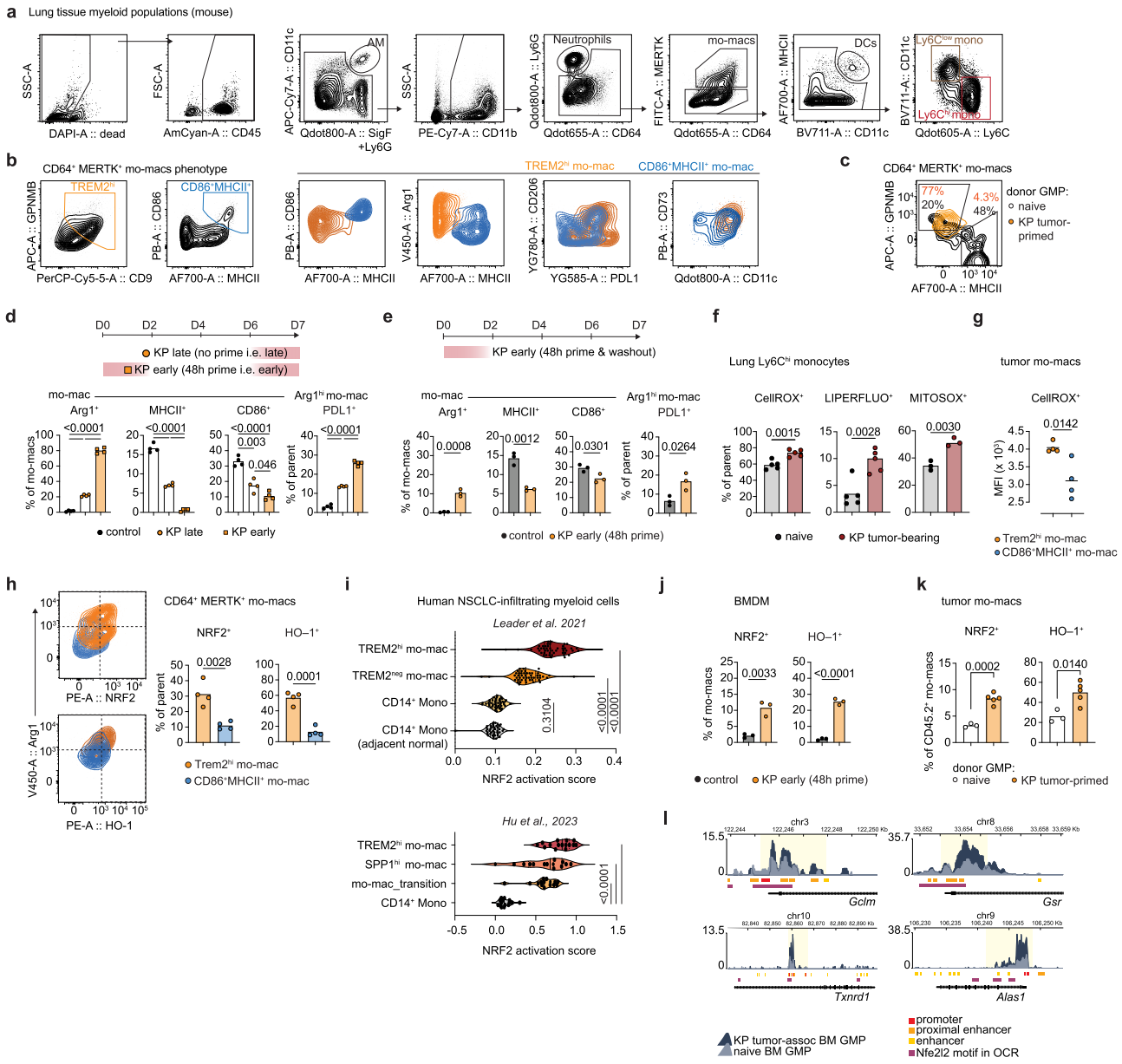
Extended Data Fig. 1 | Lung cancer promotes changes in the chromatin state of BM myeloid progenitors. **a**, Averaged heatmap for abundance of LT-HSCs, progenitors, and mature populations in bone marrow (BM) of KP tumor-bearing mice at different timepoints, normalized to tumor-naïve mice (left to right, n = 10,7,12,12). Pooled from two independent experiments. **b**, Granulocytic-monocytic colony forming units (CFU-GM) relative to erythroid blasts (BFU-E) after 8 days of incubation. n = 4 replicates. Pooled from two independent experiments. **c**, Longitudinal expansion of sorted GMPs from naïve and KP tumor-bearing mice. n = 3 replicates from one experiment. **d**, Number of Ly6C^{hi} monocytes and Ly6G^{hi} neutrophils in blood of naïve and KP tumor-bearing mice at different time points, correlated with tumor burden. Data are individual data points with confidence intervals for linear regression (left to right, n = 5,7,12,12). Pooled from two independent experiments. **e**, Number of GMPs, cMoPs, and CD157⁺Ly6C^{hi} monocytes in BM, and number of Ly6C^{hi} monocytes in blood of KP GEMM at 12 weeks post tumor initiation, compared to tumor-free mice. n = 3 mice per group, representative of two independent experiments. **f**, scRNA-seq heatmap of per-cell UMI counts across indicated myeloid cell subclusters in BM of tumor-bearing and naïve mice. Pooled over n = 3 mice per group. **g**, Gene ontology (GO) terms enriched in KP tumor-bearing mouse GMPs (left) and cMoPs (right) compared to naïve counterparts. Curated terms arranged by adjusted p-value (log q-value). **h**, Gene ontology (GO) terms enriched in PyMT tumor-bearing mouse GMPs compared to naïve counterparts from Gerber-Ferder et al.¹³ (left) and Hao et al. 2023 (right). Curated terms arranged by adjusted p-value (log q-value).

i, exemplar scATAC-seq UMAP and heatmap of column-normalized gene scores across indicated myeloid cell subclusters in BM of tumor-bearing and naïve mice. Pooled over n = 3 mice per group. **j**, scATAC-seq heatmap of normalized transcription factor (TF) motif accessibility enrichment in marker peak regions of indicated myeloid cell states. Pooled from n = 3 mice per group. **k**, GREAT pathway terms enriched in indicated H3K4me3 regions from BM GMPs and Ly6C^{hi} monocytes of KP tumor-bearing mice (Fig. 1f). Curated terms arranged by adjusted p-value (q-value). **l–m**, H3K4me1, H3K27ac, and H3K27me3 CUT&RUN signal clustering (**l**) and relative DORC scores for exemplar genes (**m**) in KP tumor-associated GMP relative to naïve GMP. **n**, Mean difference of ChromVAR-scores for TFs enriched in tumor-associated H3K4me3 signal versus H3K4me1 (left) and H3K27ac (right). **o**, scRNA-seq per-cell gene expression heatmap scaled across indicated myeloid subclusters in peripheral blood of human patients with NSCLC. Pooled from n = 4 patients. **p**, GREAT pathway terms enriched in indicated differentially accessible cisTopic region #5 of CD14⁺ monocytes from blood of patients with NSCLC (Fig. 1j). **q**, ChIP-X Enrichment Analysis (ChEA) calculated TF regulators for differentially expressed genes in CD14⁺ monocytes from blood of patients with NSCLC (n = 3) compared to healthy donors (n = 2). Dot color indicate major known biological pathways. Statistics computed by two-tailed Welch's t-test (**b**), unpaired t-test with Holm-Sidak multiple comparison (**c**), unpaired two-tailed Student's t-test (**e**), hypergeometric test with multiple test correction (**g,h,k,j,p,q**). error bars represent mean +/- SEM (**c**), colorscale indicates significance of motif enrichment based on hypergeometric test (**j**).



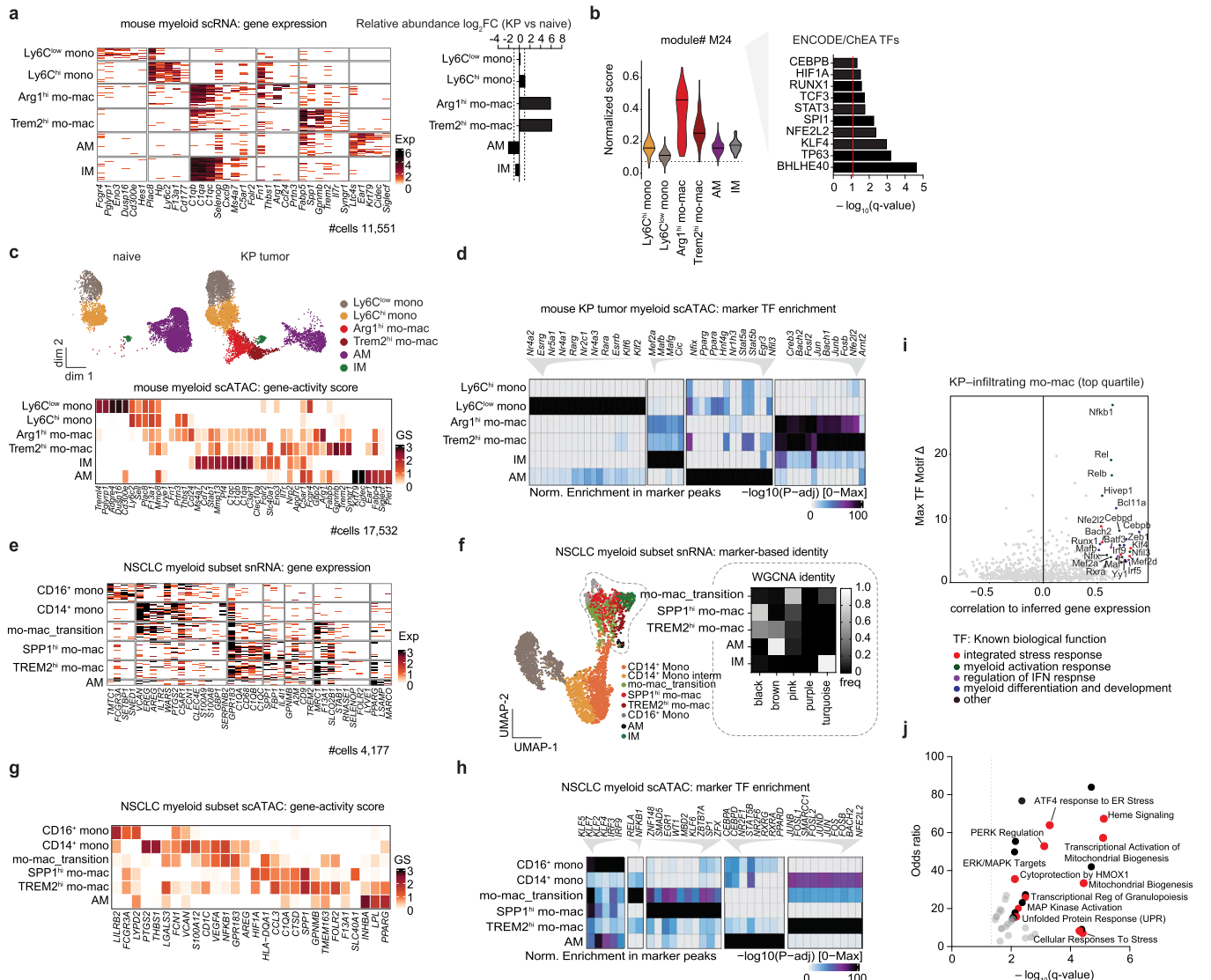
Extended Data Fig. 2 | Representative gating strategies for mouse and human experiments. **a**, Representative gating strategy for mouse bone marrow stem cell, progenitors, and differentiated monocyte and neutrophil populations. **b**, Gating strategy for mouse blood myeloid populations, and CD157⁺ phenotype of Ly6C^{hi} monocytes. **c**, Representative plots for GFP in tumor-naïve and GFP-expressing KP-burdened bone marrow (BM) and lung. **d**, Representative broad sorting strategy for myeloid populations in mouse BM and blood. **e**, Representative gating strategy for human blood stem cell.

Article

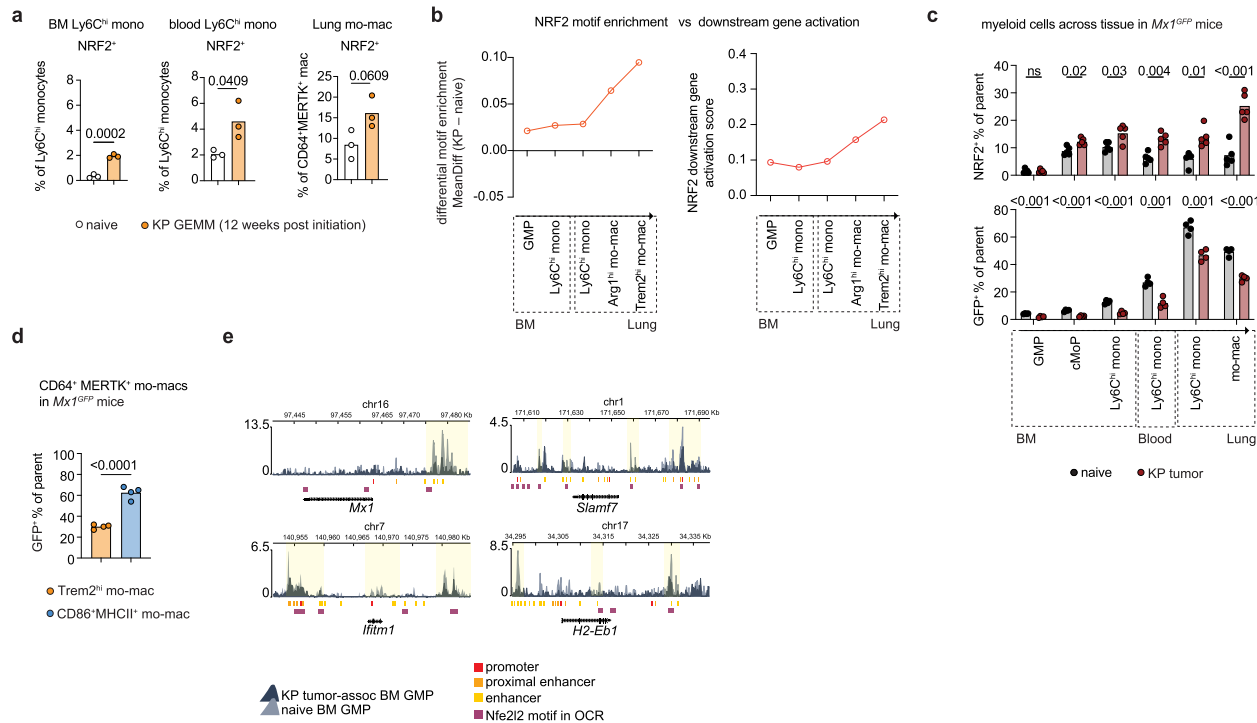


Extended Data Fig. 3 | Tumor-induced changes in BM progenitors impact mo-mac fate and function in TME. **a**, Representative gating strategy for mouse lung myeloid populations. AM, alveolar macrophages. DC, dendritic cells. mo-mac, monocyte-derived macrophages. **b**, Representative plots for intratumoral TREM2^{hi} mo-macs and CD86⁺MHCII^{hi} mo-macs, overlaid on phenotypic markers Arg1, CD206, PDL1, CD73, CD11c. **c**, CD64⁺MERTK⁺ mo-macs differentiated from donor CD45.2⁺ GMPs of naïve or tumor-primed origin (related to Fig. 2a). **d**, Frequency of BMDMs expressing Arg1, PDL1, MHCII, CD86 upon in vitro differentiation with KP tumor conditioning early (48 hr) or no conditioning (no prime). n = 4 per group. **e**, Frequency of BMDMs expressing Arg1, MHCII, CD86, and Arg1^{hi} mo-macs expressing PDL1 upon in vitro differentiation with KP tumor conditioning early (48 hr prime) followed by washout. n = 3 per group. **f**, Frequency of CellROX-, LiperFluo- (n = 5 per group), and MitoSOX-expressing Ly6C^{hi} monocytes (n = 3 per group) in KP tumor-bearing lung at day 21. **g**, Median Fluorescence Intensity (MFI) for CellROX in KP tumor-infiltrating mo-macs. n = 4 per group. **h**, Representative cytometry

plots and frequency of NRF2⁺ and HO-1⁺ cells in KP tumor-infiltrating mo-mac subsets. n = 4 per group. **i**, NRF2 downstream gene activation per-patient score in lung-infiltrating myeloid cells from independent cohorts of NSCLC (Leader et al., n = 35 and Hu et al. n = 15 patients). **j**, Frequency of BMDMs expressing NRF2 and HO-1 after 48 h prime and washout of KP CM, related to Extended Data Fig. 3e, n = 3 per group. **k**, Frequency of intratumoral donor mo-macs expressing NRF2 and HO-1 four days after GMP transfer from naïve (n = 3) or tumor-primed (n = 5) origin into congenic tumor-bearing hosts (related to Fig. 2a). One experiment. **l**, Browser plots for H3K4me3 signal at known NRF2-associated gene loci in KP tumor-associated and naïve GMPs. Highlighted regions indicate differential signal near known cis-regulatory elements and open chromatin (OCR) containing Nfe2l2 motif. Individual data points with bar denoting mean, representative of two independent experiments. Statistics computed by one-way ANOVA with Tukey's multiple comparison (**d**), one-way ANOVA with Dunnett's multiple comparison (**i**), and unpaired two-tailed Student's t-test (**e**–**h**), (**j**)–(**k**).

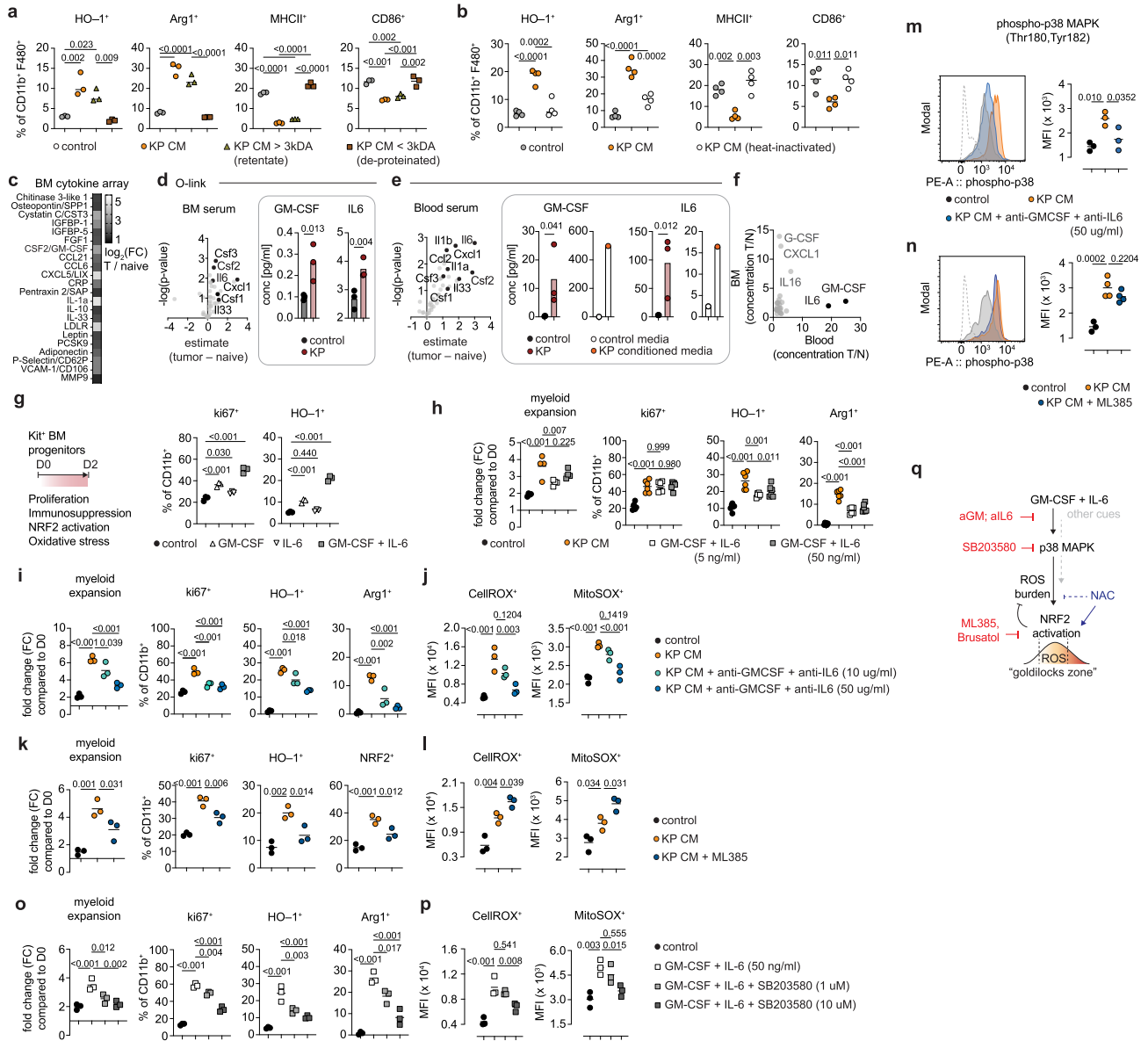


Extended Data Fig. 4 | Multiomic analyses of mouse and human lung cancer-infiltrating myeloid cells. **a**, scRNA-seq heatmap of per-cell UMI counts (left) and relative abundance (right) of myeloid sub-clusters in lung tissue of naïve and KP tumor-bearing mice. n = 3 pooled. **b**, Normalized UCell score for gene module# M24 across KP lung tumor-infiltrating myeloid cell clusters (left), with ENCODE/ChEA calculated TF regulators (right). **c**, exemplar scATAC-seq UMAP and heatmap of column-normalized genescores across indicated myeloid cell clusters in lung of naïve and tumor-bearing mice. n = 4 pooled. **d**, scATAC-seq heatmap of normalized transcription factor (TF) motif accessibility enrichment in marker peak regions of indicated myeloid cell states. n = 4 pooled. **e**, snRNA-seq heatmap of per-cell UMI counts for indicated myeloid clusters in human NSCLC primary lung tumors. n = 5 patients pooled. **f**, UMAP of myeloid cells in snRNA-seq data from human NSCLC primary lung



Extended Data Fig. 5 | NRF2 signaling in tumor-infiltrating monocytes lineage dampens Type I IFN responsiveness. **a**, Frequency of NRF2⁺ Ly6C^{hi} monocytes in BM (left), Ly6C^{hi} monocytes in BM (mid), and frequency of NRF2⁺ mo-macs in lung (right) of KP GEMM at 12 weeks post tumor initiation, compared to tumor-free mice, n = 3 per group. **b**, ChromVAR-computed TF motif deviation for *Nfe2l2* in tumor condition relative to naïve condition (left) and UCell-computed NRF2 downstream gene activation score (right) across indicated myeloid populations. **c**, Frequency of NRF2⁺ cells (top, n = 5 per group) and GFP⁺ cells (bottom, n = 4 per group) within indicated myeloid cell types from

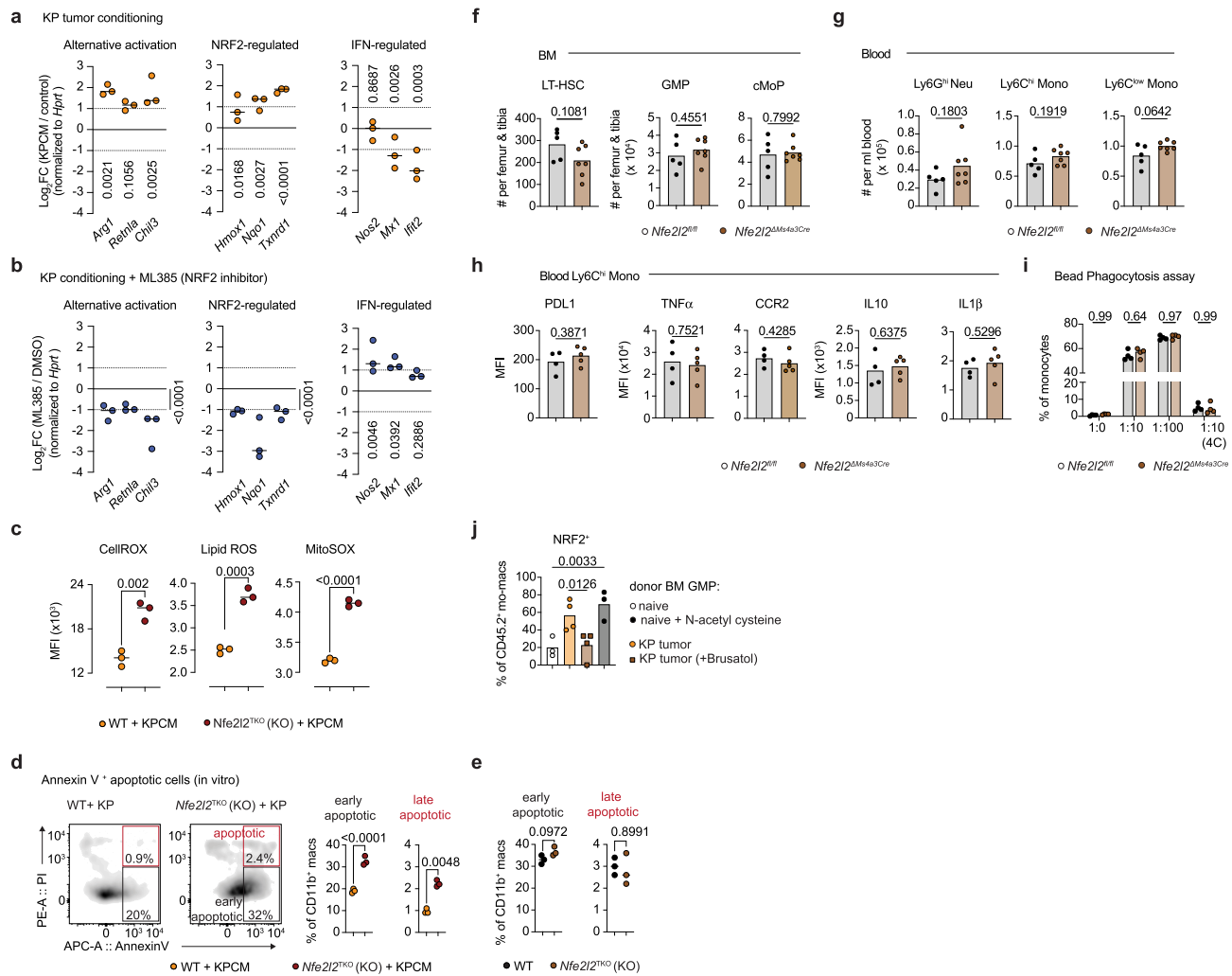
tumor-bearing and naïve (n = 4) *Mx1*^{GFP} mice. **d**, Frequency of GFP⁺ cells within CD64⁺MERTK⁺ mo-macs of indicated phenotype in tumor-bearing *Mx1*^{GFP} mice, n = 4 per group. **e**, Browser plots at indicated gene loci for H3K27ac signal in KP tumor-associated and naïve GMPS. Highlighted regions indicate differential signal near known cis-regulatory elements and open chromatin (OCR) containing *Nfe2l2* motif. Unless noted, data shown as individual data points with bar denoting mean, representative of two independent experiments (**a,c,d**). Statistics computed by unpaired two-tailed Student's t-test (**a,d**), and unpaired t-test with Holm-Sidak multiple comparison (**c**).



Extended Data Fig. 6 | Mitogenic tumor cues can elicit NRF2 activation in BM and TME to support myeloid expansion. **a**, Frequency of HO-1⁺, Arg1⁺, MHCII⁺, and CD86⁺ BMDMs after culture with >3 kDa KP CM protein retentate fraction, and <3 kDa KP CM deproteinated fraction. n = 3 per group. **b**, Frequency of HO-1⁺, Arg1⁺, MHCII⁺, and CD86⁺ BMDMs after culture with heat-inactivated KP CM. N = 4 per group. **c**, Protein abundance of indicated analytes in tumor-associated BM sera, represented as relative fold-change over naïve sera. n = 2 per condition, one experiment. **d–e**, Analytes upregulated in BM sera (**d**) and blood sera (**e**) of tumor-bearing mice compared to naïve mice as assessed by O-link, with relative concentrations of GM-CSF and IL-6 (box). n = 3 per group, one experiment. **f**, Comparison of analyte concentration from BM sera and blood sera, data from (**d**) and (**e**). **g**, Ex vivo progenitor expansion assay, with frequency of ki67⁺ and HO-1⁺ myeloid cells upon culturing BM Kit⁺ cells with indicated growth factors for 2 days. n = 3 per group. **h**, Relative expansion (left, n = 4) and frequency of ki67⁺, HO-1⁺, and Arg1⁺ myeloid cells (right, n = 6) upon culturing progenitors with KP CM or indicated growth factors for 2 days. **i–j**, Relative expansion of myeloid cells with frequency of ki67⁺, HO-1⁺, and Arg1⁺ myeloid cells (**i**) and median fluorescence intensity (MFI) for CellROX and

MitoSOX (**j**) after culturing progenitors with KP CM and indicated depletion antibodies for 2 days. n = 3 per group. **k–l**, Relative expansion of myeloid cells with frequency of ki67⁺, HO-1⁺, and NRF2⁺ myeloid cells (**k**) and MFI for CellROX and MitoSOX (**l**) after culturing progenitors with KP CM and ML385 for 2 days. n = 3 per group. **m–n**, Representative histogram and MFI quantification for phospho-p38 MAPK in myeloid progenitors treated with KP CM and indicated neutralizing antibodies (**m**, n = 3 per group) or KP CM and ML385 (**n**, n = 4 per group). **o–p**, Relative expansion of myeloid cells with frequency of ki67⁺, HO-1⁺, and Arg1⁺ myeloid cells (**o**) and MFI for CellROX and MitoSOX (**p**) after culturing BM progenitors with indicated growth factors in the presence of SB203580 for 2 days. n = 3 per group. **q**, Schematic for reactive oxygen species (ROS)-burden dependent poising of NRF2 pathways in growth factor-induced myeloid progenitor expansion in BM which enables NRF2 activation within TME. Individual data points with bar denoting mean, representative of two independent experiments (**a,g,h,i–p**). Statistics computed by one-way ANOVA with Tukey's multiple comparison (**a,b**), Dunnett's multiple comparison (**g–l**), hypergeometric test for O-link (**d,e**).

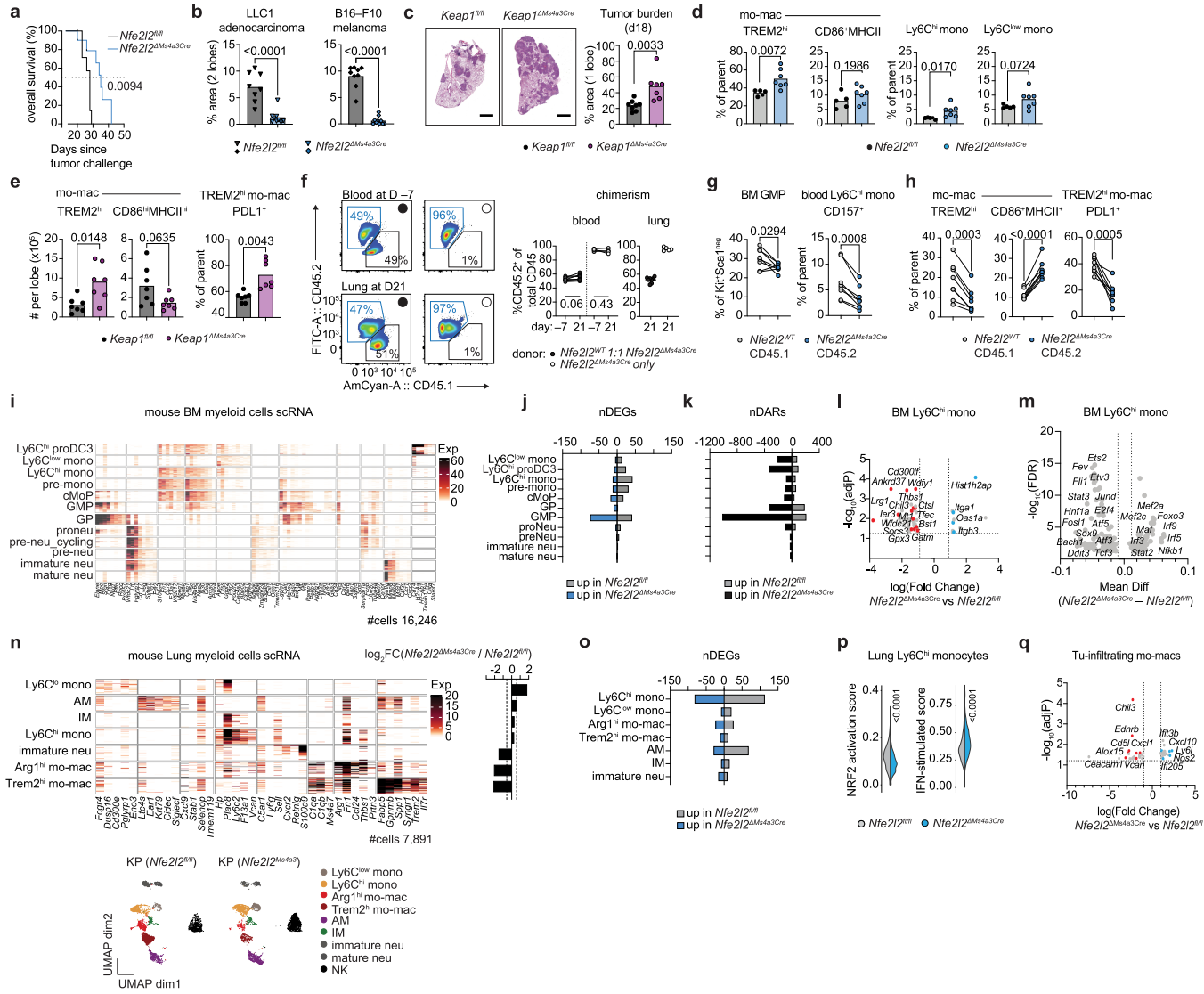
Article



Extended Data Fig. 7 | NRF2 signaling in tumor-infiltrating monocytic lineage promotes immunosuppressive program persistence in TME.

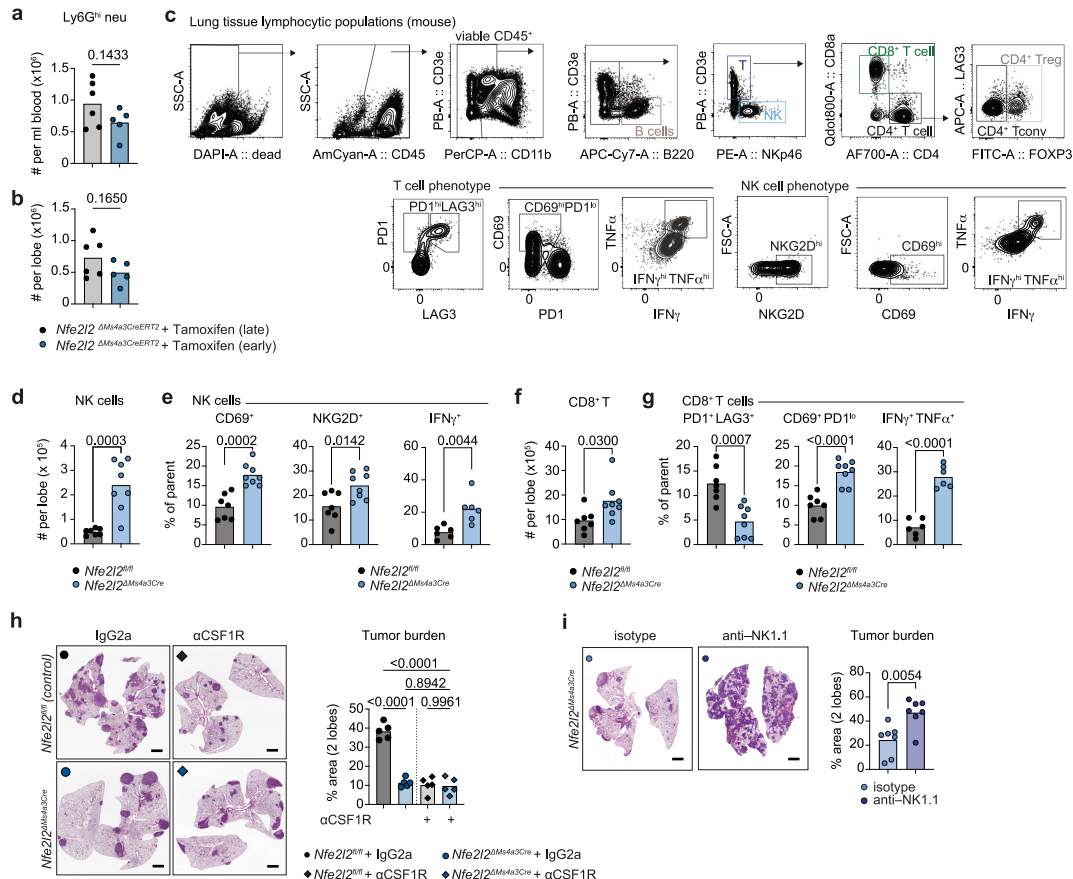
a, Gene expression in KP conditioned media (CM)-exposed BMDMs as measured by reverse transcription quantitative PCR (RT-qPCR). Relative values depicted as fold-change compared to control media, after normalization to *Hprt* expression. n = 3 replicates, representative of two independent experiments. **b**, Gene expression in KP CM-exposed BMDMs treated with ML385, as measured by RT-qPCR. Relative values depicted as fold-change compared to BMDMs treated with vehicle DMSO, after normalization to *Hprt* expression. n = 3 replicates, representative of two independent experiments. **c**, Relative MFI quantification of CellROX, LiperFluo, and MitoSOX in *Nfe2l2*^{TKO} (KO) or control (WT) BMDMs exposed to KP CM. n = 3 per group. **d**, Representative cytometry plots for Annexin-V and Propidium iodide (PI) in *Nfe2l2*^{TKO} (KO) or control (WT) BMDMs exposed to KP CM, with relative frequency of apoptotic cells. n = 3 per group. **e**, Relative frequency of apoptotic cells in *Nfe2l2*^{TKO} (KO)

or WT BMDMs without any tumor conditioning. n = 3 per group. **f–g**, Number of LT-HSCs and myeloid progenitors in BM (f) and myeloid cells in blood (g) of tumor-free *Nfe2l2*^{ΔM⁴a³C} mice (n = 7) or *Nfe2l2*^{fl/fl} controls (n = 5). **h**, MFI for indicated phenotypic markers in blood-circulating Ly6C^{hi} monocytes from tumor-free *Nfe2l2*^{ΔM⁴a³C} mice (n = 5) or *Nfe2l2*^{fl/fl} controls (n = 4). **i**, Fluorescent bead phagocytosis assay using tumor-free *Nfe2l2*^{ΔM⁴a³C} or *Nfe2l2*^{fl/fl} BM Ly6C^{hi} monocytes at different ratio of cells to beads. n = 4 per group. **j**, frequency of NRF2⁺ CD45.2⁺ donor-derived mo-macs derived from GMPs in Brusatol-treated tumor-bearing mice or N-acetyl cysteine-treated tumor-naïve mice transferred into KP tumor-bearing CD45.1 hosts, four days post transfer. (left to right, n = 3, 4, 4, 3). Individual data points with bar denoting mean, representative of two independent experiments (a,b,f–j) or three independent experiments (c,d,e). Statistics computed by unpaired two-tailed Student's t-test (c–h), two-way ANOVA with Fisher's LSD test (a,b) or Sidak's multiple comparison (i).



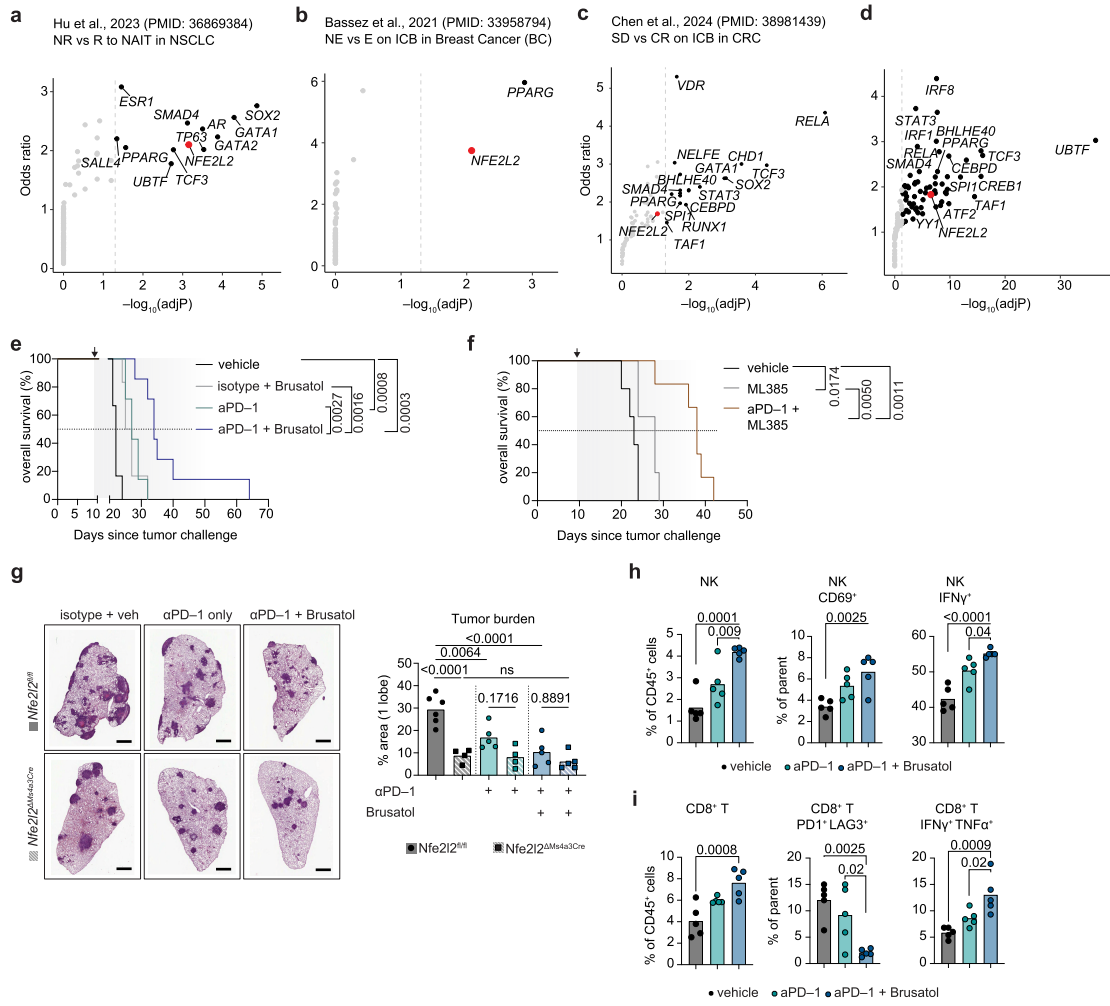
Extended Data Fig. 8 | Tumor-induced NRF2 signaling in BM impacts myelopoiesis and intratumoral myeloid phenotype. **a**, Kaplan-Meier plot for overall survival of KP tumor-bearing *Nfe2l2^{ΔMs4a3}* mice ($n=10$) or *Nfe2l2^{fl/fl}* littermates ($n=8$). **b**, Lung tumor burden in LLC1 tumor-bearing (left) and B16-F10 tumor-bearing (right) *Nfe2l2^{ΔMs4a3}* mice ($n=9,10$) or *Nfe2l2^{fl/fl}* littermates ($n=8,9$). **c**, Tumor burden in KP tumor-bearing *Keap1^{ΔMs4a3}* mice ($n=7$) or *Keap1^{fl/fl}* littermates ($n=8$). **d**, Frequency of Annexin-V⁺ cells within indicated intratumoral myeloid cells of KP tumor-bearing *Nfe2l2^{ΔMs4a3}* mice ($n=7$) or *Nfe2l2^{fl/fl}* littermates ($n=5$). **e**, Number of tumor-infiltrating TREM2^{hi} mo-macs, CD86⁺MHCII⁺ mo-macs, and TREM2^{hi} mo-macs expressing PDL1 in *Keap1^{ΔMs4a3}* mice or *Keap1^{fl/fl}* littermates ($n=7$ each). **f**, Representative flow plots (left) and quantification (right) of donor chimerism in blood and lung of *Nfe2l2^{WT/1:Nfe2l2^{ΔMs4a3Cre}}* chimera mice or *Nfe2l2^{ΔMs4a3Cre}* only chimera mice (left). Left to right, $n=8,4$ and $n=8,5$. Individual data points with lines connecting same mouse. **g-h**, Frequency of BM GMPs and blood CD157⁺ Ly6C^{hi} monocytes (**g**), frequency of lung-infiltrating TREM2^{hi} mo-macs, CD86⁺MHCII⁺ mo-macs, and lung-infiltrating TREM2^{hi} mo-macs expressing PDL1 (**h**) derived from indicated BM donors. Individual data points with lines connecting same mouse ($n=8$). **i**, scRNA-seq heatmap of per-cell UMI counts across indicated myeloid cell subclusters in BM of tumor-bearing *Nfe2l2^{ΔMs4a3}* and *Nfe2l2^{fl/fl}* mice. $n=3$ mice pooled per group. **j-k**, Number of differentially expressed genes i.e.,

nDEGs (**j**) ($|logFC| > 1$, $adjP < 0.05$) and number of differentially accessible regions i.e., nDARs (**k**) ($|logFC| > 0.25$ and $adjP < 0.05$) within indicated BM myeloid clusters of *Nfe2l2^{ΔMs4a3}* mice. **l**, Differentially expressed genes in BM Ly6C^{hi} monocytes of tumor-bearing *Nfe2l2^{ΔMs4a3}* mice compared to *Nfe2l2^{fl/fl}* littermates. **m**, Transcription factor (TF) motifs differentially enriched in BM Ly6C^{hi} monocytes of tumor-bearing *Nfe2l2^{ΔMs4a3}* compared to *Nfe2l2^{fl/fl}* littermates; ranked by FDR. **n**, scRNA-seq UMAP and heatmap of per-cell UMI counts (left) alongside relative abundance (right) of indicated myeloid sub-clusters in lung tissue of tumor-bearing *Nfe2l2^{ΔMs4a3}* and *Nfe2l2^{fl/fl}* mice. $n=3$ mice pooled per group. **o**, Number of DEGs ($|logFC| > 1$, $adjP < 0.05$) within indicated lung tumoral myeloid clusters of *Nfe2l2^{ΔMs4a3}* mice. **p**, Normalized UCell-computed scores for NRF2 activation and Type I/III Interferon (IFN)-stimulation in lung-infiltrating Ly6C^{hi} monocytes from scRNA-seq of tumor-bearing *Nfe2l2^{ΔMs4a3}* and *Nfe2l2^{fl/fl}* mice. $n=3$ per group. Data are per-cell distribution plot. **q**, Differentially expressed genes in tumor-infiltrating mo-macs ($Arg1^{hi}, Trem2^{hi}$) of tumor-bearing *Nfe2l2^{ΔMs4a3}* mice compared to *Nfe2l2^{fl/fl}* littermates. Individual data points with bar denoting mean, representative of two independent experiments (**a,b,c,d,e**). Scale bar, 2 mm (**c**). Statistics computed by Log-rank (Mantel-Cox) test (**a**), unpaired two-tailed Student's t-test (**b-e**), paired two-tailed t-test (**f-h**), hypergeometric test with multiple test correction (**l,p,q**).



Extended Data Fig. 9 | Tumor-induced NRF2 signaling in BM limits T and NK cell activity in TME. **a–b**, Number of blood Ly6G^{hi} neutrophils in blood (**a**) and lung (**b**) of tumor-bearing *Nfe2l2*^{ΔMS4A3CreERT2} mice with early (n = 5) vs late deletion (n = 6) of NRF2. **c**, Representative gating strategy for major mouse lung lymphoid (T, B, NK cell) populations, with exemplar phenotypic markers depicted for CD8⁺ T cells and NK cells. **d–e**, Number of lung-infiltrating NK cells (**d**) and frequency of NK cells expressing CD69, NKG2D, and producing IFN γ (**e**) in KP tumor-bearing *Nfe2l2*^{ΔMS4A3} mice (n = 8) or negative littermates (n = 7) at day 21. **f–g**, Number of lung-infiltrating CD8⁺ T cells expressing PD-1, LAG3, CD69, or producing IFN γ , TNF α (**g**)

in KP tumor-bearing *Nfe2l2*^{ΔMS4A3} mice (n = 8) or negative littermates (n = 7) at day 21. **h**, Representative histology and tumor burden for KP tumor-bearing *Nfe2l2*^{ΔMS4A3} mice and *Nfe2l2*^{ΔMS4A3CreERT2} control that received anti-CSF1R depletion antibodies or isotype. n = 5 mice per group. **i**, Representative histology and tumor burden for KP tumor-bearing *Nfe2l2*^{ΔMS4A3} mice that received anti-NK1.1 antibodies or isotype. n = 7 mice per group. Unless noted, data shown as individual data points with bar denoting mean, representative of two independent experiments (**a,b,d–g**). Scale bar, 2 mm (**h,i**). Statistics computed by unpaired two-tailed Student's t-test (**a,b**), one-way ANOVA with Sidak's multiple comparison (**h**).



Extended Data Fig. 10 | NRF2 pathway activation in TME myeloid cells is associated with immunotherapy resistance. a

ChIP-X Enrichment Analysis (ChEA) calculated TF regulators for differentially expressed genes in tumoral mo-macs enriched in non-responders (NR cohort) to neoadjuvant immunotherapy (NAIT) for lung cancer (NSCLC, Hu et al., n = 12 patients), compared to responders (R cohort), arranged by adjusted p-value (log q-value). **b**, ChEA calculated TF regulators for differentially expressed genes in tumoral mo-macs from patients with no clonal T cell expansion (NE cohort) after immune checkpoint blockade (ICB) in breast cancer (BC, Bassez et al., n = 29 patients) compared to macs from patients with clonal expansion (E cohort). **c–d**, ChEA calculated TF regulators for differentially expressed genes in tumoral mo-macs (**c**) and peripheral blood CD14⁺ monocytes (**d**) enriched in non-responders exhibiting stable disease (SD) to immune checkpoint blockade (ICB) for colorectal cancer (CRC, Chen et al., n = 22 patients) compared to complete response (CR). **e**, Kaplan-Meier plot depicting overall survival of KP tumor-bearing mice treated with Brusatol in conjunction with anti-PD-1.

immunotherapy (n = 8), Brusatol alone (n = 6), anti-PD-1 alone (n = 7), or vehicle (n = 6). **f**, Kaplan-Meier plot depicting overall survival of KP tumor-bearing mice treated with ML385 in conjunction with anti-PD-1 immunotherapy (n = 6), ML385 alone (n = 5), or vehicle (n = 5). **g**, Representative histology and tumor burden for KP tumor-bearing *Nfe2l2^{ΔMs4a3Cre}* and *Nfe2l2^{+/+}* mice that received Brusatol in conjunction with anti-PD1 (left to right, n = 6, 4, 5, 4, 5, 5). **h**, Frequency of NK cells within CD45⁺ cells (left), and percentage of NK cells expressing CD69 and producing IFNγ (right) in tumor-bearing WT mice treated as indicated. n = 5 mice per group. **i**, Frequency of CD8⁺ T cells within CD45⁺ cells (left), and percentage of CD8⁺ T cells expressing PD1⁺, LAG3⁺ or producing IFNγ, TNFα (right) in tumor-bearing WT mice treated as indicated. n = 5 per group. Individual data points with bar denoting mean (**g,h,i**), representative of two independent experiments (**e,f,g,h,i**). Scale bar, 2 mm (**g**). Statistics computed by hypergeometric test with multiple test correction (**a–d**), Log-rank (Mantel-Cox) test (**e,f**), and one-way ANOVA with Sidak's multiple comparison (**g**) or Dunnett's multiple comparison (**h,i**).

Reporting Summary

Nature Portfolio wishes to improve the reproducibility of the work that we publish. This form provides structure for consistency and transparency in reporting. For further information on Nature Portfolio policies, see our [Editorial Policies](#) and the [Editorial Policy Checklist](#).

Statistics

For all statistical analyses, confirm that the following items are present in the figure legend, table legend, main text, or Methods section.

n/a Confirmed

- The exact sample size (n) for each experimental group/condition, given as a discrete number and unit of measurement
- A statement on whether measurements were taken from distinct samples or whether the same sample was measured repeatedly
- The statistical test(s) used AND whether they are one- or two-sided
Only common tests should be described solely by name; describe more complex techniques in the Methods section.
- A description of all covariates tested
- A description of any assumptions or corrections, such as tests of normality and adjustment for multiple comparisons
- A full description of the statistical parameters including central tendency (e.g. means) or other basic estimates (e.g. regression coefficient) AND variation (e.g. standard deviation) or associated estimates of uncertainty (e.g. confidence intervals)
- For null hypothesis testing, the test statistic (e.g. F , t , r) with confidence intervals, effect sizes, degrees of freedom and P value noted
Give P values as exact values whenever suitable.
- For Bayesian analysis, information on the choice of priors and Markov chain Monte Carlo settings
- For hierarchical and complex designs, identification of the appropriate level for tests and full reporting of outcomes
- Estimates of effect sizes (e.g. Cohen's d , Pearson's r), indicating how they were calculated

Our web collection on [statistics for biologists](#) contains articles on many of the points above.

Software and code

Policy information about [availability of computer code](#)

Data collection

Data from flow cytometry were collected on a BD LSRLFortessa Analyzer, BD FACSAria-II using BD FACSDiva v8.0.2 or on a Beckman CytoFlex SRT using Beckman CytoExpert software. Gene expression reads were aligned to the mm10 reference transcriptome and count matrices were generated using the default CellRanger 2.1 workflow, using 'raw' matrix output. Fastq files from murine scATAC-seq samples were aligned to mouse genome reference mm10 using cellranger-atac v2.0.0. Fastq files from scATAC-seq and multiome samples were aligned to human genome reference hg38 using cellranger-atac v2.0.0 or cellranger-arc v2.0.0 respectively.

Data analysis

Flow cytometry data were analyzed using Flow Jo v10.9. Statistics were performed on Graphpad Prism v10. Histology scanned H&E slides were quantified using QuPath v0.4. For sequencing experiments, gene set enrichment analysis was performed using the EnrichR database and GREAT database. Other R packages used for single-cell analysis of newly generated and published datasets include: BiocManager v1.30.22; biomaRt v2.56.1; BSgenome v1.68.0; BSgenome.Mmusculus.UCSC.mm10 sequences; BSgenome.Hsapieins.UCSC.hg38 sequences; Seurat v4.4.0 and v4.9.9; harmony v0.1.1; scDissector v1.0.0; parallel v4.3.1; ShinyTree v0.2.7; data.table v1.14.8; reshape2 v1.4.4; reticulate v1.32.0; heatmaply v1.1.0; pheatmap v1.0.12; plotly v4.10.0; ggvis v0.4.7; ggplot2 v3.3.5; cowplot v1.1.1; patchwork v1.1.3; dplyr v1.3.1; tidyr v1.3.0; tidyverse v2.0.0; plyranges v.1.20.0; Matrix v0.9.8; seriation v.1.3.5; ArchR v1.0.2; chromVAR v1.22.1; Signac v.1.11.9; complexHeatmap v2.16.0; motifmatchr v1.20.0; deepTools v3.5.5; hdWGCNA v0.2.18; edgeR v3.42.4; limma v3.56.2; presto v1.0.0; EnhancedVolcano v1.18.0; GenomeInfoDb v1.36.1; GenomicRanges v1.52.0; MAST v1.6; Nebulosa v1.10.0; RColorBrewer v1.1; scCustomize v1.1.3; seasy v.0.0.7; scTools v1.0; SeuratDisk v.0.0.0.9; SeuratWrappers v0.3.19; SignaturR v.0.1.1; SingleCellExperiment v1.22.0; TFBSTools v1.38.0; UCell v2.4.0. Olink data was analyzed using package OlinkAnalyze v4.1.2. Exemplar code for notable analyses in this study are provided at github.com/Merad-Lab/Hegde_Myelopoiesis_Epigenetics.

For manuscripts utilizing custom algorithms or software that are central to the research but not yet described in published literature, software must be made available to editors and reviewers. We strongly encourage code deposition in a community repository (e.g. GitHub). See the Nature Portfolio [guidelines for submitting code & software](#) for further information.

Data

Policy information about [availability of data](#)

All manuscripts must include a [data availability statement](#). This statement should provide the following information, where applicable:

- Accession codes, unique identifiers, or web links for publicly available datasets
- A description of any restrictions on data availability
- For clinical datasets or third party data, please ensure that the statement adheres to our [policy](#)

No new software pipelines were used in the study beyond those described in relevant Methods sections. Exemplar data objects in this study are provided at github.com/Merad-Lab/Hegde_Myelopoiesis_Epigenetics. Accession numbers for re-analyzed published datasets are listed in Supplementary Table 7. Processed matrix files and metadata for the mouse tissue scRNA-seq and scATAC-seq generated in this study are made publicly available (GSE270148). Processed matrix files and metadata for the human tissue scATAC-seq and 10x multiome data generated in this study are also made publicly available (GSE270148).

Research involving human participants, their data, or biological material

Policy information about studies with [human participants or human data](#). See also policy information about [sex, gender \(identity/presentation\), and sexual orientation](#) and [race, ethnicity and racism](#).

Reporting on sex and gender

Biological sex was reported for all patients and healthy donors involved in the study, and reported in Supplementary Table 3. Disaggregated gender data is not collected separately.

Reporting on race, ethnicity, or other socially relevant groupings

Socially constructed or relevant groupings were not considered in this study.

Population characteristics

Relevant characteristics from all patients and healthy donors involved in the study can be found in Supplementary Table 3.

Recruitment

Patients were recruited by clinical research coordinators from the population treated for NSCLC by physicians from the Mount Sinai Center for Thoracic Oncology. Healthy donors were recruited by clinical research coordinators in accordance with IRB regulations and age range-matched where possible. There were no potential self-selection biases.

Ethics oversight

All human studies were performed with the oversight and approval of the Institutional Review Board (IRB) of the Icahn School of Medicine at Mount Sinai (ISMMS). The studies were under IRB Human Subjects Electronic Research Applications 10-00472A, in accordance with the protocol reviewed and approved by the IRB at ISMMS.

Note that full information on the approval of the study protocol must also be provided in the manuscript.

Field-specific reporting

Please select the one below that is the best fit for your research. If you are not sure, read the appropriate sections before making your selection.

Life sciences

Behavioural & social sciences

Ecological, evolutionary & environmental sciences

For a reference copy of the document with all sections, see nature.com/documents/nr-reporting-summary-flat.pdf

Life sciences study design

All studies must disclose on these points even when the disclosure is negative.

Sample size

No statistical methods were used a priori to determine sample size. Sample size was based on power analyses from prior studies in the lab and upon establishing reproducibility between experiments.

Data exclusions

In scRNA-seq and scATAC-seq data, cells were excluded based on commonly-used, pre-established criteria (low number of detectable transcripts, erythrocyte transcriptional content, high mitochondrial transcriptional content, low TSS enrichment score). Cells were further filtered based on myeloid cell markers for focused analysis. No data was excluded in flow cytometry or tumor burden experiments.

Replication

Experiments were replicable, and performed at least twice unless otherwise indicated in text. scRNA and ATA sequencing experiments were pooled analyses of multiple samples.

Randomization

Mice were randomly assigned to treatment or control groups post tumor implantation and prior to treatment start. Human studies profiled patients screened with lung cancer versus healthy donor controls, therefore, no randomization was required.

Blinding

Due to the objective manner of analysis, researchers were not blinded in treatment studies. For analyses of scanned H&E images, investigators were blinded to labels for treatment and/or genotype.

Reporting for specific materials, systems and methods

We require information from authors about some types of materials, experimental systems and methods used in many studies. Here, indicate whether each material, system or method listed is relevant to your study. If you are not sure if a list item applies to your research, read the appropriate section before selecting a response.

Materials & experimental systems

- | | |
|-------------------------------------|---|
| n/a | Involved in the study |
| <input type="checkbox"/> | <input checked="" type="checkbox"/> Antibodies |
| <input type="checkbox"/> | <input checked="" type="checkbox"/> Eukaryotic cell lines |
| <input checked="" type="checkbox"/> | <input type="checkbox"/> Palaeontology and archaeology |
| <input type="checkbox"/> | <input checked="" type="checkbox"/> Animals and other organisms |
| <input checked="" type="checkbox"/> | <input type="checkbox"/> Clinical data |
| <input checked="" type="checkbox"/> | <input type="checkbox"/> Dual use research of concern |
| <input checked="" type="checkbox"/> | <input type="checkbox"/> Plants |

Methods

- | | |
|-------------------------------------|--|
| n/a | Involved in the study |
| <input checked="" type="checkbox"/> | <input type="checkbox"/> ChIP-seq |
| <input type="checkbox"/> | <input checked="" type="checkbox"/> Flow cytometry |
| <input checked="" type="checkbox"/> | <input type="checkbox"/> MRI-based neuroimaging |

Antibodies

Antibodies used

antibody (clone)	Source/Manufacturer	Catalog#	RRID	Dilution(1/X) or Dosage
anti-mouse CD45 (30-F11) Biolegend	103138 RRID:AB_2563061	400		
anti-mouse CD62L (MEL-14) Biolegend	104406 RRID:AB_313093	200		
anti-mouse CXCR4 (2B11) Thermo Fisher Scientific	12-9991-82 RRID:AB_891391	200		
anti-mouse CD88 (20/70) Biolegend	135813 RRID:AB_2750209	100		
anti-mouse CD117 (2B8) Thermo Fisher Scientific	25-1171-82 RRID:AB_469644	200		
anti-mouse Ly6A/E (D7) Thermo Fisher Scientific	56-5981-82 RRID:AB_657836	200		
anti-mouse CD11b (M1/70) Thermo Fisher Scientific	48-0112-82 RRID:AB_1582236	400		
anti-mouse MHCII I-A/I-E (M5/114.15.2) Biolegend	107636 RRID:AB_2561397	400		
anti-mouse Ly6C (HK1.4) Biolegend	128035 RRID:AB_2562353	400		
anti-mouse CD115 (AFS98) Thermo Fisher Scientific	13-1152-85 RRID:AB_466565	200		
anti-mouse Siglec-F (1RN44N) Thermo Fisher Scientific	78-1702-80 RRID:AB_2744907	400		
anti-mouse CD34 (RAM34) Thermo Fisher Scientific	11-0341-82 RRID:AB_465022	25		
anti-mouse CD48 (HM48-1) Thermo Fisher Scientific	46-0481-80 RRID:AB_10870793	100		
anti-mouse CD135 (A2F10) Biolegend	135306 RRID:AB_1877217	100		
anti-mouse CD150 (TC15-12F12.2) Biolegend	115924 RRID:AB_2270307	100		
anti-mouse CD16/32 (93) Biolegend	553143 RRID:AB_394658	200		
anti-mouse CD16/32 (2.4G2) Thermo Fisher Scientific	56-0161-82 RRID:AB_394656	200		
anti-mouse CD11c (N418) Thermo Fisher Scientific	47-0114-82 RRID:AB_1548652	300		
anti-mouse CD11b (M1/70) Thermo Fisher Scientific	47-0112-82 RRID:AB_1603193	400		
anti-mouse CD44 (IM7) Biolegend	103041 RRID:AB_2571953	200		
anti-mouse Ly6G (1A8) Biolegend	127624 RRID:AB_10645331	400		
anti-mouse TER119 (TER-119) Thermo Fisher Scientific	47-5921-82 RRID:AB_1548786	200		
anti-mouse NK1.1 (PK136) Biolegend	108724 RRID:AB_830870	200		
anti-mouse CD3e (17A2) Thermo Fisher Scientific	47-0032-82 RRID:AB_1272181	200		
anti-mouse B220 (RA3-6B2) Thermo Fisher Scientific	47-0452-82 RRID:AB_1518810	200		
anti-mouse CD25 (PC61) Biolegend	102028 RRID:AB_2295974	200		
anti-mouse CD335/NKp46 (29A1.4) Thermo Fisher Scientific	12-3351-82 RRID:AB_1210743	200		
anti-mouse PD-1 (J43) Thermo Fisher Scientific	25-9985-82 RRID:AB_10853805	200		
anti-mouse LAG-3 (C9B7W) Biolegend	125209 RRID:AB_1063972	200		
anti-mouse TIM-3 (BB.2C12) Thermo Fisher Scientific	17-5871-82 RRID:AB_2573234	200		
anti-mouse CD4 (GK1.5) Biolegend	100430 RRID:AB_493699	200		
anti-mouse CD8a (53-6.7) Biolegend	100750 RRID:AB_2562610	200		
anti-mouse CD3e (eBio500A2) Thermo Fisher Scientific	48-0033-82 RRID:AB_2016704	200		
anti-mouse KLRG1 (2F1/KLRG1) Biolegend	138405 RRID:AB_10578565	200		
anti-mouse PD-L1 (MIH5) Thermo Fisher Scientific	12-5982-82 RRID:AB_466089	200		
anti-mouse PD-L2 (TY25) Thermo Fisher Scientific	12-5986-82 RRID:AB_466097	200		
anti-mouse CD40 (1C10) Thermo Fisher Scientific	17-0401-82 RRID:AB_469386	100		
anti-mouse CD86 (GL-1) Biolegend	105022 RRID:AB_493466	100		
anti-mouse CD80 (16-10A1) Biolegend	104725 RRID:AB_10900989	100		
anti-mouse MERTK (2B10C42) Biolegend	151503 RRID:AB_2617035	200		
anti-mouse F4/80 (BM8) Biolegend	123106 RRID:AB_893501	200		
anti-mouse CD64 (X54-5/7.1) Biolegend	139318 RRID:AB_2566557	300		
anti-mouse CD206 (C068C2) Biolegend	141720 RRID:AB_2562248	200		
anti-mouse CD11c (N418) Biolegend	117336 RRID:AB_2565268	300		
anti-mouse CD2 (RM2-5) Biolegend	100114 RRID:AB_2563092	200		
anti-mouse CD19 (eBio1D3) Thermo Fisher Scientific	48-0193-82 RRID:AB_2734905	200		
anti-mouse CD45.2 (104) Thermo Fisher Scientific	45-0454-82 RRID:AB_953590	100		
anti-mouse CD45.1 (A20) Biolegend	110741 RRID:AB_2563378	100		
anti-mouse NKG2D (CX5) Thermo Fisher Scientific	13-5882-85 RRID:AB_466746	200		
anti-mouse XCR1 (ZET) Biolegend	148220 RRID:AB_2566410	200		
anti-mouse IFNg (XMG1.2) Biolegend	505850 RRID:AB_2616698	100		
anti-mouse TNFa (MP6-XT22) Biolegend	506307 RRID:AB_315429	100		
anti-mouse FOXP3 (FJK-16s) Thermo Fisher Scientific	17-5773-82 RRID:AB_469457	100		
anti-mouse CD157 (BP-3) Biolegend	140207 RRID:AB_10901172	200		

anti-mouse CD319 (4G2) Biolegend 152005 RRID:AB_2632677 200
 anti-mouse Ly6G (1A8) Biolegend 127645 RRID:AB_2566317 400
 anti-mouse CD177 R&D Systems FAB8186P025 N/A 200
 anti-mouse Arg1 (A1exF5) Thermo Fisher Scientific 48-3697-82 RRID:AB_2734837 50
 anti-mouse CD163 (S150491) Biolegend 155309 RRID:AB_2814063 100
 anti-mouse GPNMB (CTSREVL) Thermo Fisher Scientific 50-5708-82 RRID:AB_2574239 100
 anti-mouse CD9 (MZ3) Biolegend 124817 RRID:AB_2783077 100
 anti-mouse ki67 (SolA15) Thermo Fisher Scientific 11-5698-82 RRID:AB_11151330 100
 anti-mouse/human HO-1 (HO-1-2) Enzo ADI-OSA-111-F RRID:AB_10618556 100
 Streptavidin BV650 Biolegend 405232 N/A 400
 Streptavidin BV510 Biolegend 405233 N/A 400
 Streptavidin APC-e780 Thermo Fisher Scientific 47-4317-82 RRID:AB_10366688 400
 anti-mouse/human p38 MAPK (pT180/pY182) (4NIT4KK) Thermo Fisher Scientific 12-9078-41 RRID:AB_2572691 100
 anti-mouse NK1.1 (PK136) BioXCell #BE0036 RRID:AB_1107737 200 ug/dose
 anti-mouse IgG2a (C1.18.4) BioXCell #BE0085 RRID: AB_1107771 200 ug/dose
 anti-mouse PD-1 (RMP1-14) BioXCell #BE0146 RRID:AB_10949053 100 ug/dose
 anti-mouse CSF1R (AFS98) BioXCell #BE0213 RRID:AB_2687699 400 ug/dose
 anti-mouse IgG2a (2A3) BioXCell #BE0089 RRID: AB_1107769 400 ug/dose
 Human TruStain FcX Biolegend 422302 RRID:AB_2818986 100
 anti-human CD34 (AC136) Miltenyi Biotec 130-113-178 RRID:AB_2726005 50
 anti-human HLA-DR BD Biosciences 552764 RRID:AB_394453 100
 anti-human CD14 (M5E2) Biolegend 301839 RRID:AB_2563425 100
 anti-human CD38 (HIT2) Biolegend 303515 RRID:AB_2072782 100
 anti-human CD90 (5E10) Biolegend 328119 RRID:AB_2203302 100
 anti-human CD45RA (HI100) Biolegend 304127 RRID:AB_10708880 100
 anti-human CD49f (GoH3) Biolegend 313619 RRID:AB_2128022 100
 anti-human CD16 (3G8) Biolegend 302017 RRID:AB_314218 200
 anti-human CD66b (G10F5) Biolegend 305114 RRID:AB_2566038 200
 anti-human CD11c (3.9) Biolegend 301612 RRID:AB_493021 100
 anti-human CD20 (2H7) Biolegend 302349 RRID:AB_2565524 100
 anti-human CD3 (5K7) Biolegend 344820 RRID:AB_10662538 100
 anti-human CD56 (5.1H11) Biolegend 362535 RRID:AB_2565652 100
 Streptavidin BV605 Biolegend 405229 N/A 400
 anti-human CD11c (3.9) Biolegend 301612 RRID:AB_493021
 anti-human CD20 (2H7) Biolegend 302349 RRID:AB_2565524
 anti-human CD3 (5K7) Biolegend 344820 RRID:AB_10662538
 anti-human CD56 (5.1H11) Biolegend 362535 RRID:AB_2565652

Validation

antibody (clone) | validation comments

anti-mouse CD45 (30-F11) Flow cytometry of ms splenocytes (manufacturer's website)
 anti-mouse CD62L (MEL-14) Flow cytometry of ms splenocytes (manufacturer's website)
 anti-mouse CXCR4 (2B11) Flow cytometry of ms splenocytes (manufacturer's website)
 anti-mouse CD88 (20/70) Flow cytometry of ms splenocytes (manufacturer's website)
 anti-mouse CD117 (2B8) Flow cytometry of ms splenocytes (manufacturer's website)
 anti-mouse Ly6A/E (D7) Flow cytometry of ms splenocytes (manufacturer's website)
 anti-mouse CD11b (M1/70) Flow cytometry of ms splenocytes (manufacturer's website)
 anti-mouse MHCII I-A/I-E (M5/114.15.2) Flow cytometry of ms splenocytes (manufacturer's website)
 anti-mouse Ly6C (HK1.4) Flow cytometry of ms splenocytes (manufacturer's website)
 anti-mouse CD115 (AFS98) Flow cytometry of ms splenocytes (manufacturer's website)
 anti-mouse Siglec-F (1RNMA4N) Flow cytometry of ms splenocytes (manufacturer's website)
 anti-mouse CD34 (RAM34) Flow cytometry of ms splenocytes (manufacturer's website)
 anti-mouse CD48 (HM48-1) Flow cytometry of ms splenocytes (manufacturer's website)
 anti-mouse CD135 (A2F10) Flow cytometry of ms splenocytes (manufacturer's website)
 anti-mouse CD150 (TC15-12F12.2) Flow cytometry of ms splenocytes (manufacturer's website)
 anti-mouse CD16/32 (93) Flow cytometry of ms splenocytes (manufacturer's website)
 anti-mouse CD16/32 (2.4G2) Flow cytometry of ms splenocytes (manufacturer's website)
 anti-mouse CD11c (N418) Flow cytometry of ms splenocytes (manufacturer's website)
 anti-mouse CD11b (M1/70) Flow cytometry of ms splenocytes (manufacturer's website)
 anti-mouse CD44 (IM7) Flow cytometry of ms splenocytes (manufacturer's website)
 anti-mouse Ly6G (1A8) Flow cytometry of ms splenocytes (manufacturer's website)
 anti-mouse TER119 (TER-119) Flow cytometry of ms splenocytes (manufacturer's website)
 anti-mouse NK1.1 (PK136) Flow cytometry of ms splenocytes (manufacturer's website)
 anti-mouse CD3e (17A2) Flow cytometry of ms splenocytes (manufacturer's website)
 anti-mouse B220 (RA3-6B2) Flow cytometry of ms splenocytes (manufacturer's website)
 anti-mouse CD25 (PC61) Flow cytometry of ms splenocytes (manufacturer's website)
 anti-mouse CD335/NKp46 (29A1.4) Flow cytometry of ms splenocytes (manufacturer's website)
 anti-mouse PD-1 (J43) Flow cytometry of ms splenocytes (manufacturer's website)
 anti-mouse LAG-3 (C9B7W) Flow cytometry of ms splenocytes (manufacturer's website)
 anti-mouse TIM-3 (8B.2C12) Flow cytometry of ms splenocytes (manufacturer's website)
 anti-mouse CD4 (GK1.5) Flow cytometry of ms splenocytes (manufacturer's website)
 anti-mouse CD8a (53-6.7) Flow cytometry of ms splenocytes (manufacturer's website)
 anti-mouse CD3e (eBio500A2) Flow cytometry of ms splenocytes (manufacturer's website)
 anti-mouse KLRG1 (2F1/KLRG1) Flow cytometry of ms splenocytes (manufacturer's website)
 anti-mouse PD-L1 (MIH5) Flow cytometry of ms splenocytes (manufacturer's website)
 anti-mouse PD-L2 (TY25) Flow cytometry of ms splenocytes (manufacturer's website)
 anti-mouse CD40 (1C10) Flow cytometry of ms splenocytes (manufacturer's website)

anti-mouse CD86 (GL-1) Flow cytometry of ms splenocytes (manufacturer's website)
 anti-mouse CD80 (16-10A1) Flow cytometry of ms splenocytes (manufacturer's website)
 anti-mouse MERTK (2B10C42) Flow cytometry of ms splenocytes (manufacturer's website)
 anti-mouse F4/80 (BM8) Flow cytometry of ms splenocytes (manufacturer's website)
 anti-mouse CD64 (X54-5/7.1) Flow cytometry of ms splenocytes (manufacturer's website)
 anti-mouse CD206 (C068C2) Flow cytometry of ms splenocytes (manufacturer's website)
 anti-mouse CD11c (N418) Flow cytometry of ms splenocytes (manufacturer's website)
 anti-mouse CD2 (RM2-5) Flow cytometry of ms splenocytes (manufacturer's website)
 anti-mouse CD19 (eBio1D3) Flow cytometry of ms splenocytes (manufacturer's website)
 anti-mouse CD45.2 (104) Flow cytometry of ms splenocytes (manufacturer's website)
 anti-mouse CD45.1 (A20) Flow cytometry of ms splenocytes (manufacturer's website)
 anti-mouse NKG2D (CX5) Flow cytometry of ms splenocytes (manufacturer's website)
 anti-mouse XCR1 (ZET) Flow cytometry of ms splenocytes (manufacturer's website)
 anti-mouse IFNg (XMG1.2) Flow cytometry of ms splenocytes (manufacturer's website)
 anti-mouse TNFa (MP6-XT22) Flow cytometry of ms splenocytes (manufacturer's website)
 anti-mouse FOXP3 (FJK-16s) Flow cytometry of ms splenocytes (manufacturer's website)
 anti-mouse CD157 (BP-3) Flow cytometry of ms splenocytes (manufacturer's website)
 anti-mouse CD319 (4G2) Flow cytometry of ms splenocytes (manufacturer's website)
 anti-mouse Ly6G (1A8) Flow cytometry of ms splenocytes (manufacturer's website)
 anti-mouse CD177 Flow cytometry of ms splenocytes (manufacturer's website)
 anti-mouse Arg1 (A1exF5) Flow cytometry of ms splenocytes (manufacturer's website)
 anti-mouse CD163 (S150491) Flow cytometry of ms splenocytes (manufacturer's website)
 anti-mouse GPNMB (CTSREVL) Flow cytometry of ms splenocytes (manufacturer's website)
 anti-mouse CD9 (MZ3) Flow cytometry of ms splenocytes (manufacturer's website)
 anti-mouse ki67 (SolA15) Flow cytometry of ms splenocytes (manufacturer's website)
 anti-mouse/human HO-1 (HO-1-2) Flow cytometry of ms splenocytes (manufacturer's website)
 Streptavidin BV650 Flow cytometry of ms splenocytes (manufacturer's website)
 Streptavidin BV510 Flow cytometry of ms splenocytes (manufacturer's website)
 Streptavidin APC-e780 Flow cytometry of ms splenocytes (manufacturer's website)
 anti-mouse/human p38 MAPK (pT180/pY182) (4NIT4KK) Flow cytometry of ms splenocytes (manufacturer's website)
 anti-mouse NK1.1 (PK136) Depletion of ms NK population of interest (manufacturer's website and in-house)
 anti-mouse IgG2a (C1.18.4) Depletion of ms population of interest (manufacturer's website and in-house)
 anti-mouse PD-1 (RMP1-14) Depletion of ms T cell population of interest (manufacturer's website and in-house)
 anti-mouse CSF1R (AFS98) Depletion of ms myeloid population of interest (manufacturer's website and in-house)
 anti-mouse IgG2a (2A3) Depletion of ms population of interest (manufacturer's website and in-house)
 Human TruStain FcX Flow cytometry of Hu splenocytes (manufacturer's website)
 anti-human CD34 (AC136) Flow cytometry of Hu splenocytes (manufacturer's website)
 anti-human HLA-DR Flow cytometry of Hu splenocytes (manufacturer's website)
 anti-human CD14 (M5E2) Flow cytometry of Hu splenocytes (manufacturer's website)
 anti-human CD38 (HIT2) Flow cytometry of Hu splenocytes (manufacturer's website)
 anti-human CD90 (SE10) Flow cytometry of Hu splenocytes (manufacturer's website)
 anti-human CD45RA (HI100) Flow cytometry of Hu splenocytes (manufacturer's website)
 anti-human CD49f (GoH3) Flow cytometry of Hu splenocytes (manufacturer's website)
 anti-human CD16 (3G8) Flow cytometry of Hu splenocytes (manufacturer's website)
 anti-human CD66b (G10F5) Flow cytometry of Hu splenocytes (manufacturer's website)
 anti-human CD11c (3.9) Flow cytometry of Hu splenocytes (manufacturer's website)
 anti-human CD20 (2H7) Flow cytometry of Hu splenocytes (manufacturer's website)
 anti-human CD3 (5K7) Flow cytometry of Hu splenocytes (manufacturer's website)
 anti-human CD56 (5.1H11) Flow cytometry of Hu splenocytes (manufacturer's website)
 Streptavidin BV605 Flow cytometry of Hu splenocytes (manufacturer's website)

All antibodies were validated by comparing to an FMO control for each marker in initial experiments.

Eukaryotic cell lines

Policy information about [cell lines and Sex and Gender in Research](#)

Cell line source(s)

GFP expressing KP cells were derived from cells received from Tyler Jacks, generated from previously reported and validated KP mouse model of NSCLC (Du Page et. al., 2009, *Nature Protocols*). KPAR cells were received from Julian Downward at Francis Crick Institute, and derived from previously reported and validated mouse models of NSCLC (Boumelha et al. 2022, *Cancer Research*). LLC1 carcinoma cells were received from Dr. Lucas Ferrari de Andrade at Mt Sinai originally purchased from ATCC (CRL-1642), and B16-F10 melanoma cells were purchased from ATCC (CRL-6475).

Authentication

Cells were functionally authenticated via intravenous tail vein injection into mice and monitoring of tumor growth in lungs. KP and KPAR cells were sequenced originally in laboratory to ascertain genetic mutation profile.

Mycoplasma contamination

All cell lines were routinely tested negative for mycoplasma contamination, and used within 3-5 passages.

Commonly misidentified lines (See [ICLAC register](#))

No commonly misidentified cell lines were used.

Animals and other research organisms

Policy information about [studies involving animals](#); [ARRIVE guidelines](#) recommended for reporting animal research, and [Sex and Gender in Research](#)

Laboratory animals

C57BL/6 mice were obtained from Charles River Laboratories (Wilmington, MA) or Jackson Laboratory (Bar Harbor, ME). CD45.1 congenic C57BL/6 mice were obtained from Jackson laboratory (C57BL/6J-Ptprc^{em6Lutzy}/J RRID:IMSR_JAX:033076). Ms4a3Cre mice were purchased from Jackson laboratory (C57BL/6J-Ms4a3em2(cre)Fgnx/J RRID:IMSR_JAX:036382), and Ms4a3CreERT2 mice were received from Florent Ginhoux. Nfe2l2fl/fl floxed mice were purchased from Jackson laboratory (C57BL/6-Nfe2l2tm1.1Sred/Sbis.J RRID:IMSR_JAX:025433). NRF2 constitutive knockout (Nfe2l2TKO) mice were purchased from Jackson laboratory (B6.129X1-Nfe2l2tm1Ywk/J RRID:IMSR_JAX:017009). Keap1fl/fl floxed mice were purchased from Jackson laboratory (B6(Cg)-Keap1tm1.1Sbis/J RRID:IMSR_JAX:037075). Mx1GFP mice were received from Adolfo Garcia-Sastre, and subsequently purchased from Jackson laboratory (B6.Cg-Mx1tm1.1Agsga/J RRID:IMSR_JAX:033219). KrasLSL-G12D/+;Trp53fl/fl mice used for autochthonous model of NSCLC (GEMM) were purchased from Jackson laboratory (B6.129-Krastm4Tyj Trp53tm1Brn/J RRID:IMSR_JAX:032435). Most experiments were conducted in mice between 10–14 weeks of age.

Wild animals

No wild animals were used.

Reporting on sex

Both male and female mice were used, and we observed no significant differences between sexes in experiments. Where applicable, littermate controls were used to minimize variation between mouse strains.

Field-collected samples

No field-collected samples were used in this study.

Ethics oversight

All experiments were approved by, and in compliance with the Institutional Animal Care and Use Committee of the Icahn School of Medicine at Mount Sinai.

Note that full information on the approval of the study protocol must also be provided in the manuscript.

Plants

Seed stocks

N/A

Novel plant genotypes

N/A

Authentication

N/A

Flow Cytometry

Plots

Confirm that:

- The axis labels state the marker and fluorochrome used (e.g. CD4-FITC).
- The axis scales are clearly visible. Include numbers along axes only for bottom left plot of group (a 'group' is an analysis of identical markers).
- All plots are contour plots with outliers or pseudocolor plots.
- A numerical value for number of cells or percentage (with statistics) is provided.

Methodology

Sample preparation

Mice were euthanized by CO₂ inhalation and death confirmed by cervical dislocation. Mice were subjected to transcardiac perfusion with cold PBS and relevant tissue extracted for downstream studies. Mouse lung lobes were digested on a shaker in RPMI media containing 10% FBS, Collagenase IV (Sigma) and DNase I (Sigma) for 30 minutes at 37°C before being triturated through an 18G needle and filtered through a 70 µm mesh. Samples were subjected to RBC Lysis Buffer (BioLegend) for 2 mins at RT and quenched with ice-cold FACS Buffer (phosphate-buffered saline supplemented with 1% bovine serum albumin and 2mM EDTA) prior to downstream processes. Bone marrow was flushed with cold FACS Buffer using a 27G needle from both long bones (femur and tibia) and filtered through a 70 µm mesh. Samples were subjected to RBC Lysis Buffer (BioLegend) for 2 mins at RT and quenched with ice-cold FACS Buffer prior to downstream processes. For assays such as low-input RNA and ATAC seq, marrow cells were enriched for Kit+ progenitors using the Mojosort Mouse Lin-neg enrichment kit (BioLegend #480004). Blood was collected by cardiac puncture in EDTA-coated tubes and RBCs were lysed in two successive cycles of 5 mins each, at RT in RBC Lysis Buffer (BioLegend). Samples were quenched with FACS Buffer and kept cold for downstream processes. Where relevant, serum was collected by coagulating blood in regular microcentrifuge tubes for 30 mins at RT prior to centrifugation at 5000g for 15 mins at RT. Serum aliquots were made and stored at -80°C until experiment.

Human NSCLC lung tissues were rinsed in cold PBS, minced, and incubated on a shaker for 35 minutes at 37°C in RPMI media containing Collagenase IV at 0.25 mg/ml, Collagenase D at 200 U/ml and DNase-I at 0.1 mg/ml (Sigma). Cell suspensions were then quenched in ice-cold FACS Buffer, triturated through a 18G needle, and filtered through a 70 µm mesh prior to RBC lysis for 2 mins at RT. Cell suspensions were enriched for CD45+ cells by either bead selection (bound fraction from Stem Cell EasySep Human CD45 Depletion Kit II) per kit instructions or FACS sorting on a BD FACSAria or Beckman CytoFlex SRT sorter prior to processing for scRNA-seq, scATAC-seq or Multiome.

Human NSCLC blood was processed as follows— PBMCs were isolated by Ficoll gradient and underwent RBC lysis for 5 mins at RT. Cell suspensions were enriched for all myeloid cells or CD34+ myeloid cells by either bead selection (bound fraction from StemCell Technologies Custom negative selection Kit or CD34 positive selection II Kit) or FACS sorting on a BD FACSAria or Beckman CytoFlex SRT sorter prior to processing for scRNA-seq, scATAC-seq or Multiome.

Instrument

BD LSRFortessa, BD FACSAria-II, Beckman CytoFlex SRT

Software

FACSDiva v8.0.2, Beckman CytoExpert

Cell population abundance

Purity and abundance were evaluated by second round of cytometry post-sort. Purity was above 90% for populations of interest.

Gating strategy

Example gating strategies described for all populations in brief written form (also see Extended Data Fig. 2, 3, and 9).

For all populations, cells were first gated on intact events based on FSC-A vs SSC-A, then gated on singlets based on FSC-A vs FSC-H as well as FSC-A vs FSC-W, then gated on live cells based on FSC-A vs Viability Dye/DAPI (analyzing viability Dye/DAPI-negative cells).

Note, Lineage = Ly6g, CD3e, B220, NK1.1, CD11b, Ter-119, unless noted.

BM Stem Cells : 1. Gate on FSC-A vs Lineage was set to exclude lineage+ cells. 2. Gate on Sca-1 vs c-KIT was set to enrich double-positive cells. 3. Gate on CD135 vs CD150 was set to exclude all CD135+ MPP4 cells. 3. Gate on CD48 vs CD150. HSC-LT are CD150+ and MPP3 are CD48hi.

BM CMP and MDP: 1. Gate on FSC-A vs Lineage was set to exclude lineage+ cells. Gate on Sca-1 vs c-KIT was set to enrich c-KIT+ Sca-1- cells. 3. Gate on CD16/32 vs CD34 was set to exclude CD16/32+ CD34+ cells. 4. Gate on CD135 vs CD115 was set. CMP are CD115- CD135hi. MDP are CD115+.

BM Bulk GMP; Ly6Cneg GMP, GP, cMoP: 1. Gate on FSC-A vs Lineage was set to exclude lineage+ cells. Gate on Sca-1 vs c-KIT was set to enrich c-KIT+ Sca-1- cells. 3. Gate on CD16/32 vs CD34 was set to enrich CD16/32+ CD34+ cells. 4. Gate on CD34 vs CD135 was set to exclude CD135+ cells. This population constituted bulk GMPs. 5. Gate on bulk GMPs Ly6c vs CD115. Ly6Cneg GMPs are double negative. GPs are Ly6c+CD115-. cMoPs are Ly6c+CD115+.

BM monocytes and neutrophils: 1. Gate on Sca-1 vs c-Kit to select c-Kitneg population. 2. Gate on CD11b+ for more mature myeloid cells. 3. Gate on Ly6G+ population and use CXCR2 vs CXCR4 to differentiate preNeus from mature Neus (CXCR2hi). 4. Gate on CD115+ Ly6Chi populations and use CXCR4 to differentiate preMono from mature monocytes (CXCR4low).

Lung myeloid cells: 1. Gate on SSC-A vs CD45 to enrich CD45+ cells. 2. Gate on SigF vs CD11c. Double-positive cells are alveolar macrophages (AM). Continue on non-AM. 3. Gate on CD11b+ and then exclude Ly6G+SigF+ Neutrophils and granulocytes. 4. Gate on CD64 vs MerTK. Double positive cells are macrophages. Continue gating on non-macrophages. 5. Gate on MHC-II vs CD11c. Double positive cells are DCs. Within DCs, CD103+ cells are DC1 and CD11b+Sirpa+ cells are DC2. Continue gating on non-DCs. 6. Gate on Ly6C vs CD11c. Use Ly6C expression to discriminate Ly6CHI inflammatory monocytes from Ly6CLOW patrolling monocytes.

Blood myeloid cells: 1. Gate on SSC-A vs CD45 to enrich CD45+ cells. 2. Gate on FSC-A vs CD3e, CD19, NK1.1 to exclude CD3, CD19, and NK1.1+ cells. 3. Gate on CD11b vs Ly6G. Double positive cells are neutrophils. Continue gating on non-neutrophils. 3. Gate on Ly6C vs CD115. Double positive cells are monocytes. Monocytes can be further separated by Ly6C staining and CD62L or CD43 into Ly6CHI inflammatory and Ly6CLOW patrolling monocytes.

Lung B cells, CD4 T cells, CD8 T cells: 1. Gate on SSCA-vs CD45 to enrich CD45-HI SSC-A-LO cells. 2. Gate on CD19 vs CD3e from CD11blow cells. CD19 single-positive cells are B cells. Continue gating on CD3e single positive. 3. Gate on CD4 vs CD8. CD8 single positive are CD8 T cells. CD4 single positive are CD4 T cells.

Lung NK cells: 1. Gate on SSCA-vs CD45 to enrich CD45-HI SSC-A-LO cells. 2. Gate on CD3e vs NK1.1 or NKp46 from CD11blow cells.

Human blood: 1. Gate on Lineage-neg cells. Lineage: CD20, CD3, CD56, CD11c. 2. Gate on CD66Bneg (non-granulocytes) and then on CD34 and CD38. CD34+ CD38+ population further split by CD49f and CD45RA. CD45RA+ CD49fneg population is GMP, CD45RAneg population is CMP. CD34+ CD38neg population (stem cells) further split by CD90 and CD45RA; CD90+ HSCs and CD45RA+ LMPPs.

Tick this box to confirm that a figure exemplifying the gating strategy is provided in the Supplementary Information.